

**PHOSPHATE ANION ADSORPTION PROPERTIES OF COPPER-  
EXCHANGED ZEOLITES AND THEIR UTILITY AS A PROBE  
FOR ACTIVE SITE STRUCTURE**

by  
Akshat Vij

A dissertation submitted to Johns Hopkins University in conformity with  
the requirements for the degree of Doctor of Philosophy

Baltimore, Maryland  
December 2020

© 2020 Akshat Vij  
All rights reserved

## Abstract

Phosphorus is an essential macronutrient for plant growth and a key element in all biological systems. Zeolites—microporous, crystalline aluminosilicates amenable to modification through green chemical techniques—are one proposed class of material for the recovery of phosphate through adsorption. In this work, copper ZSM-5 zeolites with varying Si/Al ratios were synthesized using an ion exchange method and systematically studied for their performance in adsorbing inorganic dissolved phosphate from synthetic solutions. Maximum orthophosphate uptake of greater than 70% was reported at process-relevant conditions. Copper ZSM-5 with lower Si/Al ratios exhibited the greatest adsorption capacity, with higher pH enhancing uptake. On balance metal-exchanged zeolites were found to present a promising direction in the development of highly tunable synthetic sorbents for inorganic dissolved phosphate.

Metal-exchanged zeolites have long been of interest due to their catalytic activity. In particular, copper ZSM-5 has been studied intensely because of its activity in treating automotive exhaust gases. However, the exact nature of the catalytic sites—generally considered to be Cu dimers of the form  $[\text{Cu-O-Cu}]^{2+}$ —has never been fully understood. Quantifying the active site structures in metal-exchanged zeolites has

## ABSTRACT

represented one particular challenge in overcoming the gaps in understanding between material properties and their fundamental structure. Traditional methods used to titrate these sites have relied on gaseous probes combined with complex spectroscopic analysis. In this work, liquid phase phosphate anion adsorption is proposed as a unique, simpler alternative to probe and quantify the Cu sites in copper ZSM-5. Equilibrium and kinetic data for phosphate adsorption was considered together with the copper loadings of Cu-ZSM-5 prepared at several Si/Al ratios to investigate the zeolite structure. Phosphate adsorption property parameters were found to show strong linear correlations with the Cu density, facilitating quantification of the copper dimer fraction through analysis of the adsorption site capacity at low concentrations. It was concluded that liquid phase phosphate anion adsorption could represent a simple tool for probing and quantifying the copper speciation in copper ZSM-5. This presents a new and unique direction for understanding the active site structures in metal-exchanged zeolites.

**Advisor**      Dr. Chao Wang  
**Reader 1**     Dr. Marc D. Donohue  
**Reader 2**     Dr. Anthony Shoji Hall

## **Acknowledgements**

I thank Dr. Chao Wang for his guidance and support over the course of my studies at Johns Hopkins University. He has provided me with an excellent foundation in the field of research that will serve me well in the future.

I acknowledge the support of the Department of Chemical and Biomolecular Engineering, the Whiting School of Engineering and all the faculty, staff and fellow students I have had the pleasure of meeting. In particular, I acknowledge the work, collaboration and help of Beth Rannie in helping our laboratory run smoothly and always being a valuable point of contact for student-related issues.

I thank Phillip Chapman from the Department of Materials Science and Engineering for his time and assistance in training and troubleshooting equipment and facilities used in this work. Similarly, I acknowledge the Johns Hopkins University Integrated Imaging Center, a partner with the Institute of NanoBio Technology.

I also acknowledge the support of my family and friends. In particular, I thank Dr. Muneeba Khalid, for making my time at Hopkins the best years of my life.

# Contents

<b>Abstract</b>	<b>ii</b>
<b>Acknowledgements</b>	<b>iv</b>
<b>List of Tables</b>	<b>x</b>
<b>List of Figures</b>	<b>xii</b>
<b>Chapter 1 Introduction</b>	<b>1</b>
1.1 The importance of phosphorus .....	1
1.2 Phosphorus in the environment: pollutant and resource .....	9
1.2.1 Flow of phosphorus in nature and the human impact .....	9
1.2.2 Eutrophication .....	13
1.3 Solutions to the phosphorus problem .....	16
1.3.1 The separation problem .....	17
1.4 Zeolites .....	18
1.4.1 Metal-exchanged zeolites .....	21
1.5 Research objectives and dissertation overview .....	25
<b>Chapter 2 Literature review</b>	<b>27</b>

2.1	State of the art in inorganic dissolved phosphate recovery .....	27
2.1.1	Traditional removal techniques .....	28
2.1.1.1	Metal salt dosing .....	28
2.1.1.2	Biological removal .....	30
2.1.1.3	Crystallization .....	33
2.1.1.4	Struvite precipitation .....	36
2.1.2	Sorption removal .....	39
2.1.2.1	Mechanisms of sorption .....	40
2.1.2.1.1	Outer-sphere adsorption .....	40
2.1.2.1.2	Inner-sphere adsorption .....	43
2.1.2.1.3	Hydrogen bonding .....	47
2.1.2.1.4	Surface precipitation .....	47
2.1.2.1.5	Intra-sorbent diffusion .....	48
2.1.2.2	Sorption materials .....	50
2.1.2.2.1	Inorganic materials .....	51
2.1.2.2.2	Other materials .....	61
2.2	Characterization of Cu in copper-exchanged ZSM-5 .....	61
2.2.1	Analytical techniques .....	64
2.2.1.1	Spectroscopy .....	64
2.2.1.2	Probe molecules and temperature programmed methods .....	66
2.2.1.3	Liquid phase probes .....	68
<b>Chapter 3</b>	<b>Methodology</b>	<b>70</b>

## CONTENTS

3.1	Introduction.....	70
3.2	Considerations in the determination of phosphate adsorption.....	70
3.2.1	Batch vs. continuous flow .....	70
3.2.2	Quantification of the adsorbate .....	71
3.2.2.1	Phosphate determination in aqueous systems .....	72
3.3	Materials and methods .....	76
3.3.1	Synthesis of copper-exchanged ZSM-5 .....	76
3.3.2	Batch tests for measuring phosphate adsorption .....	80
3.3.2.1	Kinetic data .....	82
3.3.3	pH measurement.....	82
3.3.4	Spectrophotometric determination of phosphate.....	82
3.3.5	Spectrophotometric determination of copper .....	87
3.3.6	Characterization of solid samples .....	89
3.3.6.1	Copper and aluminum content.....	89
3.3.6.2	X-ray powder diffraction (XRD) .....	89
3.3.6.3	Scanning electron microscopy (SEM) .....	90
3.3.6.4	Attenuated total reflectance Fourier-transform infrared spectroscopy (ATR-FT-IR).....	90
3.3.7	Non-linear regression and equation solving.....	91
3.3.8	Error analysis.....	93
<b>Chapter 4 Results</b>		<b>94</b>
4.1	Introduction.....	94

## CONTENTS

4.2	Molybdenum blue assay for inorganic dissolved phosphate .....	94
4.3	Characterization of Copper ZSM-5 .....	98
4.4	Copper ZSM-5 as a sorbent for phosphate .....	108
4.4.1	Adsorption uptake .....	108
4.4.2	Adsorption isotherms .....	110
4.4.3	Effect of pH.....	115
4.4.4	Copper leaching.....	123
4.5	Linking active sites and structure to phosphate adsorption .....	125
4.5.1	Adsorption isotherms .....	126
4.5.2	Effect of pH.....	132
4.5.3	Adsorption kinetics .....	134
4.5.4	Adsorption properties and active site structure .....	139
<b>Chapter 5 Discussion</b>		<b>150</b>
5.1	Introduction.....	150
5.2	Copper ZSM-5 as a sorbent for inorganic dissolved P.....	150
5.3	Adsorption isotherms and kinetic behavior .....	153
5.4	Dimers in copper ZSM-5 and the link to phosphate adsorption.....	156
<b>Chapter 6 Conclusions</b>		<b>164</b>
<b>Chapter 7 Supplementary</b>		<b>167</b>
7.1	Synthetic enzymes and the transition state in heterogeneous catalytic dephosphorylation.....	167



## CONTENTS

7.1.1	Methodology .....	171
7.1.2	Results, Discussion and Future Work .....	174
<b>Chapter 8</b>	<b>References</b>	<b>176</b>
	<b>Curriculum Vitae</b>	<b>188</b>

# List of Tables

<b>Chapter 1 Introduction</b>	<b>1</b>
<b>Table 1.1</b> Data on the sustainability of global phosphate rock production .....	8
<b>Table 1.2</b> Flows of P and the large anthropogenic impact on the phosphorus cycle (numerical values are all megatonnes P per annum) .....	12
<b>Chapter 2 Literature review</b>	<b>27</b>
<b>Table 2.1</b> Summary of the differences between outer- and inner-sphere adsorption mechanisms as applied to anionic species .....	46
<b>Chapter 3 Methodology</b>	<b>70</b>
<b>Table 3.1</b> Technical data for as-received ammonium ZSM-5 zeolite .....	77
<b>Chapter 4 Results</b>	<b>94</b>
<b>Table 4.1</b> Metals analysis for the Cu-ZSM-5 samples synthesized for this study .....	99
<b>Table 4.2</b> Langmuir and Freundlich isotherm parameters obtained by non-linear regression for adsorption of phosphate by Cu-ZSM-5. ....	113
<b>Table 4.3</b> Langmuir and Freundlich isotherm parameters obtained by non-linear regression for adsorption of phosphate by Cu-ZSM-5, normalized by copper content.....	130
<b>Table 4.4</b> Pseudo first order and pseudo second order kinetic model parameters obtained by non-linear regression for adsorption of phosphate by Cu- ZSM-5, normalized by copper content. ....	135

<b>Chapter 7 Supplementary</b>	<b>167</b>
--------------------------------	------------

<b>Table 7.1</b> LFER results for catalytic dephosphorylation.....	<b>175</b>
--	------------

# List of Figures

<b>Chapter 1 Introduction</b>	<b>1</b>
<b>Figure 1.1</b> Illustration of the phosphorus biogeochemical cycle .....	3
<b>Figure 1.2</b> Pareto chart showing the world’s current mine production of phosphate rock, based on estimated 2019 annual mine production.....	5
<b>Figure 1.3</b> Pareto chart showing the world’s current reserves of phosphate rock .....	6
<b>Figure 1.4</b> Phosphorous equilibrium and cycles in soil. ....	15
<b>Figure 1.5</b> Pore openings of selected zeolites. ....	20
<b>Figure 1.6</b> Schematic of the NH <sub>3</sub> -SCR based emissions control system on a 2011 Ford Super Duty diesel pickup truck .....	24
<b>Chapter 2 Literature review</b>	<b>27</b>
<b>Figure 2.1</b> Chemical dosing for P removal in waste-water treatment.....	29
<b>Figure 2.2</b> Simplified process illustration of biological P removal .....	32
<b>Figure 2.3</b> Solubility of phosphate species important to water treatment and soil systems.....	34
<b>Figure 2.4</b> Simplified schematic of the fluidized bed reactor (DHV Crystalactor) used in a commercialized crystallization removal process .....	35
<b>Figure 2.5</b> Example illustration of outer-sphere and inner-sphere adsorption mechanisms, along with the formation of the diffuse layer that balances the surface charge of the negatively charged sorbent. ....	42
<b>Figure 2.6</b> Examples of inner-sphere phosphate adsorption on metal centers.....	44

<b>Figure 2.7</b> The four reaction and transport processes important in sorption by porous materials.....	49
<b>Figure 2.8</b> Schematic diagram of the structure of layered double-hydroxides .....	55
<b>Figure 2.9</b> Simplified representation of potential copper species in Cu-ZSM-5 .....	63
<b>Chapter 3 Methodology</b>	<b>70</b>
<b>Figure 3.1</b> Breakdown of various forms of P in aquatic system. ....	74
<b>Figure 3.2</b> UV-Vis absorbance spectra for five sodium phosphate standard solutions using the molybdenum blue reaction for orthophosphate determination..	85
<b>Figure 3.3</b> Representative calibration curve for spectrophotometric determination of orthophosphate using the molybdenum blue reaction .....	86
<b>Figure 3.4</b> Calibration curve obtained for spectrophotometric determination of copper using the Hach Copper TNT860 test kit. ....	88
<b>Chapter 4 Results</b>	<b>94</b>
<b>Figure 4.1</b> Summary of validation studies for the molybdenum blue assay used in this dissertation.....	97
<b>Figure 4.2</b> XRD patterns of the four synthesized Cu-ZSM-5 zeolites used in this study, along with selected patterns for H-ZSM-5 and Na-ZSM-5 .....	101
<b>Figure 4.3</b> SEM images for Cu-ZSM-5-(11) .....	102
<b>Figure 4.4</b> Energy-dispersive X-ray spectroscopy (EDS) spectra obtained for Cu-ZSM-5-(11).....	104
<b>Figure 4.5</b> ATR-FT-IR absorbance spectra for pristine Cu-ZSM-5 and samples after phosphate adsorption across the range of initial phosphate concentrations studied.....	107
<b>Figure 4.6</b> Room temperature phosphate adsorption performance of Cu-ZSM-5 at 10 mg-P/L over 24 hours. ....	109

## LIST OF FIGURES

<b>Figure 4.7</b> Phosphate adsorption isotherms obtained for Cu-ZSM-5 at $20 \pm 2$ °C and neutral pH .....	111
<b>Figure 4.8</b> Phosphate adsorption isotherm data for Cu-ZSM-5 fitted to the empirical Freundlich model by non-linear least squares regression.....	114
<b>Figure 4.9</b> Effect of initial pH on phosphate adsorption over a wide range of initial pH values for Cu-ZSM-5 and Na-ZSM-5 at Si/Al ratios of 11 and 42 ..	116
<b>Figure 4.10</b> Change in pH of solutions due to the addition of ZSM-5 sorbents and phosphate adsorption for a wide range of initial pH values .....	118
<b>Figure 4.11</b> Phosphate adsorption on Cu-ZSM-5 at Si/Al ratios 11 and 42 evaluated as a function of the final solution pH.....	122
<b>Figure 4.12</b> Leaching of copper from Cu-ZSM-5 sorbents into solution due to phosphate adsorption over a range of initial solution phosphate concentrations, up to 1500 mg-P/L.....	124
<b>Figure 4.13</b> Phosphate adsorption isotherms for Cu-ZSM-5 at $20 \pm 2$ °C and neutral pH, normalized by copper content.....	127
<b>Figure 4.14</b> Equilibrium phosphate adsorption isotherm data for Cu-ZSM-5 fitted to the Freundlich and Langmuir models by non-linear least squares regression.....	131
<b>Figure 4.15</b> Effect of pH (A: initial, B: equilibrium) on phosphate adsorption for Cu-ZSM-5, normalized by copper content .....	132
<b>Figure 4.16</b> Phosphate adsorption data for Cu-ZSM-5 fitted to kinetic models by non-linear least squares regression, normalized by copper content.....	137
<b>Figure 4.17</b> Phosphate adsorption data for Cu-ZSM-5, normalized by copper content, with $t^{1/2}$ as the abscissa for evaluation of the intra-particle diffusion kinetic model. ....	138
<b>Figure 4.18</b> Characterization of Cu sites in copper-exchanged ZSM-5.....	141
<b>Figure 4.19</b> Dependence of equilibrium phosphate adsorption properties at tested conditions on Cu density .....	142

<b>Figure 4.20</b> Equilibrium phosphate adsorption parameters equalized by $\delta \cdot \eta_{\text{Cu}\cdots\text{Cu}} + (1 - \eta_{\text{Cu}\cdots\text{Cu}})$ .....	146
<b>Figure 4.21</b> Copper dimer fraction derived from equilibrium phosphate adsorption and applied to kinetic data .....	147
<b>Figure 4.22</b> TPR profiles for five Cu-ZSM-5 zeolites at full exchange referenced in Figure 4.21 .....	148
<b>Chapter 5 Discussion</b>	<b>150</b>
<b>Figure 5.1</b> Sketch of proposed phosphate adsorption arrangement in Cu-ZSM-5 by dimer sites (left) and monomer sites (right) in a 10-membered ring of the zeolite.....	159
<b>Chapter 7 Supplementary</b>	<b>167</b>
<b>Figure 7.1</b> Simplified scheme for the enzymatic hydrolysis of a phosphomonoester substrate .....	169
<b>Figure 7.2</b> Summary of the phosphomonoester substrates utilized in this study .....	173
<b>Figure 7.3</b> The leaving group dependence for catalytic dephosphorylation by cerium oxide nanoparticles at five different temperatures.....	175

# Chapter 1 Introduction

## 1.1 The importance of phosphorus

Phosphorus (P) is an essential macronutrient for plant growth and a key element in all biological systems, primarily through its importance in the structures of biomolecules (e.g., nucleic acids, phospholipids) and role in metabolic reactions (e.g., ATP, NADPH) [1]. Unlike nitrogen (N), phosphorus is not found in the atmosphere (apart from negligible amounts of phosphine (PH<sub>3</sub>) gas produced by certain microorganisms or in particulates carried by eroding winds [2]) and its biogeochemical cycle—illustrated in Figure 1.1—is rate-limited by processes including rock formation and uplift that occur on geologic time scales. For these reasons, phosphorus extracted from the ground is increasingly being viewed as a critical, non-renewable resource in a similar vein to conventional oil [3], [4].

The phosphorus used in agriculture—by the far the biggest market, fertilizer and feed utilize approximately 90% of all mined phosphorus [5]—is applied in the form of phosphate, H<sub>x</sub>PO<sub>4</sub><sup>(3-x)-</sup>, and derived from mineral-rich rock. Roughly 95% of the phosphorus in the Earth's crust is found in the poorly soluble calcium phosphate



## INTRODUCTION

mineral apatite,  $\text{Ca}_{10}(\text{PO}_4)_6\text{X}_2$ , where X is F in fluorapatite, OH in hydroxyapatite, Cl in chlorapatite [2]. Although P is relatively scarce in the biosphere—it presents at approximately 1180 ppm in the lithosphere, less abundant than titanium or potassium but more so than manganese or sulfur—the element is found at relatively high levels in vertebrates, mainly as a hydroxyapatite ceramic in bones and teeth. A typical adult human contains approximately 550 g P in this form, with an additional 80 g P found within soft tissues as soluble phosphate, nucleic acids, and enzymes [2].

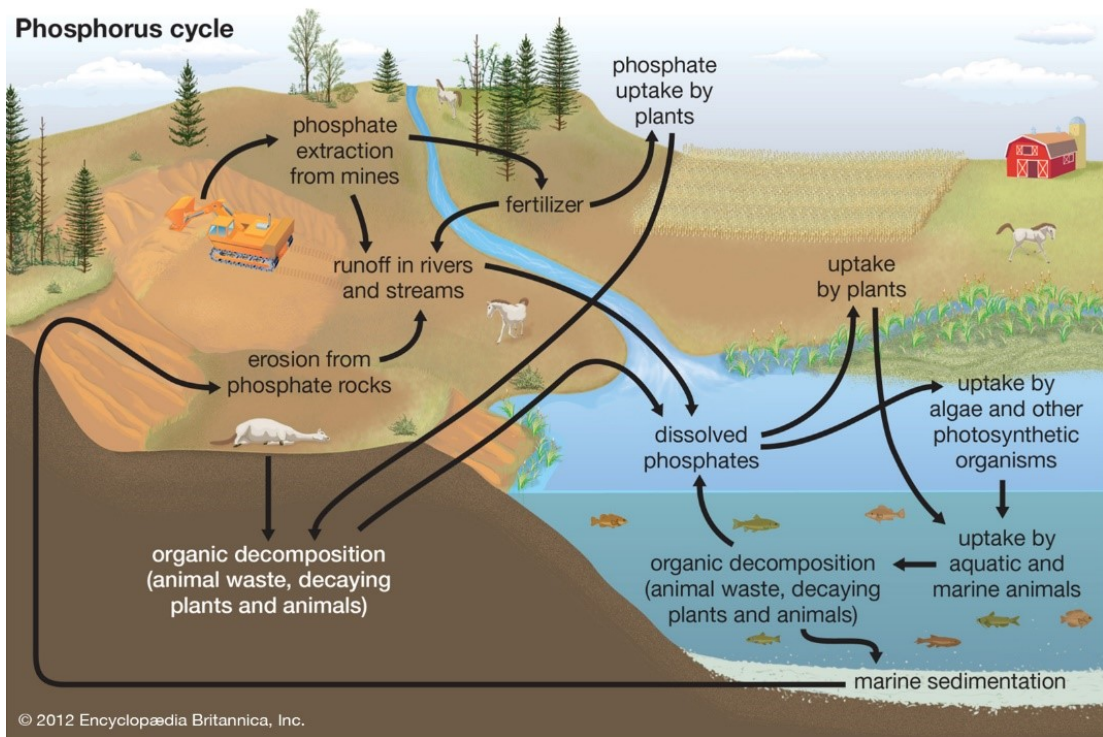


**Figure 1.1** Illustration of the phosphorus biogeochemical cycle [6]. Phosphate-rich rock is mined and processed (primarily) into agricultural fertilizer. This source is replenished by the formation of new rock and uplift to the earth’s surface, which occurs on geologic time scales. In natural systems, phosphorus is transported in the liquid and solid phases; it does not enter the atmosphere in significant amounts.

## INTRODUCTION

The mass extraction and transport of P, as with most minerals, has been driven by human demand. Current levels of food production that sustain the global population of over seven billion people would not be possible without the fertilizer and feed inputs that sustain crops and livestock around the world. Therefore, notwithstanding significant changes to current agricultural practices and human diets (to name only a few possibilities), ensuring continued availability of phosphate is of critical importance to the well-being of humanity. Figure 1.2 and Figure 1.3 depict the current state of affairs with regards to mine production rates and current reserves of phosphate rock for a selection of countries, respectively. Here, mineral reserves have been defined by the source as the portion of currently known mineral base reserves which could be economically extracted or produced with current technology under current market conditions. There are a few key points to be observed. Firstly, both production and reserves are highly concentrated geographically: China, Morocco & Western Sahara and the United States accounted for over 70% of annual production in 2019. In terms of reserves, the concentration is even more striking, with 70% held by a single country (or region, acknowledging the disputed status in the area of Morocco & Western Sahara). This level of concentration in both production and reserves already greatly exceeds that for the oil market [5], which raises questions regarding the impacts (both negative and positive) on Morocco & Western Sahara and the rest of the world as reserves in other countries are depleted.

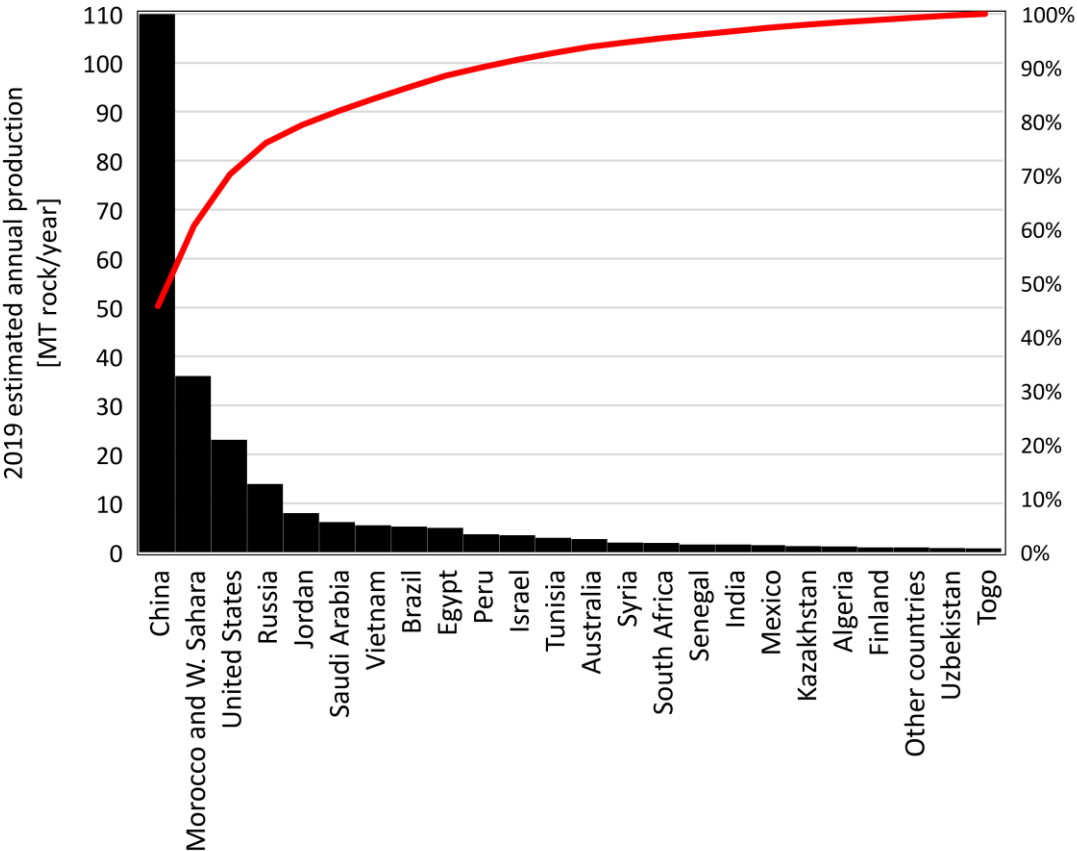


**Figure 1.2** Pareto chart showing the world’s current mine production of phosphate rock, based on estimated 2019 annual mine production. Approximately 70% of production can be attributed to three countries: China, Morocco & Western Sahara, United States. Underlying data obtained from the USGS Mineral Commodity Summaries 2020 [7].

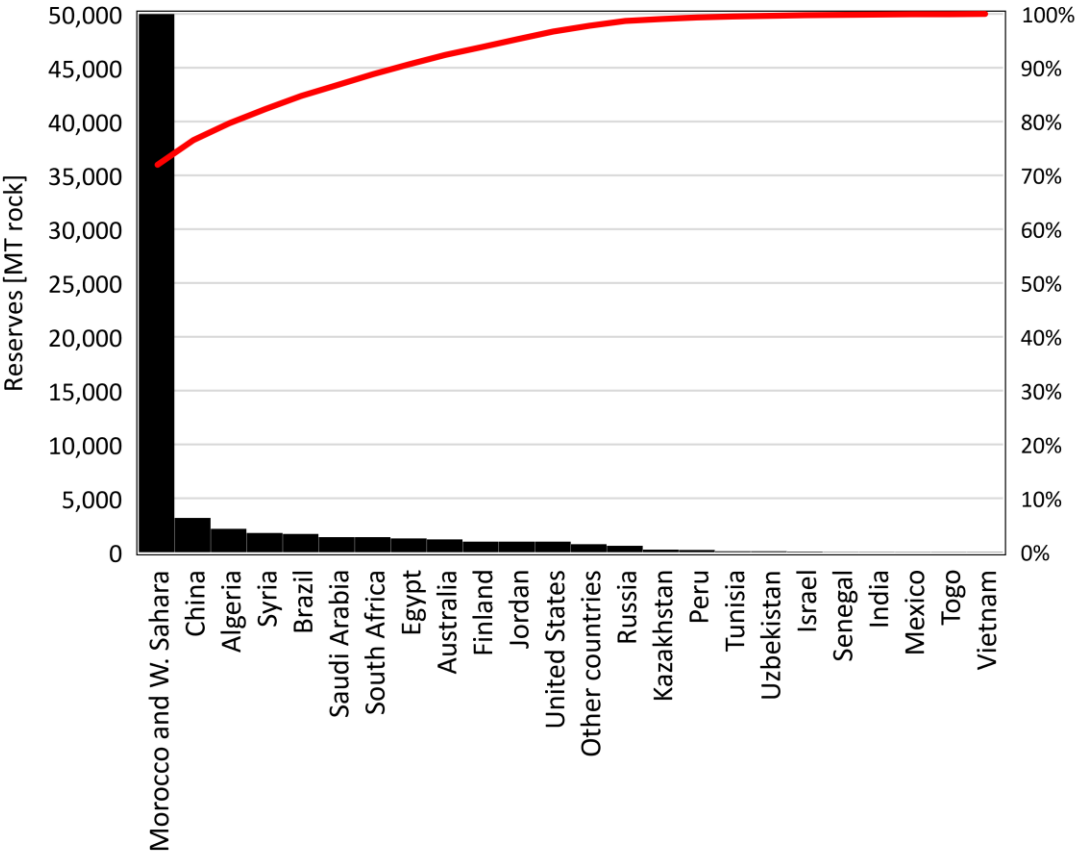


**Figure 1.3** Pareto chart showing the world’s current reserves of phosphate rock. Reserves of phosphate rock are concentrated in Morocco and Western Sahara. Underlying data obtained from the USGS Mineral Commodity Summaries 2020 [7].

Secondly, Figure 1.2 and Figure 1.3 reveal that current production rates are not aligned with reserves. This discrepancy can be quantified by calculating a simple reserves-to-production ratio (R/P), as shown in Table 1.1. While accepting that neither production rates nor reserves are necessarily constant—reserves can increase with advancements in mining technology or favorable market conditions—the R/P value, in units of years, provides a simple metric for assessing the sustainability of phosphate rock production.

Table 1.1 shows that according to the R/P metric, the world has approximately 300 years before phosphate reserves would be depleted at current production rates. China (which accounted for 46% of production in 2019) only has ~30 years of reserves, and the United States less than 45 years. The data suggests over the next 50 years, there will necessarily be a continued transition in terms of where phosphate rock is sourced and that increased global cooperation will be required. While there is considerable uncertainty regarding exactly how long it would take to exhaust all mineable phosphate rock, most scientists agree that depletion of these reserves will become a significant human and economic issue within the current or next centuries [8], [9].

**Table 1.1** Data on the sustainability of global phosphate rock production. Countries are listed in order of increasing R/P, used here as an approximate indication of the length of time (in years) current mine production of phosphate rock could be sustained. Data sourced from the USGS Mineral Commodity Summaries 2020 [7].

Region	Reserves/Production [years]	Reserves [GT rock]
Vietnam	5	30
Israel	18	62
Mexico	20	30
India	29	46
China	29	3,200
Senegal	31	50
Tunisia	33	100
Togo	38	30
Russia	43	600
United States	43	1,000
Peru	57	210
Uzbekistan	111	100
Jordan	125	1,000
Kazakhstan	200	260
Saudi Arabia	226	1,400
Egypt	260	1,300
<b>World</b>	<b>289</b>	<b>69,488</b>
Brazil	321	1,700
Australia	444	1,200
South Africa	737	1,400
Other countries (not listed)	770	770
Syria	900	1,800
Finland	1,000	1,000
Morocco and W. Sahara	1,389	50,000
Algeria	1,833	2,200

## **1.2 Phosphorus in the environment: pollutant and resource**

Despite its status as a valuable commodity in the form of phosphate rock, phosphorus is often considered a pollutant once it enters waterways. By examining the pathways P takes in the human-modified phosphorus cycle and its role in eutrophication, we can gain a better understanding of how traditional waste and other flows can be viewed as untapped resources.

### **1.2.1 Flow of phosphorus in nature and the human impact**

While increased phosphate rock production and the application in agriculture has been a boon for the growth of human populations around the world, it's also facilitated an increasingly problematic anthropogenic pathway for phosphate entry to aquatic ecosystems. Figure 1.1 provides a simplified illustration of how phosphate-rich fertilizer applied to soils contributes to the mobilization of P (both in particulate and dissolved forms) into rivers and streams, in addition to the natural erosion of phosphate rock. Other significant pathways—particularly for dissolved P (not illustrated in Figure 1.1)—include insufficiently treated municipal or industrial waste-water and sewage discharged into oceans, rivers, lakes and other water bodies. Regardless of the transport pathway, the main consequence of this excessive P loading is artificial eutrophication of waterways leading to significant and sometimes devastating disruption to the natural ecosystem.



Table 1.2 provides some numerical detail on the relative magnitudes of P flows in the world's phosphorus cycle and the intensification of natural flows indirectly caused by purely anthropogenic fluxes. The data shows that in the absence of inorganic fertilizer usage during preindustrial times, there was relatively low intensification of P flows that transported the element to the world's waterways. However, by the end of the 20<sup>th</sup> century, 15 MT-P/year of inorganic fertilizers were being applied to the world's greatly expanded agricultural lands and order-of-magnitude increases had occurred in all other human-induced P flows (e.g., human and animal wastes). This has been accompanied by two- or three-fold increases in erosion losses by water and transport of both particulate and dissolved P through river systems.

It is important to point out that the increased total P entering streams is not a one-to-one result purely attributable to the increased application of fertilizers—a point which is sometimes forgotten in cursory discussions of the subject—but a combination of factors. The massive increase in P flow associated with erosion is a consequence of land converted and used to plant annual crops being far more susceptible to the processes of erosion than forests, grasslands and other natural floors [2], [5], [10]. Erosion occurs because raindrops (and wind) have sufficient kinetic energy to dislodge surface soil particles and transport them away. While soil structure and topography impact erosion rates, the vegetative cover on top of the soil (e.g., canopies, living and dead biomass,

## INTRODUCTION

established root systems) plays a critical role in preventing erosion. When this cover is removed—as is common in preparing crop lands—erosion rates can increase dramatically; reducing cover from 100% to 1% can lead to ~200 fold increases [10]. It's been reported that 75 to 80% (and frequently, greater than 90%) of soil erosion relating to crop lands can be accounted for by the loss of vegetative cover [2]. Therefore, combined with the application of P-rich fertilizers to the topsoil, erosion by water is able transport the vast quantities of P delineated in Table 1.2.

**Table 1.2** Flows of P and the large anthropogenic impact on the phosphorus cycle (numerical values are all megatonnes P per annum). Adapted from Smil [2].

<b>Natural flows</b>	<b>Natural</b>	<b>Preindustrial (1800)</b>	<b>Recent (2000)</b>	<b>Intensification (recent vs. natural)</b>
Erosion - <i>wind</i>	<2	<3	>3	~50%
Erosion - <i>water</i>	>8	>12	>27	~240%
River transport - <i>particulate P</i>	>6	>8	>20	~230%
River transport - <i>dissolved P</i>	>1	<2	>2	~100%
Biomass combustion (e.g., fires)	<0.1	<0.2	<0.3	~200%
<b>Anthropogenic flows</b>				
Crop uptake		1	12	
Animal wastes		>1	>15	
Human wastes		0.5	3	
Organic recycling		<0.5	>6	
Inorganic fertilizers			15	

### 1.2.2 Eutrophication

Eutrophication—from the Greek for “well-nourished”—in freshwater systems is driven three major nutrients: phosphorus, nitrogen and carbon. However, P tends to be of primary concern in most systems because it not as easily obtainable (though rainfall can contribute) at the water-air interface and has a large multiplying effect on the production of phytomass [2], [11]. One highly visible example of this is the significant contribution to excessive algal growth (e.g., algal blooms with varying degrees of toxicity), which can destabilize natural ecosystems, reduce dissolved oxygen concentrations, cause large fish kills and catastrophically harm communities dependent on aquaculture [12]. Eutrophication affects a diverse range of ecosystems across the globe, including the Chesapeake Bay in the United States, the Baltic Sea, and the Great Barrier Reef to name but a few [13]–[15]. An in-depth review of the multitude of algal species, their toxicity profiles and the detailed mechanisms by which aquatic ecosystems are damaged is beyond the scope of this dissertation, and the reader is directed to the cited literature. However, it’s sufficient to say that the unsolved problem of eutrophication is well-accepted and has played an important role since the late 1960s in bringing issues of environmental conservation into the public sphere [2].

Dissolved P concentrations of greater than 10 ppb can lead to eutrophication, though the loading—mass of P per unit area of water surface—combined with retention time

of the water body is a critical consideration [2]. The most significant contributions of dissolved P come from municipal or industrial waste-waters (point sources; detergents and sewage are rich in P) and previously discussed runoff from agriculture (diffuse sources). While leaching or percolation of nutrients into subsurface waters from agricultural lands is an accepted and significant pathway for removal of N, it is a less important pathway for P due to better retention in most soils as it moves deeper [2], [11]. Although the magnitude of dissolved P transport in streams is relatively small (>2 MT/year; see Table 1.2), the increase from natural levels—approximately double—is substantial given the sensitivity of waters to even small increases in P loading. Indeed, these diffuse sources alone (i.e., if point sources were controlled) provide sufficient P loadings to cause eutrophication [11].

Particulate P can also contribute to eutrophication by acting as a store, with dissolved P released to phytomass through solid-liquid equilibrium processes or biological action, as shown in Figure 1.4. However, not all particulate P transported through streams reaches lakes, oceans or other large bodies; at least 25% is redeposited, which accounts for the 7 MT/year difference between water erosion and river particulate transport observable in Table 1.2.

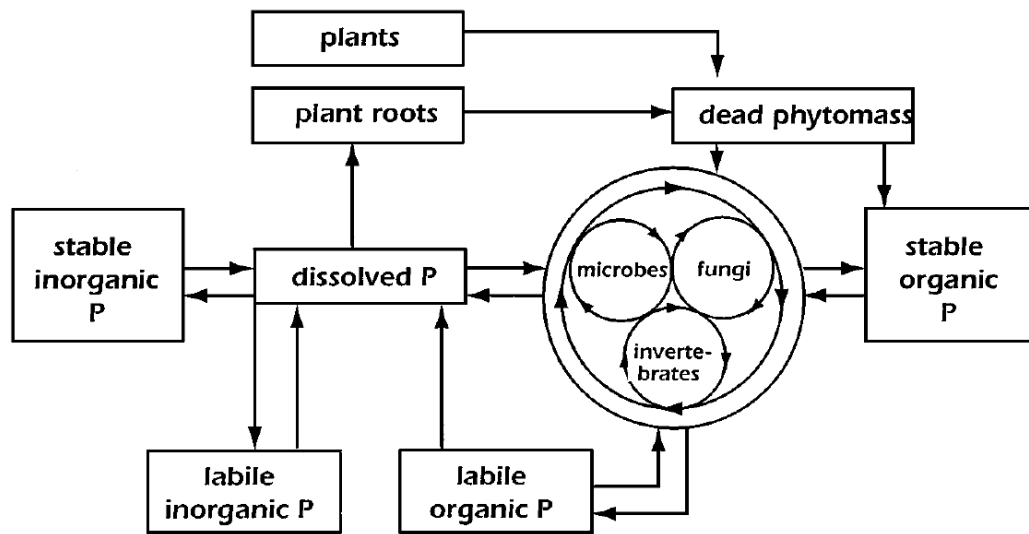


**Figure 1.4** Phosphorous equilibrium and cycles in soil. Diagram from Smil [2] based on illustration in Paul & Clark [16].

### 1.3 Solutions to the phosphorus problem

The information presented in the preceding sections has established the seriousness of the phosphorus problem, both from environmental and economic perspectives. This raises the question of what can be done. Unfortunately, phosphorus as a macronutrient has no substitute. However, as alluded to in section 1.2, phosphate rock in the ground is not the only potential source if we consider the other flows that occur. Alternatives—referred to here as secondary sources—include excreted human waste, livestock wastes not harvested for manure, domestic and industrial waste-water, sewage sludge, crop residue, agricultural runoff, digested algae, food waste, spent detergents and mine wastes [17]–[22]. Naturally, most of these sources are not independent and represent various parts of the human-modified phosphorus cycle. The grand challenge is to engineer a closed loop in the anthropogenic phosphorus cycle—in other words, recover and recycle phosphorus from secondary sources into fertilizers and other products—such that the reliance on traditional phosphate rock reserves is reduced to a level that can be sustained indefinitely.

While the focus on a closed-loop solution is laudable—and remains the focus here—it should not be assumed that it's the only path available in addressing the potential shortage in phosphorus. Lower hanging fruit include improvements in mining, processing and fertilizer production—where losses of P are estimated at ~35% [9]—

and addressing the astonishing levels of food wastage—1.3 billion tonnes per year or roughly one third of global production—especially in North America, Oceania, Europe and industrialized Asia where consumer-level per capita wastage is ~100 kg/year (versus ~10 kg/year in the so-called developing world) [23]. Analysis has also shown that a mere ~25% reduction in the quantity of meat eaten by those in rich countries would lead to ~10% reduction in the need for phosphate fertilizers without any impact on nutrition or need for new investment [2]. As a more technical solution, genetic modification and selecting or developing cultivars to improve P use efficiency by plants at the crop stage is a direction agricultural science can offer for addressing the phosphorus problem on the demand side [24]. It is likely that the best approach to tackling the complicated issues of phosphorus supply and environmental pollution will lie in adopting several strategies that address inefficiencies at every point of the human-modified phosphorus cycle.

### **1.3.1 The separation problem**

Recovering phosphorus from secondary sources generally boils down to a separation problem. Since orthophosphate—dissolved inorganic P or  $H_xPO_4^{(3-x)-}$ —is the form typically available to phytomass and most easily converted to fertilizer by pairing with a suitable cation (calcium, ammonium or potassium [2]), it is of particular interest for recovery applications. This applies whether orthophosphate is targeted directly in point or diffuse secondary sources, or as an intermediate processing step where



orthophosphate is being liberated from particulate or organic form. Therefore, separation of dissolved inorganic phosphate from an aqueous phase is an important technical challenge.

Due to the above motivations, there have been numerous studies on the development of materials capable of reversibly removing phosphate from solution via adsorption. Several classes of materials have received interest, including zeolites, biomass, biochars, synthetic iron oxides such as goethite and akaganéite, and magnetic materials such as magnetite nanoparticles [21], [25]–[30]. Each material has its own advantages and the authors of the cited works present various rationales for their selection. Some of these materials will be reviewed in further detail in the literature review of this dissertation.

## 1.4 Zeolites

Zeolites—microporous, crystalline aluminosilicates amenable to modification through green chemical techniques—are one proposed class of material for the recovery of phosphate through reversible adsorption. The name zeolite dates to 1756 and comes from the Greek for “boiling stone”, a reference to the observed steaming and frothing of a stone (probably stilbite) releasing adsorbed water after being subject to heat [31]. Zeolites have a 3D framework structure resulting in well-defined and uniform pores often less than 1 nm in size (i.e., molecular length scale). They are composed of  $\text{TO}_4$

tetrahedra—where T is either a silicon, aluminum (or phosphorus for aluminophosphates)—that share all four vertex oxygen atoms. The unit cells of zeolites—secondary building units (SBU) composed of an arrangement of the  $\text{TO}_4$  tetrahedra—bridge or fuse to create a variety of repeating framework structures; well over 200 unique frameworks (each distinguished by a three-letter code) have been identified, though the majority are not found in nature [32]. Zeolites are often referred to as molecular sieves; the pore openings—size set by the particular framework structure—are sufficiently small to selectively allow certain molecules inside the channel or cage structure while excluding others. Therefore, zeolites have become extremely important in catalysis and adsorption applications. Figure 1.5 shows examples of the pore openings for some common zeolite frameworks.

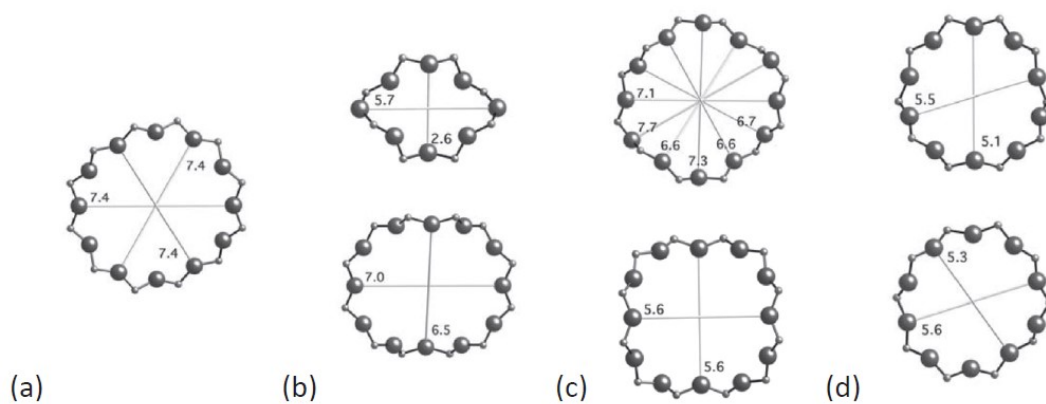


**Figure 1.5** Pore openings of selected zeolites [32]. The larger spheres represent T atoms, while the smaller spheres are the connected oxygen atoms. Pores with a greater number of T atoms are larger in size. (A) 12-ring opening, FAU zeolites. (B) 8-ring and 12-ring opening, MOR zeolites. (C) 12-ring opening, BEA zeolites. (D) 10-ring opening, MFI zeolites.

Zeolites can have varying amounts of aluminum substitution (i.e., where Si is replaced with Al in  $\text{TO}_4$ ). Typically, this is quantified by the Si/Al or silica-alumina ratio per the generalized formula  $\text{M}_{2/n}\text{O}\cdot\text{Al}_2\text{O}_3\cdot y\text{SiO}_2\cdot m\text{H}_2\text{O}$ , where M is the cation that balances the charge difference between  $\text{Al}^{3+}$  and  $\text{Si}^{4+}$  and n is the valence of M [33]. The loosely held cations maintaining the charge neutrality of the zeolite play an important role in the sought-after properties of the material. These species can be used for ion exchange purposes and also serve as sites to interact with polar molecules or form active adsorption/catalytic sites in their own right; lower Si/Al ratios (i.e., more aluminum) generally results in higher cation exchange capacity and increased hydrophilicity. The unique properties of zeolites have led to their application in a host of fields: oil and gas processing, petrochemicals, adsorbents, gas separation, detergents, agriculture and horticulture to name a few [34].

#### **1.4.1 Metal-exchanged zeolites**

Metal-exchanged zeolites can be defined as those materials where the charge balancing cation (typically  $\text{H}^+$ ,  $\text{Na}^+$  or  $\text{NH}_4^+$ , depending on the synthesis method or exchange method) is replaced with a metal cation (typically a transition metal) for the purpose of obtaining an enhanced adsorption, catalytic or other activity. Typically, the substitution is accomplished using relatively simple wet ion exchange techniques, though solid-state ion exchange and chemical vapor deposition have also been used [35]. Cations can also

be introduced into the zeolite through isomorphous replacement of Si or Al in the framework itself, though that type of modification is excluded from the definition here.

The interest in metal-exchanged zeolites has been largely driven by the desire to replicate the success of the standard three-way catalytic converter—a device fitted on gasoline-powered vehicles since the 1980s that oxidizes CO and unburned hydrocarbons while reducing NO<sub>x</sub> species to nitrogen—in diesel automobile engines. Although diesel engines have higher thermal efficiency—they typically run at much higher compression ratios than their gasoline counterparts—they run much leaner (i.e., higher air-to-fuel ratio). Under these conditions with excess oxygen, the three-way catalytic converter is unable to reduce NO<sub>x</sub> in the exhaust and emissions of the harmful gases would exceed acceptable limits. Therefore, over the past two decades there has been a great push to overcome this limitation, with significant progress made using metal-exchanged zeolites—primarily utilizing copper or iron cations [35]–[37]—for the selective catalytic reduction of NO<sub>x</sub> with ammonia (NH<sub>3</sub>-SCR) [36].

Landmark discoveries were made in the late 1980s and 1990s that showed copper-exchanged ZSM-5—Cu-ZSM-5—was catalytically active in the decomposition and selective catalytic reduction of NO [38], [39]. Especially with respect to the ammonia-mediated SCR of NO<sub>x</sub>, many years of research in the field has concluded that although the fresh catalyst displays impressive performance, deactivation at typical application

conditions (e.g., long-term treatment of lean-burn automotive exhaust gas) renders Cu-ZSM-5 impractical for commercialization [36]. Indeed, other materials such as copper-containing CHA zeolites have addressed this performance gap and were slated for commercialized in certain applications almost a decade ago [36], [40]. In these systems, the ammonia is typically provided by injecting aqueous urea into the exhaust stream. This is illustrated in Figure 1.6, which shows a recent commercialized implementation of NH<sub>3</sub>-SCR in an emissions control system. Despite the subsequent success of small pore Cu-CHA zeolites in addressing some of the critical issues with Cu-ZSM-5 in SCR automotive applications, the latter remains an active area of study. Owing to its complexity, the exact nature of the active catalytic sites in copper-exchanged ZSM-5—generally accepted to be a Cu dimer of generalized form [Cu–O<sub>x</sub>–Cu]<sup>2+</sup> bridging framework Al T-sites and formed from copper ions introduced through ion exchange—is still not fully understood and therefore continues to attract academic interest [41]–[45].

In trying to answer questions about the copper speciation in Cu-ZSM-5, typical methods of investigation often use the adsorption of gaseous probe molecules (e.g., CO, N<sub>2</sub>, NO, NH<sub>3</sub>) combined with spectroscopic analysis (e.g., infra-red spectroscopy) to study the catalyst's surface [36]. However, the adsorption of anionic species from the liquid phase—aqueous inorganic phosphate, for example—has not been previously investigated for its potential as a probe of Cu sites in copper-exchanged ZSM-5.

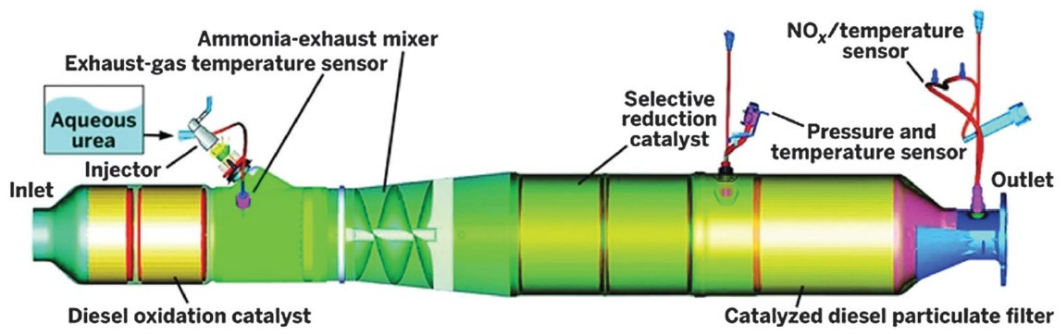


**Figure 1.6** Schematic of the NH<sub>3</sub>-SCR based emissions control system on a 2011 Ford Super Duty diesel pickup truck [36].

## 1.5 Research objectives and dissertation overview

The primary objective of the research work presented in this dissertation is to complete an in-depth study of the inorganic phosphate anion adsorption properties of copper-exchanged zeolites—with specific focus on Cu-ZSM-5—in order to answer the following questions:

1. To what extent can copper-exchanged zeolites perform as sorbents for dissolved inorganic P, and under what conditions (e.g., P concentration, zeolite Si/Al ratio, pH) might they be considered applicable for phosphate recovery from environmental, waste, or processing flows?
2. What is the relationship between the phosphate anion adsorption properties of copper-exchanged zeolites and their structure, and can these adsorption properties be used as a probe for specific active sites (e.g., Cu dimers), thus presenting a new and unique method for understanding this important class of materials?

Having introduced the necessary background, motivating factors and guiding objectives for this research, this dissertation will follow with a review of selected literature to establish the current state of the art in P recovery by sorption and characterization of active Cu sites in copper-exchanged zeolites. Following this, a detailed description of



## INTRODUCTION

the methodology used to address the research objectives will be presented; the level of detail will be such that the reader may fully understand how the results were obtained, assess the limitations, and accurately repeat the experimental work. After presenting the results and discussing their implications in the context of the stated research objectives, the dissertation will conclude with final remarks and a consideration of further work that may be of value.

## **Chapter 2 Literature review**

The purpose of this literature review is to put the research presented in this dissertation into context. By conducting a carefully selected review of recent advances, competing technologies and current industrial practice, the originality and value of this work will be established. Specifically, two broad areas will be addressed: sorption-based methods for inorganic dissolved P recovery, and characterization of active Cu sites in copper-exchanged zeolites.

### **2.1 State of the art in inorganic dissolved phosphate recovery**

Owing to the long-standing realization that excessive phosphate discharge into waterways has significant negative impacts on the environment, many proven phosphate removal technologies already exist. However, of those currently in use, most tend to focus on meeting environmental regulations rather than creating a closed-loop recycling system for P [18]. Therefore, before reviewing the literature on novel sorption-based methods, a brief overview of traditional methods used in waste-water treatment will be presented to highlight both their merits and deficiencies in achieving this goal.

## 2.1.1 Traditional removal techniques

### 2.1.1.1 Metal salt dosing

Perhaps one of the most obvious solutions to removing dissolved inorganic phosphate is by simple precipitation with an appropriate cation, followed by solid-liquid separation. Indeed, this method has been in use since the 1950s in waste-water treatment [46], and is typically effected with metal salts of aluminum and iron. Aluminum salts used include alum ( $\text{Al}_2(\text{SO}_4)_3 \cdot 14\text{H}_2\text{O}$ ) and aluminum chloride ( $\text{AlCl}_3$ ); iron salts include ferric chloride ( $\text{FeCl}_3$ ) and ferrous chloride ( $\text{FeCl}_2$ ) [47]. Salts are typically dosed during secondary treatment (though dosing can occur at other stages if required) and the precipitated iron or aluminum phosphates are removed along with biosolids as sludge after clarification, as illustrated in Figure 2.1.

Although chemical dosing is an effective and simple method for reducing dissolved inorganic P concentrations in the effluent, the precipitate is generally not considered a useful material for reuse as a fertilizer, primarily due to the reduced bioavailability of P [18], [46], [48].

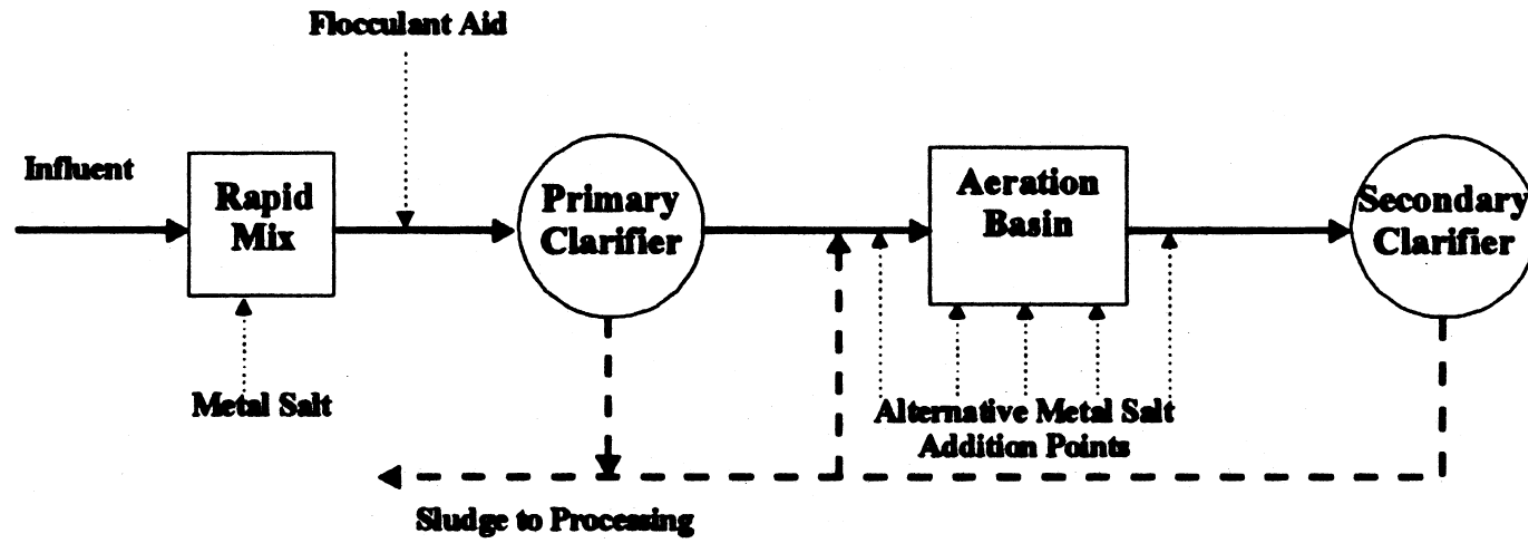


Figure 2.1 Chemical dosing for P removal in waste-water treatment. From Morse *et al.* [46].

### 2.1.1.2 Biological removal

Biological removal of dissolved inorganic P is another well-established technique used in waste-water treatment plants for almost as long as chemical dosing [46]. The primary basis of this method is “luxury” uptake of P—utilization significantly greater than required for regular growth—by microorganisms in activated sludge exposed to the right conditions [49]. Figure 2.2 shows the process configuration of a simple biological P removal system. An anaerobic (no nitrates or oxygen) or anoxic treatment zone is introduced prior to the aerobic step in secondary treatment, where *Acinetobacter* or other polyphosphate accumulating organisms (PAO) consume volatile fatty acids introduced by pre-fermentation of the sludge or addition of acetic acid to achieve a sufficient carbon load. The energy requirement for this accumulation of carbon into intracellular polyhydroxyalkanoates (PHA) is provided by hydrolysis of stored intracellular polyphosphates, which releases orthophosphate into solution. In the following aerobic zone, the PAOs oxidize their PHA for energy and accumulate dissolved orthophosphate as polyphosphate; this orthophosphate uptake is in addition to that consumed in new PAO cell growth. After this aeration zone, a recycle stream of the activated sludge is returned the anaerobic portion, with excess sludge removed from the system once loaded with P to remove it from the system and avoid excessive orthophosphate concentrations in the cycle. Overall P removal can approach 80 to 90%,

## LITERATURE REVIEW

though because removal can be variable, biological removal is often accompanied by chemical dosing when specific effluent standards are being targeted [46], [50].

Enhancements, modifications and side stream processes have been incorporated into various commercialized versions of biological P removal technology, such as Phostrip. This particular process involves removal of P from a side stream taken off the recycled activated sludge stream; a portion of the P-loaded sludge is exposed to a carbon source triggering release of orthophosphate from the PAOs which is removed by chemical precipitation. Compared to simple chemical dosing, biological P removal involves significantly more complicated treatment plant configurations, process control and sludge handling [46], [47], [50]. Although P-loaded sludge should in theory be more a biocompatible source of P compared to chemical sludges, challenges for use as a direct fertilizer include variability in nutrient content and concerns regarding contamination.

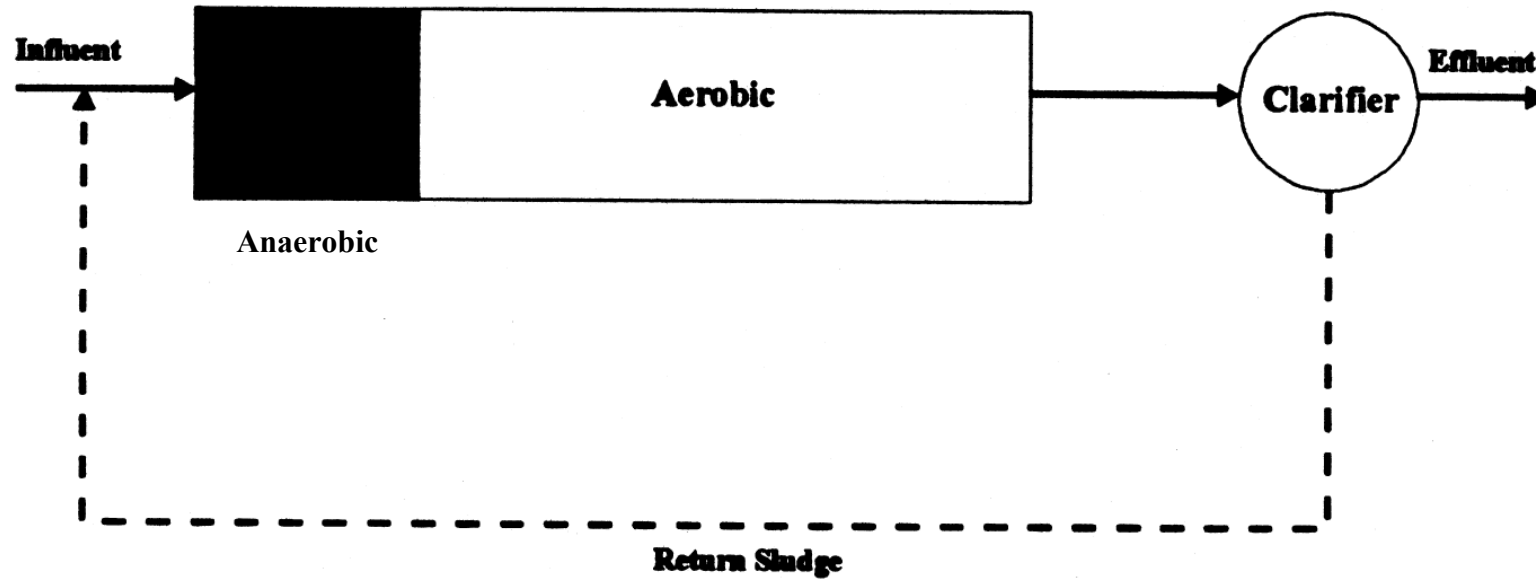


Figure 2.2 Simplified process illustration of biological P removal. Adapted from Morse *et al.* [46].

### 2.1.1.3 Crystallization

Crystallization technologies for inorganic dissolved phosphate removal were first developed in the 1970s to combat stricter phosphate emission standards and consideration of the need to produce more desirable by-products [46]. The premise of the technique is to crystallize calcium phosphate from a P-rich liquor using seeding grains and favorable pH conditions. Depending on pre-existing calcium conditions, the pH is adjusted with sodium hydroxide or calcium hydroxide addition to the crystallization reactor. The relationship between solubility and pH is shown in Figure 2.3.

Increasing the pH to alkaline conditions promotes fast rates of crystallization, facilitating relatively short residence times and reasonably sized fluidized bed reactors. After sufficient growth, the calcium phosphate grains are recovered from the reactor and replaced with fresh seed grains fed. Figure 2.4 depicts an example of a reactor system used in this process. Calcium carbonate precipitation in the reactor is combatted by prior degasification steps (e.g., addition of sulfuric acid to facilitate removal as carbon dioxide), while post-filtration aids in removal of residual calcium phosphate to achieve lower effluent P concentrations [46].



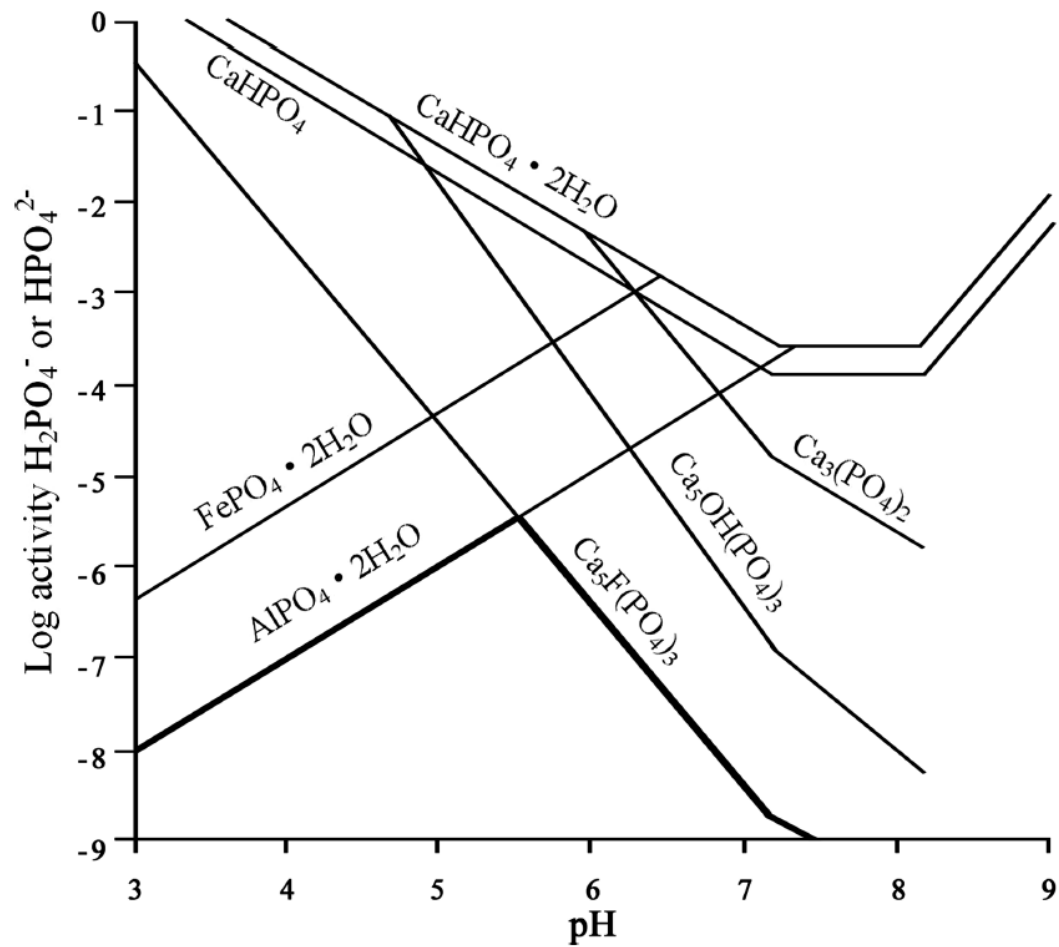


**Figure 2.3** Solubility of phosphate species important to water treatment and soil systems. Reproduced from Liu et al. Plot from Liu *et al.* [51], based on Schlesinger [52].

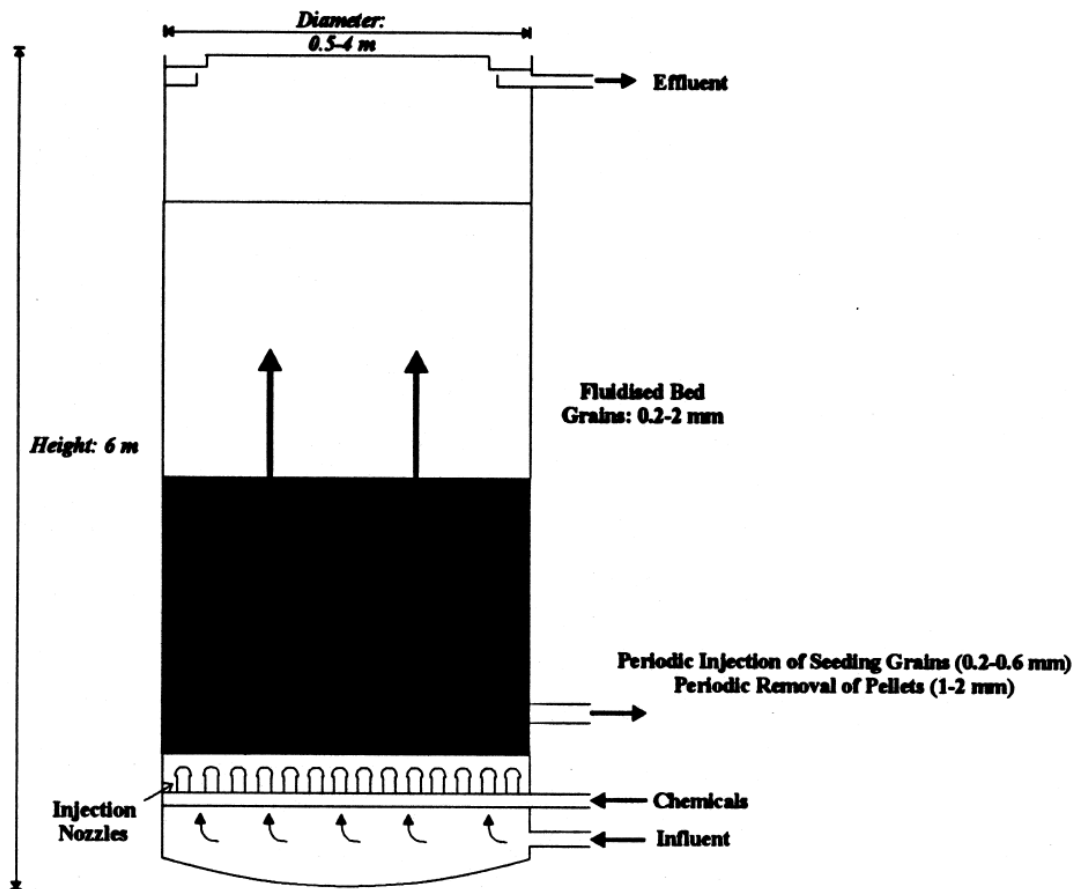


**Figure 2.4** Simplified schematic of the fluidized bed reactor (DHV Crystalactor) used in a commercialized crystallization removal process for orthophosphate [46].

The two main advantages of crystallization approaches include that they don't generate sludge and produce a desirable by-product; calcium phosphate pellets (40-50% P) are desirable and can be easily recycled by industry. Disadvantages of the technology include the need for continuous chemical input (i.e., for pH adjustment and seeding) and operational complexity. Although alternative P-rich compounds—hydroxyapatite and struvite, for example—can be targeted for use in crystallization systems, they are not as well developed in this context. Struvite—to be discussed in section 2.1.1.4—is considered advantageous because of its potential utility as a slow-release fertilizer; hydroxyapatite on the other hand, is only slightly soluble and is analogous to phosphate rock [18], [19], [46].

#### **2.1.1.4 Struvite precipitation**

Traditionally, struvite ( $\text{MgNH}_4\text{PO}_4 \cdot 6\text{H}_2\text{O}$ ) has been considered an unwanted by-product formed in pipes and pumps of waste-water treatment plants, creating blockages and maintenance downtime [4], [53]. Fouling by unwanted precipitation of the compound was recognized as a serious problem as early as 1939 and creates current annual costs exceeding \$100,000 for typically sized water treatment plants [18]. More recently, the concept of intentionally precipitating the mineral as a means of recovering P has received tremendous interest [19]. High purity struvite precipitation requires a Mg:N:P molar ratio of close to 1:1:1 (though excess Mg may still allow correct precipitation), pH 7.0 to 7.5 and generally long reaction times as the precipitation rate

is rather slow [19], [53]; Hao *et al.* required three months of controlled conditions at room temperature to acquire a single crystal of struvite with 99.7% purity [54]. The compounds precipitated both in practice and discussed in the scientific literature—which are typically obtained at alkaline pH with much faster kinetics—are often misreported as struvite; at pH values above 9.5, the material may well contain less than 30% struvite. It's likely that these “struvite-like” materials precipitated actually contain significant proportions of amorphous calcium and other phosphates that are XRD-silent [19].

Nevertheless, struvite-like materials are considered advantageous for P recovery and fertilizer recycling for several reasons. Firstly, the material is potentially useful as a slow-release source of nutrients, with a fertilizer efficiency somewhere between monocalcium phosphate to triple superphosphate [4], [19], [20]. Secondly, if we ignore the complication of misidentification of species, the material is rich in N as well as P, thereby providing two essential macronutrients compared to inorganic fertilizers providing P only (in addition to also recovering some N from waste streams). Finally, recovery of struvite-like materials alleviates some of the technical and economic costs of fouling in waste-water treatment plants. In fact, struvite-like material recovery is already used in some limited examples of practical application, with 80 to 90% P recovery at full-scale operation [53].

On the other hand, critics have pointed out several shortcomings of the material. Perhaps the greatest criticism is that the production of struvite material as a replacement fertilizer doesn't pass key economic tests. The chemical reagent input costs are three times the income stream typically derived from selling the recovered struvite; this is a reflection of the poor sale price, rather than high reagent costs [18]. The low sale price is a function of the material's nil advantage over fertilizers derived from mined phosphate rock, and general unattractiveness as a raw input (i.e., as a replacement for mined rock) due to its higher price and potential incompatibility with established chemical and thermal processing routes [2], [18], [19]. On top of this, struvite does not provide the optimal N:P ratio for most plant growth, so it does not eliminate the need for other inorganic fertilizers to achieve the desired balance. Finally, the fundamental misunderstanding of the obtained material's composition already discussed—and the technical challenges to actually produce true struvite from non-synthetic streams—implies that the material generally reported as struvite may not be a marketable product of known composition; variations in P or N content could have negative implications for its use as a fertilizer or as a raw input to another process.

Some have argued that there is a bias in favor of the struvite precipitation approach in the field of phosphate recovery research that can't be justified based on its limitations [19]. It is possible this is due to the origins of struvite recovery as a tool for combatting fouling problems, rather than as an approach to P recovery [18]. There may be a strong

incentive to adapt a familiar technique with demonstrated technical capability to solve a second problem, but without accounting for some of the fundamentally different objectives and requirements of a circular P recovery system.

### **2.1.2 Sorption removal**

The concept of using sorption—the term is used here to include both surface adsorption mechanisms and trapping of phosphate within the materials themselves—has received significant interest for several decades as a potential alternative to traditional dissolved inorganic P removal technologies used in waste-water treatment. Removal by sorption is seen by the research community an attractive alternative due to simplicity of design, relatively uncomplicated nature from an operations standpoint, potential for effective removal at very low P concentrations, lack of high-volume sludge production, possibility of sorbent reusability, general chemical stability and environmental compatibility [21], [55]. Ultimately, the goal is to create or identify a material that meets the as many of the following non-ordered criteria as possible: high adsorption capacities with favorable isotherm for the target phosphate concentration range, selective for phosphate, fast sorption kinetics, complete desorption (i.e. reversible sorption) and regeneration under mild stripping conditions, long cycle life, resistant to fouling by biological activity, chemical and physical stability across a wide range of pH and environmental temperature conditions, naturally abundant or easy to synthesize with low cost to mine or produce, easy to incorporate or retrofit into a full-scale

treatment system, non-hazardous and generally compatible with aquatic ecosystems in the event of accidental release. Of course, rarely does a perfect material exist for engineering applications and hence a trade-off must be accepted. The projected capital and operating costs will generally dictate the viability of a system once a baseline technical and fundamental material performance is achievable.

### **2.1.2.1 Mechanisms of sorption**

The sorption properties (e.g., capacity, kinetics) of materials are a function of the specific mechanisms by which orthophosphate is taken up. In fundamental studies, attempting to understand the underlying mechanism is generally considered the best approach to gain valuable information on how to improve and troubleshoot performance. Here, phosphate adsorption mechanisms are broken down into five classes for a brief review: outer-sphere adsorption, inner-sphere adsorption, hydrogen bonding, surface precipitation and intra-sorbent diffusion.

#### **2.1.2.1.1 Outer-sphere adsorption**

Outer-sphere adsorption is driven by purely electrostatic interactions between the sorbent surface and oppositely charged ions available in solution. To maintain an overall neutral charge, there is both adsorption of ions adjacent to the surface—this is typically accompanied by the desorption of another ion (i.e., ion exchange)—as well as an accumulation of counter ions in the diffuse layer. In this mechanism, ions adsorbed

to the surface completely retain their hydration spheres and the adsorption is physical and reversible. In other words, the ions themselves do not come into direct (i.e., chemical) contact with the surface of the sorbent material, as shown in the descriptive illustration shown in Figure 2.5. Outer-sphere adsorption is typically associated with poor selectivity, weak adsorption strength, very fast kinetics, reversibility, favoring higher concentrations and benefitting from high valency (e.g., orthophosphate at moderate to alkaline pH) [21].



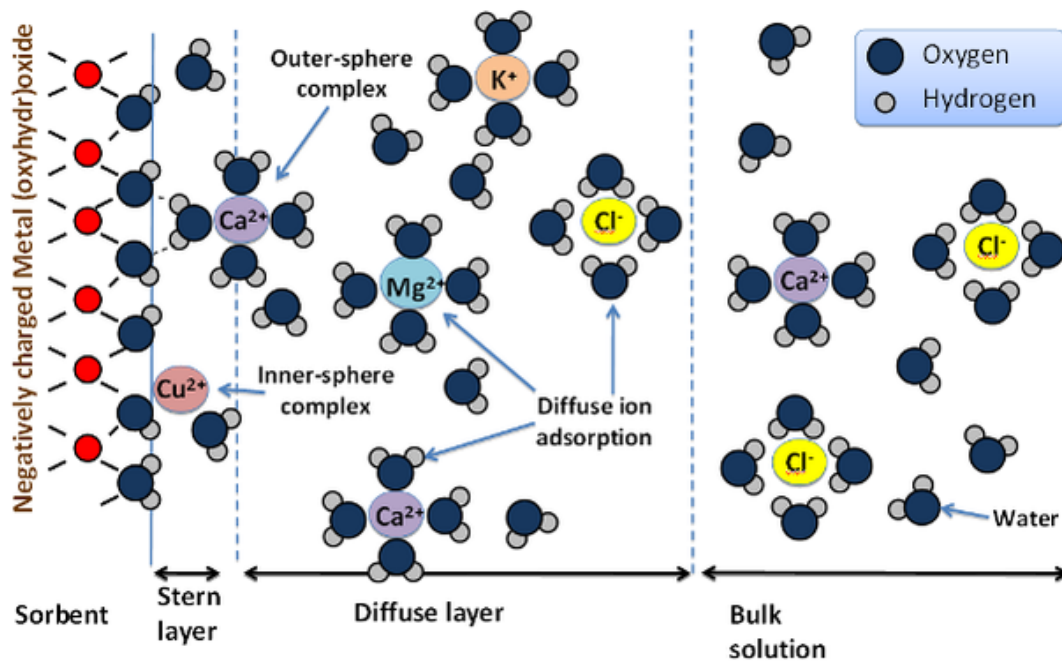


**Figure 2.5** Example illustration of outer-sphere and inner-sphere adsorption mechanisms, along with the formation of the diffuse layer that balances the surface charge of the negatively charged sorbent. From Thompson *et al.* [56].

### 2.1.2.1.2 Inner-sphere adsorption

In contrast to outer-sphere adsorption, inner-sphere adsorption is characterized by the counter ion shedding at least one coordinated  $\text{H}_2\text{O}$  molecule and forming a bond of covalent nature with the exposed surface species, as illustrated in Figure 2.5. In the context of P adsorption, the orthophosphate anion typically bonds to a metal center, and  $\text{OH}^-$ —or another adsorbed anion—is released. Because of direct chemical contact between the adsorbate and the surface, this mechanism is also described as ligand exchange in the literature. In contrast to inner-sphere adsorption—where the non-specific adsorption balances the surface charge—outer-sphere phosphate adsorption modifies the surface and tends to add negative charge owing to its trivalent nature [57]. In addition, sorbents that operate by ligand exchange can result in multiple configurations for binding of the phosphate, including mononuclear monodentate, mononuclear bidentate, binuclear bidentate, and other arrangements involving simultaneous hydrogen bonding, as shown in Figure 2.6 [21].

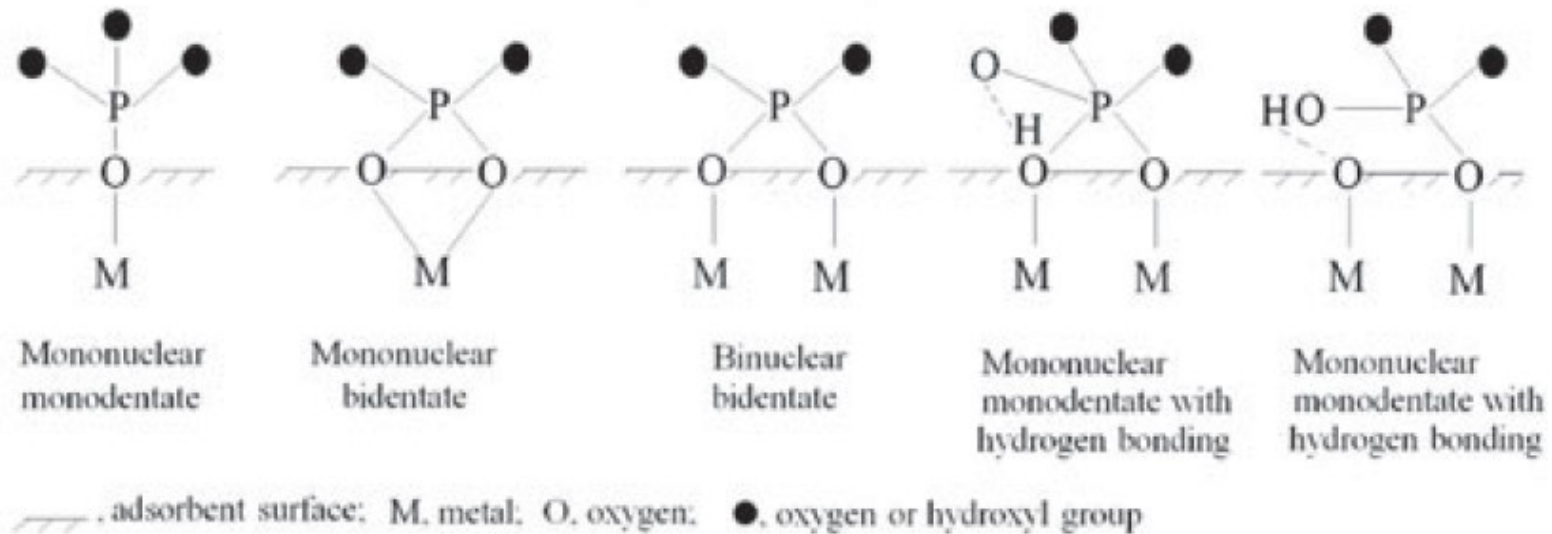
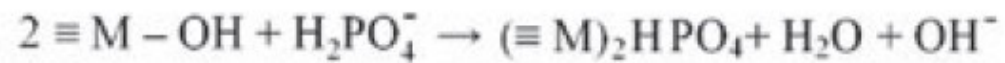


**Figure 2.6** Examples of inner-sphere phosphate adsorption on metal centers. From Loganathan *et al.* [21].

## LITERATURE REVIEW

Owing to the specific adsorption associated with inner-sphere adsorption, orthophosphate can be removed selectively, from dilute solutions and also in the presence of other anions less strongly less preferred by the active site; because it is not governed purely by electrostatic interactions, inner-sphere adsorption is also typically associated with high adsorption capacities [21]. Bolan *et al.* have previously compared and summarized the differences between specific and non-specific anion adsorption processes (i.e., inner-sphere and outer-sphere adsorption, respectively), which are detailed in Table 2.1.

**Table 2.1** Summary of the differences between outer- and inner-sphere adsorption mechanisms as applied to anionic species. Adapted from Bolan *et al.* [57]

<b>Outer-sphere adsorption</b>	<b>Inner-sphere adsorption</b>
Non-specific adsorption	Specific adsorption
Electrostatic attraction - anions and positive adsorbent sites	Chemical bonding - anions and surface sites
Balances positive charge to maintain neutrality - no new charge added to surface	Can add negative charge - number of charges generally less than anion valence
Significant adsorption only when net positive charge on sorbent	Adsorption occurs even with net negative charge on sorbent
Adsorption depends on number of positive charges on surface (anion exchange capacity)	Adsorption can exceed the anion exchange capacity
If sorbent can have variable charge, adsorption decreases with increasing pH	Adsorption can occur over wide pH range
Adsorption is weak and reversible	Adsorption is strong and less reversible

### **2.1.2.1.3 Hydrogen bonding**

Hydrogen bonding is a particularly strong attractive dipole-dipole interaction—stronger than regular interactions of this type—between an electropositive H atom bonded to a more electronegative atom on one molecule (either in the sorbate or the sorbent) and the lone electron pair on the strongly electronegative O (or N, F) on another molecule. The adsorption energy of H bonding is greater than that for outer-sphere adsorption but not as strong as inner-sphere ligand exchange. H bonding in the context of sorption generally has fast kinetics but may not always be reversible [21]. H bonding has been shown to facilitate phosphate adsorption by an alumina sorbent functionalized with carboxylic acid groups on the surface [58].

### **2.1.2.1.4 Surface precipitation**

Because orthophosphate sorption is routinely calculated from the drop in P concentration in the liquid phase, the calculated capacities can sometimes include precipitation phenomena. Specifically, this can include precipitation in the bulk liquid—provided the component concentrations exceed the equilibrium solubility product—as well as precipitation on the surface of the sorbent. Unfortunately, it's been well demonstrated that some adsorption isotherm modeling can't distinguish between true adsorption (i.e., 2D product formation) and precipitation (i.e., 3D product formation) and microscopic analysis or modeling is required for this [59]. In addition,

surface precipitation can occur at concentrations well below that predicted by bulk thermodynamics; in other words, surface precipitation can occur even when the product of the bulk concentrations of the constituents is below the  $K_{sp}$  [60]. It's thought that this is possible due to local saturation in a small region adjacent to a mineral's surface; X-ray diffraction (XRD), X-ray absorption (XAS) and scanning electron microscopy (SEM) are techniques often used to provide evidence of surface precipitation [21]. Nagamine *et al.* examined the crystallization of hydroxyapatite inside fibrous, macro-porous  $TiO_2$  using synthetic waste-water containing phosphate, bicarbonate and calcium salts [61]. They suggested that phosphate anions adsorbed to the  $TiO_2$  surface acted as nucleation sites for crystal growth of hydroxyapatite flakes, which is consistent with a surface precipitation phenomenon. Surface precipitation is generally characterized as having fast kinetics but with limited reversibility [21].

#### **2.1.2.1.5 Intra-sorbent diffusion**

For sorbents that feature a porous structure, diffusion of species inside the material can play a significant role in governing the measured sorption properties. Weber *et al.* first proposed four steps related to the sorption process in a porous material: bulk transport (fast), film diffusion (slow), intra-particle diffusion (slow), adsorption (fast) [62]. The four stages are illustrated in Figure 2.7.

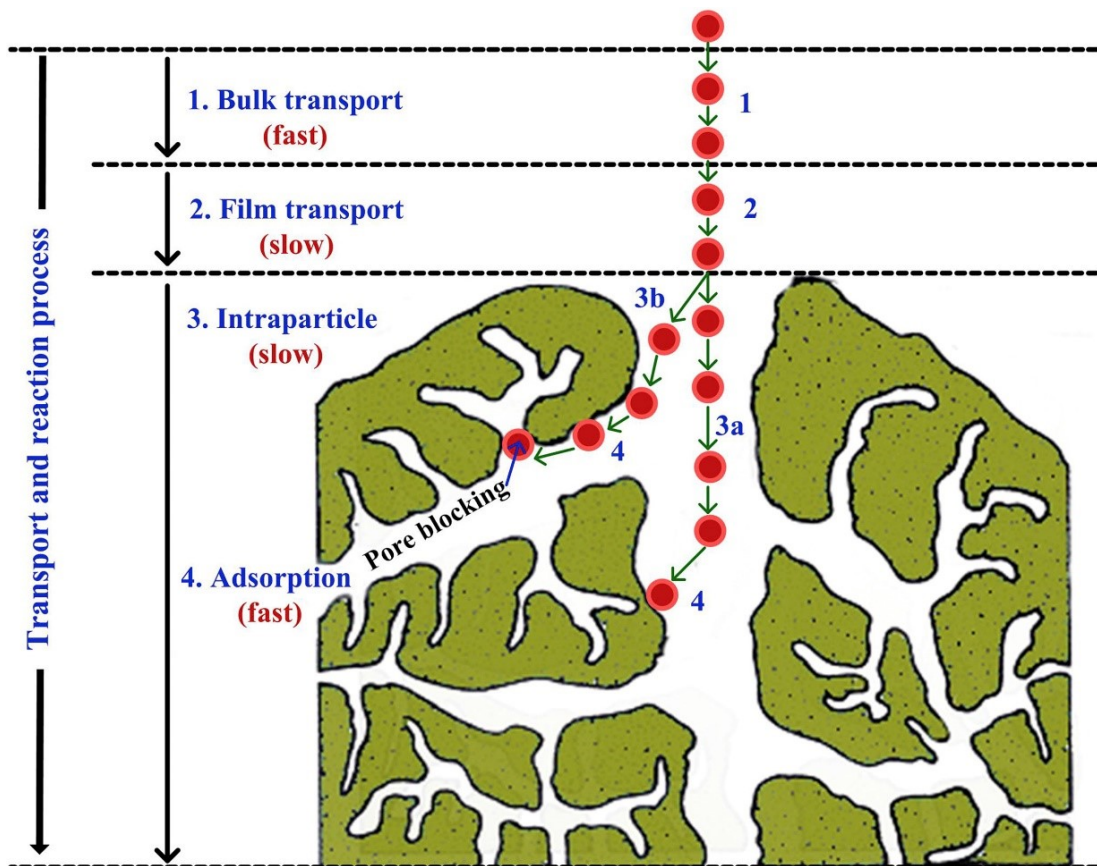


**Figure 2.7** The four reaction and transport processes important in sorption by porous materials. From Tran *et al.* [63], originally adapted from [62].



Bulk transport and final attachment to the adsorption site are typically much faster than film diffusion—where species move from the bulk aqueous phase to the sorbent’s external surface through the hydrodynamic boundary layer—and intra-particle diffusion, which involves the transport of species into and through the material’s pores or along the walls of the pores. Therefore, sorption by this mechanism is typically a multi-step process; the first being a relatively quick film-diffusion/adsorption step where the species makes its way and is adsorbed to the outer surface, followed by a significantly slower intra-particle diffusion/adsorption step as they make their way inside the particles and attach to the interior surface. The relative strength or importance of the initial film diffusion/adsorption compared to subsequent intra-particle diffusion has been modeled by Wu *et al.* by an initial adsorption factor,  $R_i$  [64]; this is an extension of Weber *et al.*’s originally proposed kinetic model of intra-particle diffusion model [65]. Sorption of phosphate by porous materials—amorphous hydrous metal oxides and date palm fibers, for example—have been shown to be consistent with the mechanism of intra-particle sorption [21]. Sorption that is heavily dominated by intra-particle diffusion is generally considered to be irreversible, especially from a practical standpoint [21].

### **2.1.2.2 Sorption materials**

A huge number of sorbents have been investigated for their orthophosphate adsorption properties. Therefore, a thorough review of every class of material is beyond the scope

of this dissertation. Instead, emphasis will be placed on inorganic materials such as zeolites, metal (hydr)oxides and layered double-hydroxides.

### 2.1.2.2.1 Inorganic materials

#### *Metal (hydr)oxides*

Metal oxides, hydroxides and oxide-hydroxides are advantageous for inorganic dissolved P removal due to their natural abundance, chemical stability, ease of synthesis, environmental compatibility and cost [55]. In particular, iron, aluminum, manganese, titanium and zirconium have been widely investigated [21].

Chitrakar *et al.* studied the phosphate adsorption properties of synthetic goethite ( $\alpha$ -FeOOH) and akaganeite ( $\beta$ -FeOOH) using synthetic phosphate solutions and phosphate-enriched seawater [28]. They showed that both materials are selective for phosphate and displayed maximum uptakes of 11 mg-P/g and 9 mg-P/g, respectively, at an equilibrium concentration of 0.3 mg-P/L in seawater and pH  $\sim$ 7. In a phosphate-only solution (50 mg-P/L), goethite and akaganeite had maximum adsorption capacities of 24 mg-P/g and 28 mg-P/g, respectively, at pH 2. They determined that the Freundlich isotherm provided a good fit for both materials, but that akaganeite had a superior selectivity, with goethite adsorbing  $\text{CO}_3^{2-}$  in addition to orthophosphate. Due to selective adsorption, the mechanism proposed was one of ligand exchange with the

surface OH groups; in other words, inner-sphere complexation. Using 0.1 M NaOH as the eluant, the authors determined that goethite had poor regeneration capability; akageneite on the other hand displayed good cyclability, retaining full adsorption capacity after ten cycles.

In the last two decades, the growing interest in nanotechnology has led to researchers examining the adsorption properties of nanoscale materials. Generally speaking, decreasing the size of a materials particles should improve adsorption performance per gram, due to the increase in specific surface area. However, creating finely powdered materials could decrease practical usability in engineering applications because of more difficult solid-liquid separation [21]. One recent example is from Afridi *et al.*, who synthesized anodized iron oxide nanoflakes and studied the effect of concentration, competing anions, heavy metals and organic matter on orthophosphate adsorption from waste-water [66]. Although the authors present scanning electron microscopy (SEM) micrographs, the paper's focus is on adsorption properties rather than size/shape control of the nanoflakes; no specific size range is mentioned or analyzed, though the flakes are submicron. The material—a mixture of magnetite ( $\text{Fe}_3\text{O}_4$ ) and hematite ( $\text{Fe}_2\text{O}_3$ ) indicated by X-ray diffraction (XRD) patterns—exhibited an adsorption capacity of 21.5 mg-P/g, but suffered significant (though not prohibitive) interference from divalent ions (e.g., carbonate, sulfate), heavy metals (e.g., arsenic, chromium) and organic matter (citric, humic and oxalic acids). Afridi *et al.* proposed a chemisorption

(i.e., inner-sphere adsorption) mechanism based on fitting to the Langmuir and Elovich models for the adsorption isotherm and kinetic behavior, respectively. Although such inferences are common in the literature, Tran *et al.* suggest that careful thought must be given in drawing conclusions on mechanism based solely on isotherm and kinetic models; other analysis techniques are usually prudent [63].

Utilizing magnetic materials is a frequently proposed solution when considering the problem of solid-liquid separation. Owing to the favorable magnetic properties of some iron oxides, they have been studied for phosphate adsorption in this context. Daou *et al.*, for example, studied the phosphate adsorption properties of magnetite-based nanoparticles [30]. The authors synthesized 40 nm magnetite particles capable of achieving a maximum adsorption capacity of 5.2 mg-P/g, measured at pH 3 and for all equilibrium concentrations higher than 300 mg-P/L. They showed that adsorption occurs rapidly, inhibits dissolution of the magnetite and doesn't impact the material structure or magnetization. Using a suite of spectroscopic techniques—infra red (IR), X-ray photoelectron (XPS) and Mössbauer—Daou *et al.* showed the mechanism involves interaction with positively charged groups as well as OH sites, specifically  $\text{Fe}^{3+}$  in octahedral sites, leading to primarily a protonated binuclear species. They found that desorption could be achieved with 1 M NaOH eluant, resulting in 90% removal and the capability for regeneration; ~75% of the initial capacity was retained after cycle stabilization. The authors did not examine the separability of the magnetite particles

from liquid using an applied magnetic field; rather the paper focused on detailed characterization of the adsorbed phosphate species on the sorbent surface.

### ***Layered double-hydroxides***

Layered double-hydroxides (LDH)—also referred to as hydrotalcite-like compounds (HTlc)—are a class of clay mineral investigated in recent decades for their phosphate and other oxyanion adsorption properties. Structurally, they are made up of brucite-like sheets—brucite has the formula  $\text{Mg}(\text{OH})_2$ —where some of the  $\text{Mg}^{2+}$  is isomorphous replaced by 3+ or 4+ charged cations, leading to positively charged sheets. This charge is balanced by intercalated anions, giving rise to a high anion exchange capacity; Figure 2.8 illustrates the general structure of LDHs. Although LDHs are found in nature, one aspect of their attractiveness is relative ease in synthesis [21], [67]. Techniques to achieve the desired composition—both in the layers themselves and the desired intercalating anion—include co-precipitation (a mixture of precursor salts with  $\text{M}^{2+}$  and  $\text{M}^{3+}$  are used), separate nucleation and aging, urea hydrolysis, ion exchange, hydrothermal methods, rehydration-reconstruction (high temperature calcination to form active metal oxides that return to the original structure after rehydrating and take up of anions; this is often termed the “memory effect”), and various others [67]. The high-temperature calcination technique can be advantageous because leads to improved sorption capacity by increasing the specific surface area and also making use of the memory effect to reform the LDH [21].

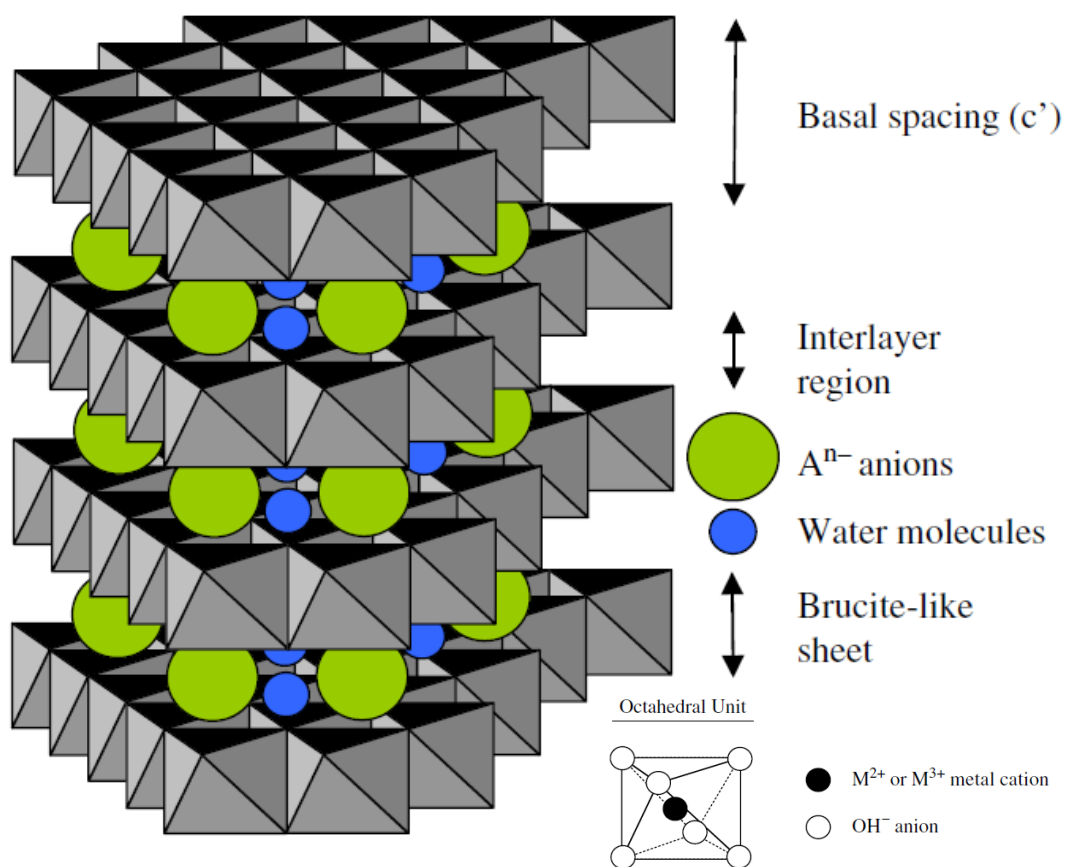


**Figure 2.8** Schematic diagram of the structure of layered double-hydroxides. From Goh *et al.* [67].

Owing to their structure, LDHs have been an increasing focus for researchers targeting the development of sorption materials for inorganic dissolved phosphate. Recently, Luengo *et al.* studied the phosphate adsorption on Mg-Al LDH prepared by a simple co-precipitation method [68]. They reported an impressive phosphate adsorption capacity of 69.7 mg-P/g at a pH of 5, though the study was unable to pinpoint a single adsorption mechanism. Instead, their interpretation from XRD and electrophoretic mobility data is that both inner-sphere adsorption and anion exchange of intercalated ions likely contribute. Interestingly, the authors reveal the extent to which LDHs dissolve as a function of pH, which is an important consideration for both applicability as stable, long-term reusable sorbent. They show that at pH 3, sorbent loading of 0.3 g/L and 0.1 M NaCl concentration, the LDS completely dissolves after 150 to 200 minutes. At pH 5, still 22% of the sorbent is lost to dissolution. Dissolved  $Mg^{2+}$  or  $Al^{3+}$  may play a significant role in phosphate removal and contribute to the apparent adsorption capacity, though it's difficult to delineate the contribution by analyzing the results in Lueng *et al.* The study also discusses protonation of orthophosphate in relation to the anion exchange capacity. At pH 5, orthophosphate is almost entirely monovalent ( $H_2PO_4^-$ ), and the reported adsorption capacity corresponds to approximately 50% of intercalated chloride ions being exchanged; only if present in the divalent form would the adsorption capacity correspond to approximately 100% ion exchange. The authors do not comment on whether this is a coincidence or indicative of a particular mechanism. LDHs typically feature high adsorption capacities, and the

results from Lueng *et al.* are in line with several other studies that investigated Mg-Al LDHs [67].

### ***Zeolites***

Compared to metal (hydr)oxides and LDHs, zeolites have received comparatively less attention for application to phosphate removal. This is despite the material's inherent advantages that have made it widely studied in other fields of application, such as heterogenous catalysis. However, in recent decades, researchers have begun to examine the contaminant removal potential of zeolites in more detail.

In 2007, Onyango *et al.* published a study examining the phosphate adsorption capability of a synthetic zeolite (HSZ 330 HUD Zeolite, Tosoh Chemical, Japan) with Si/Al ratio between 2.75 to 3.25 [27]. They studied both the H and the Al-exchanged form of the material and reported adsorption capacities ~35-50 mg-P/g at an initial orthophosphate concentration of 100 mg-P/L and neutral pH. The Al-exchanged zeolite consistently outperformed the protonated form; the authors suggested that this was due to a higher number of terminal =Al-OH sites introduced through the exchange process. According to their pH study, Onyango *et al.* reported a decrease in adsorption capacity with increasing pH, primarily due to higher coulombic repulsion of orthophosphate by increasing proportion of negatively charged binding sites at elevated pH (i.e., =Al-OH). The study suggests a combination of outer- and inner-sphere adsorption, with the latter



(ligand-exchange) dominating at higher pH, where outer-sphere electrostatics are unfavorable. They report a better fit to the Freundlich isotherm, attempt to explain kinetic behavior using a variation of the intra-particle diffusion model, and show that approximately half of the adsorbed phosphate can be released at high pH using sodium hydroxide as the eluant. Onyango *et al.*'s study is one of the earlier publications in this field to describe using a metal-exchanged zeolite for the adsorption of phosphate. However, the selected synthetic zeolite is not of a well-known framework and the material is unavailable for purchase in 2020.

More recently, there is an increasing trend towards lanthanum modification of zeolites [69]–[73]. Generally, the rare earth element is considered favorable due to its environmental compatibility, redox stability and strong affinity for orthophosphate;  $\text{LaPO}_4$  is least soluble of the rare-earth phosphate compounds [71].

In 2019, Shi *et al.* reported enhanced removal of orthophosphate from aqueous systems using zeolite loaded with Mg-Al-La ternary hydr(oxides) [69]. They demonstrated a maximum adsorption capacity of 80.8 mg-P/g at pH 6.6, stability in adsorption between pH 4 and 10, and selectivity towards phosphate in the presence of sulfate and nitrate coexisting in solution. However, the authors reported the maximum adsorption capacity as that deduced from adsorption isotherm modeling, which means this capacity would never be achieved in application to unconcentrated environmental or waste-water

streams—where concentrations are typically low—alluded to in their motivations. In contrast, their study on sewage-contaminated water from a local river showed adsorption was  $<10$  mg-P/g.

In the same year, Pham *et al.* studied phosphate adsorption and recovery using La-modified ZSM-5 beads [70]. The authors synthesized the material by impregnating commercial ZSM-5 beads with lanthanum nitrate solution. They justified the choice of beads by stating concerns regarding leaching of the powdered zeolite materials and perceived difficulty in their recovery and reuse. The reported maximum adsorption capacity (using the Langmuir isotherm) was 106.2 mg-P/g, compared to 59.8 mg-P/g for the zeolite beads without lanthanum modification. Pham *et al.* suggest a ligand-exchange mechanism is responsible for enhanced adsorption with lanthanum-modified beads, with variations in pH explainable due to changes in the surface charge and speciation of phosphate.

With respect to copper-exchanged zeolites, Manto *et al.* conducted a study in 2017 on the potential utility of Cu-ZSM-5 as a sorbent for recovery of inorganic dissolved phosphorus [74]. Here, the zeolite material was prepared from commercial  $\text{NH}_4$ -ZSM-5 treated with intermediate steps (H-ZSM-5, then Na-ZSM-5). The study uses 1 g/L  $\text{Na}_2\text{HPO}_4$  with unadjusted initial pH of 8.6 and sorbent loading of 30 mg/mL. Under these conditions, the achieved capacity was  $\sim 30$  mg-P/g, with an increase in capacity

(and speed) observed with increasing exchange level during synthesis. Manto *et al.* focus on the recovery and reuse potential of the material, for which impressive values are reported; >90% at the synthetic conditions. However, the recovery is less than 40% for a waste-water sample with 8.1 mg-P/L inorganic dissolved phosphate. The authors identify the importance of Cu(II) as the active site in specific phosphate adsorption, but several questions remain unanswered and present new directions to build on this research.

Firstly, Manto *et al.*'s study limits itself to ZSM-5 with a Si/Al ratio of 11.5; what role does the Si/Al ratio play in the adsorption of orthophosphate? Secondly, the synthetic portion of the study only considers one phosphate concentration, 1 g/L; this is generally one to two orders of magnitude greater than the concentrations expected in waste-water treatment or environmental systems without significant pre-concentration. It may be of interest to study the sorbent over a wider range of concentrations and establish the nature of the adsorption isotherm; do traditional models explain the behavior and what correlation (if any) is there with the Si/Al ratio? Thirdly, it's reasonable to ask what the role of pH is on adsorption of phosphate; Manto *et al.* focus on an alkaline pH of 8.6 without adjustment. What trends can be observed when the pH is varied? Seeking answers to these questions is one objective of this dissertation.

#### **2.1.2.2.2 Other materials**

Sorption materials are not limited to chemically synthesized or naturally occurring inorganic materials. Organic sorbents play exceedingly important roles in various adsorption processes, and some—such as activated carbon and anion exchange resins—have been investigated for their application to phosphate recovery [75]. Biological wastes are another sorbent class attracting increased attention due to demonstrated activity for phosphate adsorption and the novelty of using recycled materials to further recycle nutrients such as phosphate. Biochars and food waste (e.g., food and fruit peels) are typical examples of these materials [26], [76]. In a similar vein, industrial wastes have also been investigated, including red mud (tailings from bauxite mining processes at the front-end of aluminum production), slags (from furnace operations) and fly ash (combustion by-products) [21]. For a detailed review of phosphate sorbent materials that extends beyond those of inorganic nature, the reader is directed to the comprehensive accounting by Loganathan *et al.* [21].

### **2.2 Characterization of Cu in copper-exchanged ZSM-5**

As outlined in the introduction to this dissertation, despite the success of small pore zeolites in addressing some of the critical issues with Cu-ZSM-5 in automotive catalytic applications, the latter remains an active area of study. Specifically, the exact nature of the active metal sites in copper-exchanged ZSM-5—generally accepted to be a Cu

dimer of generalized form  $[\text{Cu}-\text{O}_x-\text{Cu}]^{2+}$  bridging framework Al T-sites and formed from copper ions introduced through ion exchange—is still not completely understood and therefore remains of interest to the academic community [41]–[45]. Given that dimer sites coexist with isolated  $\text{Cu}^{2+}$  monomers—and in some cases, crystalline CuO—there has been a drive to investigate and characterize the dimer fraction of all Cu sites in the zeolite [42]. These site types are depicted in a simplified form in Figure 2.9. This information can serve as a particularly useful tool in correlating and better understanding the catalytic active sites in Cu-ZSM-5. Here, with a focus on methods that do not require reactive conditions, a selection of investigative tools used to study the nature of Cu sites will be reviewed.

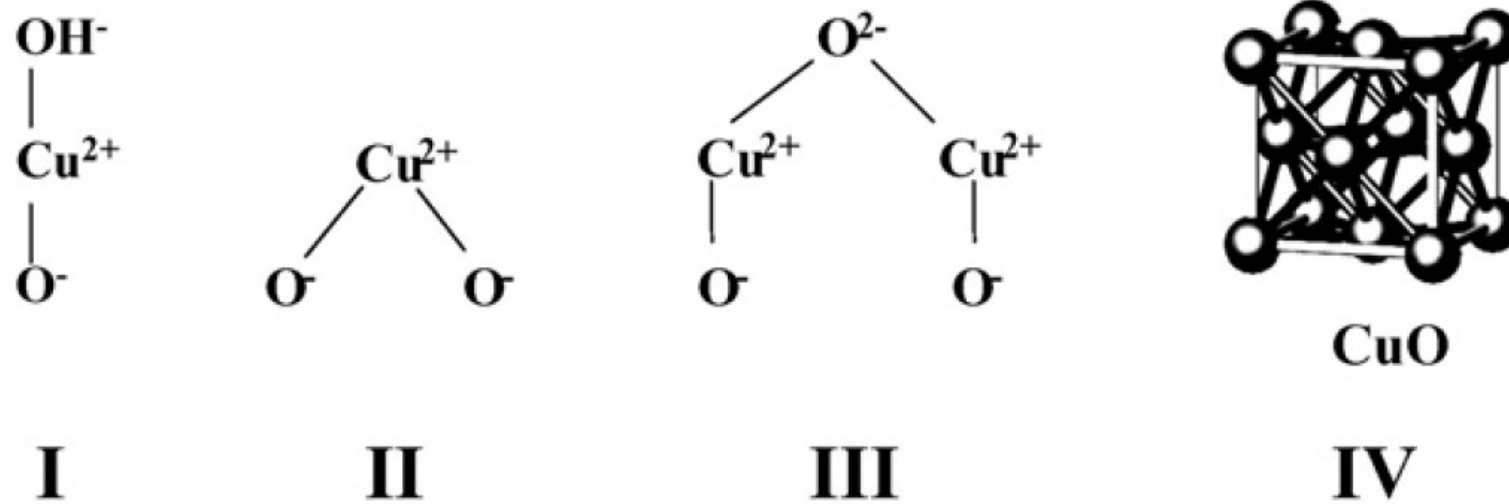


**Figure 2.9** Simplified representation of potential copper species in Cu-ZSM-5. I and II represent monomeric Cu sites, while III is indicative of the dimer. IV represents crystalline or bulk copper oxide formed within the zeolite. From Da Costa *et al.* [42].

## 2.2.1 Analytical techniques

A host of analytical techniques have been applied to characterizing active sites in Cu-ZSM-5, whether focused on the Cu sites directly, by characterizing adsorbates relevant to the reactions of interest, or other probe molecules used under non-reactive and typically low-temperature conditions.

### 2.2.1.1 Spectroscopy

X-Ray based methods have been widely used, and are attractive due to their relative simplicity, ability to penetrate various conditions and amenability to characterization of materials pre-, during and post-reaction [36]. X-ray absorption spectroscopy (XAS) is unique in its ability to provide information on structural and electronic properties of catalysts under such conditions; XAS is one of very few methods that exclusively relies on photons [77]. Da Costa *et al.* used x-ray absorption near edge structure (XANES) analysis to support their study of dimeric and monomeric Cu sites in Cu-ZSM-5 [42]; spectral features in the near-edge portion are sensitive to the oxidation state of copper [42], [43]. Examining the near-edge spectra during treatment with H<sub>2</sub> (and others), the Da Costa *et al.* were able to track—using two distinct spectral features—the oxidation state changes from Cu(II), Cu(I) and Cu(0) for samples with different Cu/Al ratios (i.e., exchange levels) and exposed to different temperature and chemical conditions. Although this spectroscopic technique was useful to study the redox chemistry of

copper in Cu-ZSM-5, it was not directly applied to quantification of dimeric vs. monomeric sites in the zeolite. Similarly, extended x-ray absorption fine structure (EXAFS) can reveal detailed, localized chemical information of interest to the study of Cu-ZSM-5. However, the technique is complicated—relying heavily on non-trivial data fitting and processing algorithms—and can lead to varying and sometimes conflicting conclusions when applied to the study of dimeric copper sites [43], [78]. Groothaert *et al.* concluded—based on a study utilizing EXAFS and supported by UV-vis-near-IR—that copper dimer species, bis( $\mu$ -oxo)dicopper, is formed at Cu/Al greater than 0.2 leading to a sharp increase in NO decomposition activity [43]. However, similar to many studies based solely on spectroscopic techniques, quantification of dimeric vs. monomeric sites in Cu-ZSM-5 is not achieved with this approach; rather the focus is on detection and characterization of the sites themselves.

Other spectral techniques have been used in studying copper-exchanged zeolites, including x-ray diffraction (XRD), infrared spectroscopy (IR), UV-Vis diffuse reflectance spectroscopy (DRS), electron paramagnetic resonance (EPR) and several more [36]. While ex-situ XRD is generally used for identification of phases, in-situ is generally a weaker tool than XAS for studying dimer/monomer copper sites due to a general requirement for long-range order [77], [78]. IR is powerful analytical tool, though Cu (or Cu-adsorbate complexes) may not be redox-stable during IR data collection; in addition, under many conditions significantly less than 100% of copper



in the sample is actually observed [44]. DRS can provide insight into the Cu(II) coordination environment due to electronic transitions in the 3d shell being dependent on the ligand structure around the metal [79]. However, because this ligand coordination environment is not homogenous, spectra often overlap; low Cu exchange levels are assumed to provide better DRS results due to only preferred sites being occupied, which represents one limitation of the method. EPR has been used with some success for characterizing copper sites; generally, the EPR-active copper is identified as isolated (i.e., monomeric) Cu(II) on the zeolite framework [43], [80]. However, the signal is highly sensitive to the hydration state of the material [80]. Groothaert *et al.* used the “EPR silence” of the monomeric copper sites in order to quantify the dimeric fraction in Cu-ZSM-5 with varying Cu/Al ratios [43]. In general, it is challenging to quantify the coppers dimers and monomers directly using spectroscopic techniques alone.

### **2.2.1.2 Probe molecules and temperature programmed methods**

A well-refined and state of the art thrust in non-reactive experimental characterization and quantification of active sites in Cu-ZSM-5 is to combine a spectroscopic technique (e.g., FT-IR, IR) with a gaseous chemical probe to study and characterize adsorption sites in the zeolite. The premise of this approach is that upon adsorption, the vibrational spectrum of the probe molecule is altered in such a way that information on the active adsorption site is revealed [36]. Ammonia, for example is widely used to probe the acid

properties of solid catalysts [36]. Frequently, the molecular probe approach is combined with temperature-programmed desorption (TPD), where desorbed molecules are monitored—by a suitable detector, such as a mass spectrometer or gas chromatograph—as the temperature increases; the desorption rate vs. temperature spectrum can reveal information about the adsorption interactions with the surface, especially binding energy and site quantity [81]. Similarly, temperature-programmed reduction (TPR) with probes such as CO and H<sub>2</sub> can provide information on these active sites.

Da Costa *et al.* used H<sub>2</sub>/CO and O<sub>2</sub> as probe molecules in TPR and TPD experiments, respectively, in parallel with XAS to study the speciation of copper in Cu-ZSM-5 over a range of Cu/Al ratios from 0.12 to 0.60 [42]. Their H<sub>2</sub>-TPR experiments support their conclusions that in ion-exchanged samples subject to calcination, the principal species were isolated Cu<sup>2+</sup> (not [Cu<sup>2+</sup>OH]<sup>+</sup>) and dimers of the form [Cu<sup>2+</sup>O<sup>2-</sup>Cu<sup>2+</sup>]<sup>2+</sup>; these results were obtained by correlating H<sub>2</sub> consumption and H<sub>2</sub>O evolution quantities calculated from the TPR spectra to expected H<sub>2</sub>/Cu, H<sub>2</sub>O/Cu and H<sub>2</sub>/H<sub>2</sub>O stoichiometries for the proposed Cu species (I though IV, Figure 2.9). The authors' parallel XANES analysis supported the H<sub>2</sub>-TPR data. Similarly, they employ CO as a probe in TPR to specifically titrate the copper dimer sites, as this species features a removable oxygen unlike isolated Cu<sup>2+</sup> (owing to a lack of protons needed to balance charges). They determined the dimer percentage of the total number of copper sites

increased from 46% to 78% as Cu/Al increased from 0.12 to 0.60. Further, Da Costa *et al.* used O<sub>2</sub>-TPD to identify differences in dimer behavior as Cu/Al was varied, finding that the fraction of dimers capable of auto reducing and liberating O<sub>2</sub> increased as Cu/Al increased due to dimers being in closer proximity to each other; at these higher ratios, a larger number of unstable copper dimers form which correlate with higher NO decomposition activity. Da Costa *et al.*'s work is one example that encompasses the general approach to utilizing probe molecules to glean information about a catalyst's surface sites. It is worth noting that well-controlled experimental conditions and carefully calibrated instrumental setups are required to obtain reliable results from this methodology; it's conceivable that the complexity involved may have contributed to relatively frequent contradictory findings within this area of study [36], [42], [43].

### **2.2.1.3 Liquid phase probes**

The usage of gas probe molecules is well-developed and represents the state of the art in this approach for the determination of copper site speciation and quantifying the dimeric and monomeric fractions. In contrast, the usage of liquid phase probes to investigate and quantify copper sites in Cu-ZSM-5 does not appear to have been studied. It is reasonable to assume that there has been little attention paid to this direction because the zeolite catalyst itself has primarily found utility in gas phase reactions, such as SCR and direct NO decomposition. More recently, Cu-ZSM-5 has been applied to the catalytic dehydration of glucose into 5-hydroxymethylfurfural in a

multi-phased liquid system [82]. Additionally, the material has, as previously discussed, been studied for its phosphate adsorption properties in aqueous systems [74]. For the most part though, liquid phase applications of Cu-ZSM-5 have not been widely studied. Therefore, the possibility of using liquid phase molecular probes for studying the nature of copper sites in Cu-ZSM-5 is of potential value to the research efforts in this field and may lead to new methodologies that could be applicable to other heterogenous catalysts.

## **Chapter 3 Methodology**

### **3.1 Introduction**

The purpose of the methodology section is to explain how the results of this research work were obtained, as well as discuss and justify the use of certain methods. Consistent with the concept of maintaining high standards of ‘pre-productibility’—defined and discussed by Stark [83]—in the dissemination of research, the descriptions here will provide sufficient detail such that readers may fully understand how the experimental work was completed and the methods used to process or analyze data. The guiding principle is that the reader will be given enough information to check and repeat the work with confidence.

### **3.2 Considerations in the determination of phosphate adsorption**

#### **3.2.1 Batch vs. continuous flow**

It is likely that any practical recovery system designed to capture P from diffuse or point sources in the environment or waste-water treatment plants would be continuous in nature. A batch system would be untenable in the context of well-established

continuous flows (e.g., municipal waste-water, agricultural run-off). However, in the context of studying fundamental adsorption properties of materials, batch tests are appropriate; they facilitate the measurement of both fundamental equilibrium data (e.g., adsorption isotherms) and kinetic data (e.g., rate constants, determination of reaction order) with simple experimental setups that are largely free from the confounding effects of transport and reactor design. Batch testing is widely used in the field for measuring the phosphate adsorption abilities of materials [21], [55]. While acknowledging the limitations—primarily, that batch results are not directly translatable to a real-world, continuous systems—batch studies were selected for this work because of the focus on fundamental studies and ease of comparison to the large body of existing results based upon this method.

### **3.2.2 Quantification of the adsorbate**

Equilibrium and kinetic studies on adsorption require an acceptably accurate, precise and fast method for quantifying the amount of adsorbate taken up by a material. Conceptually, the most direct approach would be to measure the adsorbate's mass or other signal while it remains on the material. Unfortunately, this method may be difficult to employ in practice; in aqueous systems, the solid-liquid separation would have to be complete, measuring mass alone is not specific for a particular adsorbate, and techniques for translating other signals (e.g., energy-dispersive x-ray spectroscopy) may not satisfy requirements for accuracy and precision. Typically, batch adsorption

experiments instead rely on measuring the initial concentration of the adsorbate of interest in a solution sample—well-established assay techniques exist for many species, including phosphate—and comparing this to the (lower) concentration after exposure to the adsorbent. With knowledge of the solution volume and other parameters, the change in concentration can be used to quantify adsorption by the adsorbent under the assumption that no other process can consume the species in question. Owing to its simplicity and the availability of well-established and robust chemical assays, this technique is close to a *de facto* standard for studies measuring inorganic phosphate adsorption—or phosphate removal by other means—and has therefore been adopted in this work [21], [27]–[29], [76], [84].

### **3.2.2.1 Phosphate determination in aqueous systems**

A robust method for determining P is critical to the success of obtaining reliable data on the adsorption by a given material. Owing to its importance in the environment and long-established regulations on monitoring, techniques for determining P are well-established [85]. Figure 3.1 summarizes commonly delineated forms of P that may be of interest in a variety of systems. In the context of phosphate adsorption studies—where P is typically provided in the form of synthetic salt solutions of sodium or potassium phosphate—dissolved reactive phosphorus (DRP) generally accounts for all

P and is therefore the quantity of interest; it is synonymous in this dissertation with orthophosphate, dissolved inorganic P and  $H_xPO_4^{(3-x)-}$ .

The most widely used technique for P analysis is based on spectrophotometric detection using the reaction with molybdate to create a blue-colored complex, first described by Murphey & Riley in 1962 [85]–[87]. This ‘molybdenum blue’ spectrophotometric technique—which measures orthophosphate—can be used in conjunction with relevant filtration, persulfate digestion, sulfuric acid hydrolysis and mass balances to determine the P quantity of interest, as shown in Figure 3.1 [88]. The method is approved by the United States Environmental Protection Agency [88]. A detailed review of the underlying chemistry of the molybdenum blue method reaction beyond the scope of this dissertation; the reader is directed instead to discussions in Nagul *et al.* [85], which contains a thorough review of the reaction chemistry and interferences, along with various criteria for improvements and adjustments to the original method useful for optimizing the technique to specific applications (the specific implementation devised for use in this work is discussed in section 3.3.4).



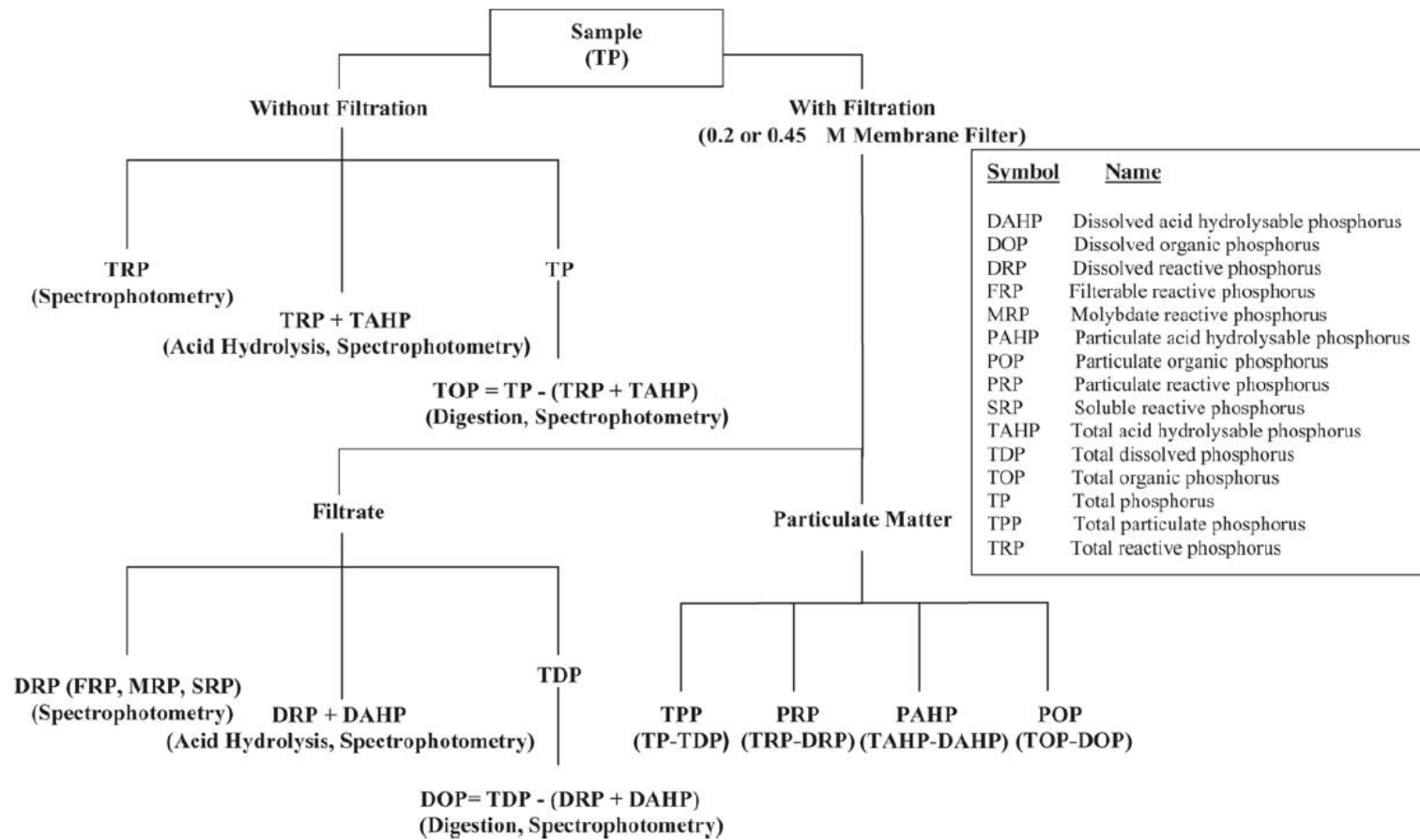


**Figure 3.1** Breakdown of various forms of P in aquatic system. From Worsfold *et al.* [86] originally adapted from [89].

Briefly, the chemistry of the molybdenum blue reaction can be described as follows. First, orthophosphate—strictly speaking, any molybdate-reactive phosphate can react, including labile phosphate groups in some organic molecules [90]—combines with Mo(VI) (generally supplied from a molybdate salt) in a strongly acidified aqueous solution—pH between 0 and 1 typically achieved with sulfuric acid—to form the Keggin ion, 12-molybdophosphoric acid (12-MPA). 12-MPA is then reduced to a phospho-molybdenum complex by addition of suitable reductant(s), typically a combination of ascorbic acid with Sn(II) or Sb(III). Although the exact phospho-molybdenum complex produced varies depending on the reductants, pH, heating and other conditions, they generally exhibit a blue color with one or two strong absorption peaks in the 600 to 900 nm range of the visible spectrum [85].

The P assay method developed for use in this work is based on Harwood *et al.* [90], with some adjustments based on Nagul *et al.* and laboratory experimentation. This method was chosen for its low limit of quantification (estimated at 0.05 mg-P/L), acceptable working range (linear up to ~2.5 mg-P/L), temporal stability of the phospho-molybdenum species (afforded by addition of Sb(III); enhances repeatability), similarity to commercially-produced test kits (e.g., Hach Company TNTplus® 843, Loveland, CO) and chemical compatibility (i.e., no anticipated interferences).

### 3.3 Materials and methods

Ultra-pure deionized water (18.2 M $\Omega$ ·cm) was used in all experimental work and delivered from an ELGA PURELAB flex system. All chemicals were used as received unless noted otherwise.

#### 3.3.1 Synthesis of copper-exchanged ZSM-5

Cu-ZSM-5 sorbents with nominal Si/Al ratios of 11.5, 15, 40 and 100 – 200 were synthesized based on a typical wet ion exchange method beginning with commercially available ammonium ZSM-5 (Alfa Aesar 45879, 45880, 45882, 45883) with intermediate steps to produce H-ZSM-5 and Na-ZSM-5 [74]. Typically, published methods for this synthesis of Cu-ZSM-5 tend to omit various details that could be beneficial to others seeking to reproduce the materials with confidence. Therefore, the full procedure used in this study has been presented here. Table 3.1 summarizes the technical data of the as-received zeolites, based on the relevant certificates of analysis. The Si/Al ratios (by analysis) obtained from this data will be used to identify the four zeolite materials and their derivatives throughout this dissertation.

**Table 3.1** Technical data for as-received ammonium ZSM-5 zeolite. The Si/Al from analysis will be used in this dissertation for identification and calculation purposes.

<b>Nominal Si/Al</b>	<b>Si/Al (by analysis)</b>	<b>Surface area (m<sup>2</sup>/g)</b>	<b>Crystallinity (by XRD)</b>
<i>11.5</i>	11	439	92%
<i>15</i>	17	443	88%
<i>40</i>	42	463	94%
<i>100 – 200</i>	161	437	97%

## METHODOLOGY

First, ammonium ZSM-5 was converted to H-ZSM-5 by calcination in static air. Approximately 15 to 20 g of the  $\text{NH}_4$ -ZSM-5 powder was transferred to an open vessel and placed inside a cool box furnace programmed to ramp and then hold at 450 °C for 4 hours. The heating and cooling rate were both set to 5 °C/min.

After cooling, the product was converted to Na-ZSM-5 by ion exchange. An accurately weighed amount (typically 10 to 15 g) of the cool H-ZSM-5 was combined with  $10.0 \pm 0.1$  mL/ $\text{g}_{\text{zeolite}}$  of  $1.00 \pm 0.05$  M aqueous sodium nitrate solution (from sodium nitrate,  $\geq 99.0\%$ , Sigma-Aldrich S5506) and transferred to a 250 mL three-neck round bottom glass flask with a ~1-inch PTFE-coated stir bar. All openings were closed with glass stoppers and the flask lowered into a pre-heated oil bath (~1 L) manually controlled to  $80 \pm 5$  °C for 4 hours using a thermometer and hot plate set to stir at ~500 RPM. Upon completion, the flask was removed from the bath and the off-white mixture washed with deionized water into several conical tubes for centrifugation at 10,000 RPM for at least five minutes. After pouring off the clear and colorless supernatant, the solid was washed twice using deionized water and intermediate centrifugation. The sodium ion exchange procedure described above was repeated an additional two times. The centrifuged (but still wet) solids were not dried or reweighed between ion exchange steps; the same volume of sodium nitrate solution determined for the first ion exchange step was added to the solids in the centrifuge tubes, shaken to a mixture, and then transferred to a clean 250 mL glass flask for the next ion exchange step. After the third

ion exchange step, the product mixture was not centrifuged; the mixture was filtered using a Büchner funnel and P4 grade qualitative filter paper, and subsequently washed by addition and filtration of  $\sim 150 \text{ mL/g}_{\text{zeolite}}$  deionized water to remove residual salt. The filtered and washed Na-ZSM-5 was dried in an oven at  $\sim 70$  to  $90 \text{ }^\circ\text{C}$  for at least several hours.

Finally, the off-white Na-ZSM-5 powder was converted to Cu-ZSM-5 by ion exchange. Three ion exchange steps of  $\sim 24$  h each were performed at room temperature with  $10.0 \pm 0.5 \text{ mM}$  aqueous copper(II) acetate solution (from copper(II) acetate monohydrate,  $\geq 99.0\%$ , Sigma-Aldrich 61148). The volume of copper(II) acetate solution used in each step was calculated such that the number-ratio of copper ions in the liquid to aluminum sites in the weighed Na-ZSM-5 powder—typically three to four grams—equaled 0.5 (i.e., full exchange based on charge balance) based on a simplified molecular formula of  $\text{Na}_2\text{Al}_2\text{O}_3 \cdot 2x\text{SiO}_2$  (where  $x$  is the nominal Si/Al ratio of the commercially purchased zeolite). For example, the volumes used were therefore  $65 \text{ mL/g}_{\text{zeolite}}$  and  $20 \text{ mL/g}_{\text{zeolite}}$  for Si/Al = 11 and Si/Al = 42 zeolites, respectively. The intermediate centrifugation, washing, filtration and drying steps were the same as those described for the synthesis of Na-ZSM-5, except that the final vacuum filtration and washing was completed with  $\sim 1 \text{ L/g}_{\text{zeolite}}$  deionized water to ensure removal of any residual copper salt. After drying, the light blue powder was calcined in static air at  $500 \text{ }^\circ\text{C}$  for 4 hours. The powder was initially placed in a cool furnace and the heating rate was  $\sim 30 \text{ }^\circ\text{C}/\text{min}$ . After calcination,

the samples were cooled at ~5 to 10 °C/min, removed from the furnace at ~150 to 200 °C and transferred to a vacuum desiccator for cooling to room temperature.

### 3.3.2 Batch tests for measuring phosphate adsorption

All data was collected at  $20 \pm 2$  °C. Batch adsorption tests were performed using a zeolite loading rate of 20 mg/mL. This dosage was selected to facilitate a level of adsorption that could be determined from the difference in measured concentrations without excessive error propagation. Equation 1 shows the calculation of adsorbed phosphate, where  $q$  is the adsorbed phosphate (milligrams—in terms of elemental P—per gram of zeolite),  $C_0$  is the measured phosphate concentration of the solution before mixing with zeolite (mg-P/L),  $C$  is the measured phosphate concentration after separation of solids,  $V$  is the volume of solution added and  $m$  is the mass of zeolite used.

$$q = \frac{(C_0 - C) \times V}{m} \left[ \frac{\text{mg-P}}{\text{g}_{zeolite}} \right] \quad (\text{Equation 1})$$

For data used in the construction of adsorption isotherms, all solutions were diluted from a stock sodium phosphate buffer prepared at pH 7 (sodium phosphate monobasic,  $\geq 99.0\%$ , Sigma-Aldrich RDD007 and sodium phosphate dibasic,  $\geq 99.0\%$ , Sigma-Aldrich 795410). All solutions were verified to be within 0.3 units of pH 7. For the preparation of phosphate solutions at the same concentration but different pH,

## METHODOLOGY

phosphoric acid (o-Phosphoric Acid, 85% (Certified ACS), Fisher Chemical) was added by pipette to volumetric flasks with approximately half the capacity of water. The solutions were adjusted with 1 M NaOH, with the target volumes of base determined by initial measurements and trials. The flasks were then made up to the mark. Therefore, the pH-adjusted phosphate solutions all featured the same phosphate concentration (within measurement error), without dilution or contamination with other anions that would have occurred if solutions were adjusted after preparation by addition of volumes of concentrated acid or base.

In a typical experiment,  $10.0 \pm 0.1$  mL of the relevant aqueous sodium phosphate solution was added to  $200 \pm 1$  mg of Cu-ZSM-5 in a capped 20 mL glass vial with 0.5-inch PTFE-coated stir bar. The mixture was stirred at  $\sim 1100$  RPM for between two and 24 hours to allow equilibration, with the time used depending on the observed kinetic behavior of the sample. After this time, the solids were separated using a  $0.22 \mu\text{m}$  PES syringe filter (it was verified that the filter did not interfere with phosphate measurements) and the filtrate prepared for assay and pH measurement. For samples requiring analysis of post-adsorption solids (e.g., FT-IR, XRD), preliminary separation was achieved by centrifugation at 10,000 RPM for approximately 5 minutes. The supernatant was poured off and filtered through a  $0.22 \mu\text{m}$  membrane as described above and prepared for assay. The solids were washed of remaining adsorbate solution by vortex mixing with  $20 \pm 1$  mL deionized water and centrifuged again, the supernatant



being filtered and assayed for phosphate in order to calculate the remaining phosphate adsorbed on the solid.

### **3.3.2.1 Kinetic data**

To obtain kinetic data, a ~1 mL aliquot was taken by syringe from the well-mixed vial at each pre-determined time point and immediately filtered through a 0.22  $\mu\text{m}$  PES syringe filter. The filtrate was then prepared for assay.

### **3.3.3 pH measurement**

All pH measurements were taken at  $20 \pm 2$  °C with a Eutech Instruments pHTestr 30 probe calibrated with three buffer standards (4.0, 7.0, 10.0) prior to use.

### **3.3.4 Spectrophotometric determination of phosphate**

A customized implementation of the widely-used molybdenum blue reaction was used for phosphate determination in this study [85], [90]. The following three solutions were prepared for this assay:

1. 1.0 M  $\text{H}_2\text{SO}_4$  (prepared from concentrated sulfuric acid, TraceMetal™ Grade, Fisher Chemical; 13.3 mL in 250 mL deionized water)

## METHODOLOGY

2. 3.85 mM ammonium molybdate tetrahydrate solution (prepared from ammonium molybdate tetrahydrate, ACS reagent, 81.0-83.0% MoO<sub>3</sub> basis, Sigma-Aldrich A7302; 1.19 g in 250 mL deionized water). The solution was not kept for longer than three months. Prior to an analysis run, the aliquot removed from the bottle was filtered through a 0.22 μm PES syringe filter.
3. Mixed reagent solution: 810 mg L-ascorbic acid (≥99.0%, Sigma-Aldrich 795437), 22 ± 1 mg potassium antimonyl tartrate trihydrate (≥99.0%, Sigma-Aldrich 383376) and 40.0 ± 0.5 mL deionized water were mixed until clear. The solution was prepared fresh prior to analysis and filtered through a 0.22 μm PES syringe filter.

First, up to 2 mL of sample was transferred by micropipette into a disposable glass vial, along with deionized water to make up any balance. Then, 1 mL of the sulfuric acid solution was added by micropipette, and the vial swirled or vortexed at low speed. Prior to measurement, 1 mL of the ammonium molybdate solution was added by micropipette, followed by 1 mL of the mixed reagent solution (the total volume of the assay solution was therefore 5 mL). A 15-minute timer was started, and the vial vortexed or swirled thoroughly for at least 10 seconds. Close to the 15-minute mark, the vial was swirled again, and an aliquot transferred to a disposable methacrylate cuvette. At the 15-minute mark, the absorbance at 880 nm was read in a ThermoFisher Genesys 50 UV-Visible spectrophotometer.

## METHODOLOGY

A new calibration curve was constructed for each analysis run using five equally spaced sodium phosphate standards (including the reagent blank). Figure 3.2 and Figure 3.3 are examples of the measured absorbance spectra of the standards and calibration curve, respectively. The target range for analysis with this method was between 0.05 and 1.5 mg-P/L (this refers to the concentration in the 5 mL assay solution), the upper limit corresponding to a maximum absorbance of ~1.0. However, the method was observed to be linear to at least 2.5 mg-P/L. Salt spike studies were performed with NaCl (99%+ ACS, Fisher Chemical).

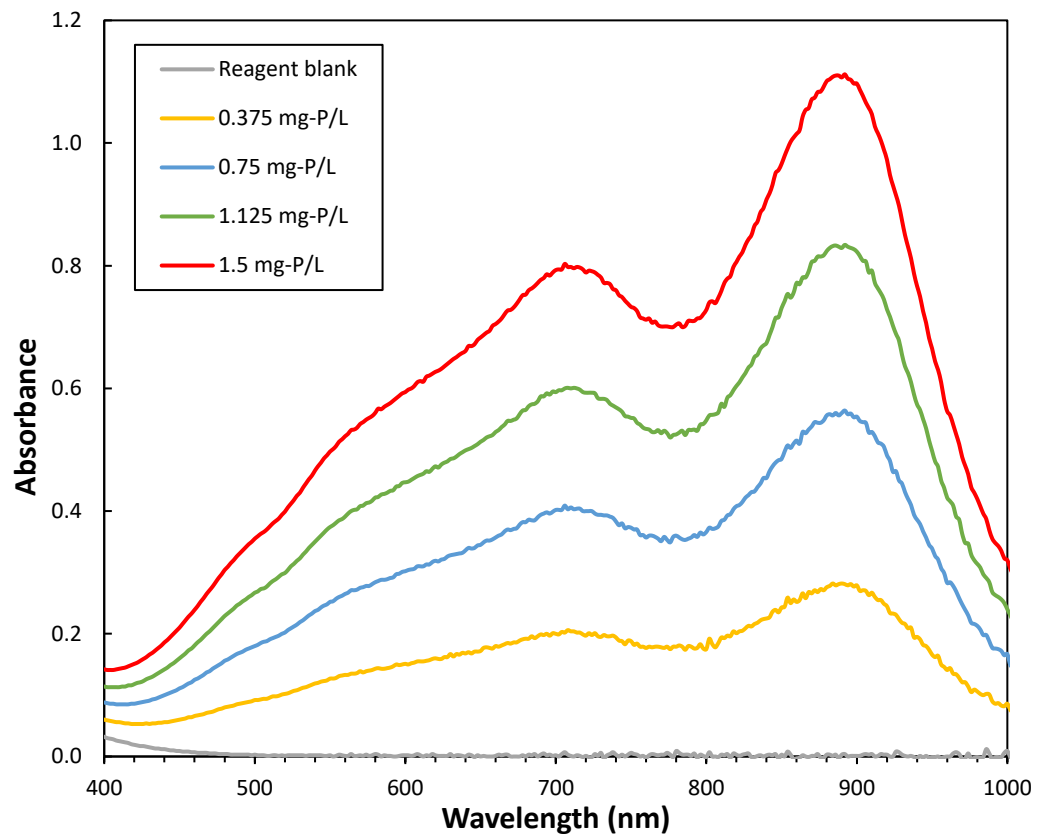


**Figure 3.2** UV-Vis absorbance spectra for five sodium phosphate standard solutions using the molybdenum blue reaction for orthophosphate determination. The reference was ultra-pure deionized water.

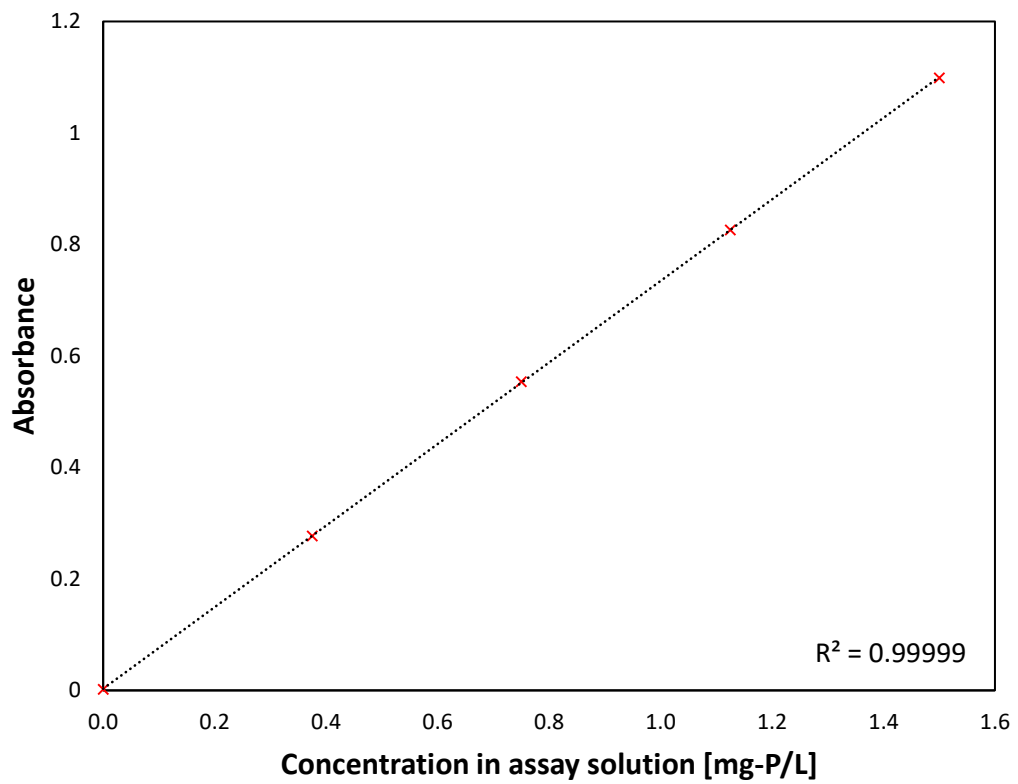


**Figure 3.3** Representative calibration curve for spectrophotometric determination of orthophosphate using the molybdenum blue reaction. The absorbance reading was taken at 880 nm, while the concentration relates to the diluted value in the total 5 mL of assay solution. The reference was ultra-pure deionized water.

### 3.3.5 Spectrophotometric determination of copper

Commercially available test kits were used for copper determination (0.1 – 8.0 mg-Cu/L, Hach Copper TNT860). The manufacturer's instructions for sample preparation were followed, and the absorbance read at 478 nm in a ThermoFisher Genesys 50 UV-Visible spectrophotometer. A calibration curve, Figure 3.4, was constructed using five approximately equally spaced standards across the manufacturer's specified determination range. The validity of the curve was periodically validated by analyzing a standard solution with each new analysis run. The standard solution was prepared by dissolving a measured mass of high-purity copper foil ( $\geq 99.8\%$ ) in a minimum of concentrated nitric acid (70% ACS Plus, Fisher Chemical A200C-212) and subsequent dilution. The volume of concentrated nitric acid was limited to ensure the pH of the diluted solutions did not interfere with the assay.

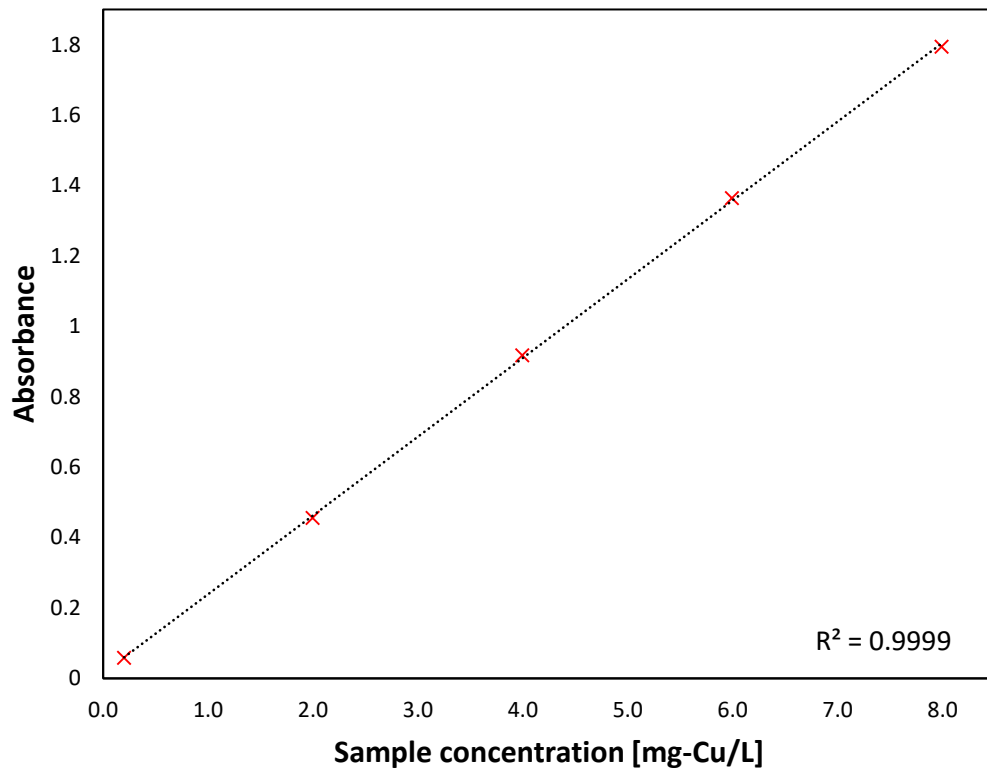


**Figure 3.4** Calibration curve obtained for spectrophotometric determination of copper using the Hach Copper TNT860 test kit. The absorbance reading was taken at 478 nm.

### **3.3.6 Characterization of solid samples**

#### **3.3.6.1 Copper and aluminum content**

The copper and aluminum content of the synthesized Cu-ZSM-5 zeolite was determined by inductively coupled plasma, optical emission spectroscopy (ICP-OES) after digestion with hydrofluoric acid. The assay was completed by MSE Supplies LLC (Tucson, AZ).

The analysis was performed with an Agilent 720ES with the following test parameters: RF Power = 1.20 kW, plasma flow = 15.0 L/min, auxiliary flow = 1.50 L/min, nebulizer flow = 0.75 L/min, sample uptake delay = 15 s, instrument stabilization delay = 15 s, replicate read time = 2 s, replicates = 3. The sample mass used was approximately 50 mg.

#### **3.3.6.2 X-ray powder diffraction (XRD)**

XRD patterns were acquired from a Philips X'Pert PW 3040 Powder x-ray diffractometer (Cu source) and a Bruker D8 Focus x-ray diffractometer with autosampler (Cu source). Samples analyzed with the Philips instrument were prepared by dispersing solid powders in ethanol and drop-casting onto a SiO<sub>2</sub> zero diffraction placed on a warm hot plate set to < 60 °C. Samples analyzed with Bruker instrument



were prepared by compacting powder directly onto a round glass coverslip with a small dot of petroleum jelly to aid in adhesion. We verified that apart from a broad background artifact in the low-angle range for latter, the measurements obtained from both instruments and techniques were comparable. The raw data has been plotted without smoothing or similar processing techniques. However, the intensities of the patterns were normalized by the most intense peak in each pattern for ease of comparison.

### **3.3.6.3 Scanning electron microscopy (SEM)**

SEM images were obtained using a JEOL JSM-6700F Field Emission Scanning Electron Microscope fitted with an Element EDAX detector. Energy-dispersive X-ray spectroscopy (EDS) was used to confirm copper loading into the zeolite.

### **3.3.6.4 Attenuated total reflectance Fourier-transform infrared spectroscopy (ATR-FT-IR)**

Absorbance spectra were obtained using a PerkinElmer Frontier Optica FT-IR equipped with a single-reflection universal attenuated total reflectance (ATR) diamond crystal. All samples were measured as dry powders placed on the diamond crystal and compacted by the pressure arm. A total of 4 accumulation scans were performed for each sample and the resolution set to  $1\text{ cm}^{-1}$ . The raw data has been plotted without

smoothing or similar processing techniques. However, the intensities of the patterns were normalized by the most intense peak in each pattern for ease of comparison.

### **3.3.7 Non-linear regression and equation solving**

Non-linear regression was used to obtain the best fit parameters for relevant non-linear equilibrium and kinetic models. A custom worksheet was developed in Microsoft Excel using the built-in Solver add-in—set to the GRG Nonlinear engine—to minimize the sum of the squared residuals between the experimental data and the data calculated by the model. An initial guess was supplied for the model parameters and full convergence to the default tolerance criteria (0.0001) was achieved (a similar solver routine was implemented for solving non-linear sets of equations). Additionally, the convergence and accuracy of the non-linear regression routine was verified by implementing the solutions in Python. An example script for one calculation is reproduced on the following page.

```
import numpy as np
from scipy.optimize import curve_fit

def func(x,a,b):
    return a*x**b # Freundlich fit

# Data
x = np.array([0.29, 2.03, 19.01, 55.83, 96.55, 143.09,
317.14, 577.21])
y = np.array([0.490880082, 0.912159831, 1.575373825,
2.194915595, 2.690921694, 3.23984289, 4.874926501,
7.234740803])

param, vars_matrix = curve_fit(func,x,y)
variance = np.diagonal(vars_matrix)
SE = np.sqrt(variance)

results = {'a':[param[0],SE[0]],'b':[param[1],SE[1]]}

print("Parameter\tValue\t\tStdError")
for v,c in results.items():
    print(v,"\t",c[0],"\t",c[1])
```

The chi-squared metric ( $\chi^2$ )—calculated per equation 2 [63]—was used to evaluate and compare the goodness of fit of relevant models.

$$\chi^2 = \sum \frac{(q_{exp} - q_{calc})^2}{q_{calc}} \quad (\text{Equation 2})$$

$R^2$  was not used to compare and evaluate inherently non-linear models in this work, despite its frequent (mis)use in the adsorption literature and availability in software packages. The  $R^2$  metric is not appropriate for evaluating goodness of fit in regression where the model is non-linear in the parameters [91].

### 3.3.8 Error analysis

All reported error estimates have been derived using standard error propagation relations, unless otherwise noted. For input to these calculations, the specified tolerance was used for laboratory equipment (e.g., micropipette, glassware) while for the calibration curves obtained by linear regression, the 95% confidence intervals associated with the slope and intercept were used as the error inputs. Error estimates were not obtainable for the ICP-OES analysis conducted by the external analytical laboratory. Therefore, the error in this data was estimated at 5%.

## **Chapter 4 Results**

### **4.1 Introduction**

This chapter presents the results obtained by implementing the methods outlined in Chapter 3. After reporting data relating to the necessary characterization of the materials, this section will delineate the results into two broad areas consistent with the objectives of the thesis: the characteristics of copper ZSM-5 as sorption material for phosphate in general, and the phosphate adsorption properties of copper ZSM-5 as they relate to active sites and structure of the material itself.

### **4.2 Molybdenum blue assay for inorganic dissolved phosphate**

The molybdenum blue assay was validated for its suitability as a precise quantification method for orthophosphate in the context of this study. Although the technique has been well studied, confusion persists regarding its limitations; many modifications presented in the literature do not discuss validation of the technique for the specific conditions to which the assay is applied [74], [85]. Therefore, a comprehensive validation of the specific implementation of the assay technique used in this dissertation (as presented in presented in section 3.3.4) was completed. Figure 4.1 summarizes some of the key

## RESULTS

results of the validation studies. Figure 4.1A shows that addition of the antimony salt stabilized the blue complex measured at 880 nm for at least two hours, which confirmed the results presented and discussed in the literature [85], [87], [90]. The rapid increase in absorbance noted when the antimony salt was omitted indicates that such methods may be inherently more difficult to execute with a high degree of precision, regardless of any potential improvements in execution speed. Studies that have used this implementation for measuring phosphate adsorption do not always explain the motivation [74]. Figure 4.1B indicates that the assay was valid across the pH range expected for this study, at the typical dilutions required for a sample with 100 mg-P/L dissolved phosphate. In other words, no pH interference was observed under these conditions; the working pH for complex formation was not disturbed significantly by alkalinity of certain samples that were expected in this study. Figure 4.1C and Figure 4.1D illustrate the results of salt spiking studies to assess any interference effects at high loadings of  $\text{Na}^+$  (and  $\text{Cl}^-$ ). At the high assay phosphate concentration, there was a slight negative interference observed up to 1 g/L NaCl, which is consistent with the salt effect noted in the literature [85]. This effect was not detectable at the low assay phosphate concentration. However, at the highest salt spike, a positive interference of  $\sim 0.08$  mg-P/L was observed. This was most likely due to phosphate or arsenic impurities in the sodium chloride reagent registering at higher concentrations. The expected concentration of non-phosphate species (in particular,  $\text{Na}^+$ ) after dilution to the final assay concentration was  $\ll 2$  g/L. Therefore, expected levels of  $\text{Na}^+$  due to

## RESULTS

addition of salts or NaOH was confirmed to not create an interference bias in the phosphate adsorption data. This validation was consistent with the recommendation—Na<sup>+</sup> interference level of 1 g/L—published by a commercial test kit based on similar assay chemistry [92].

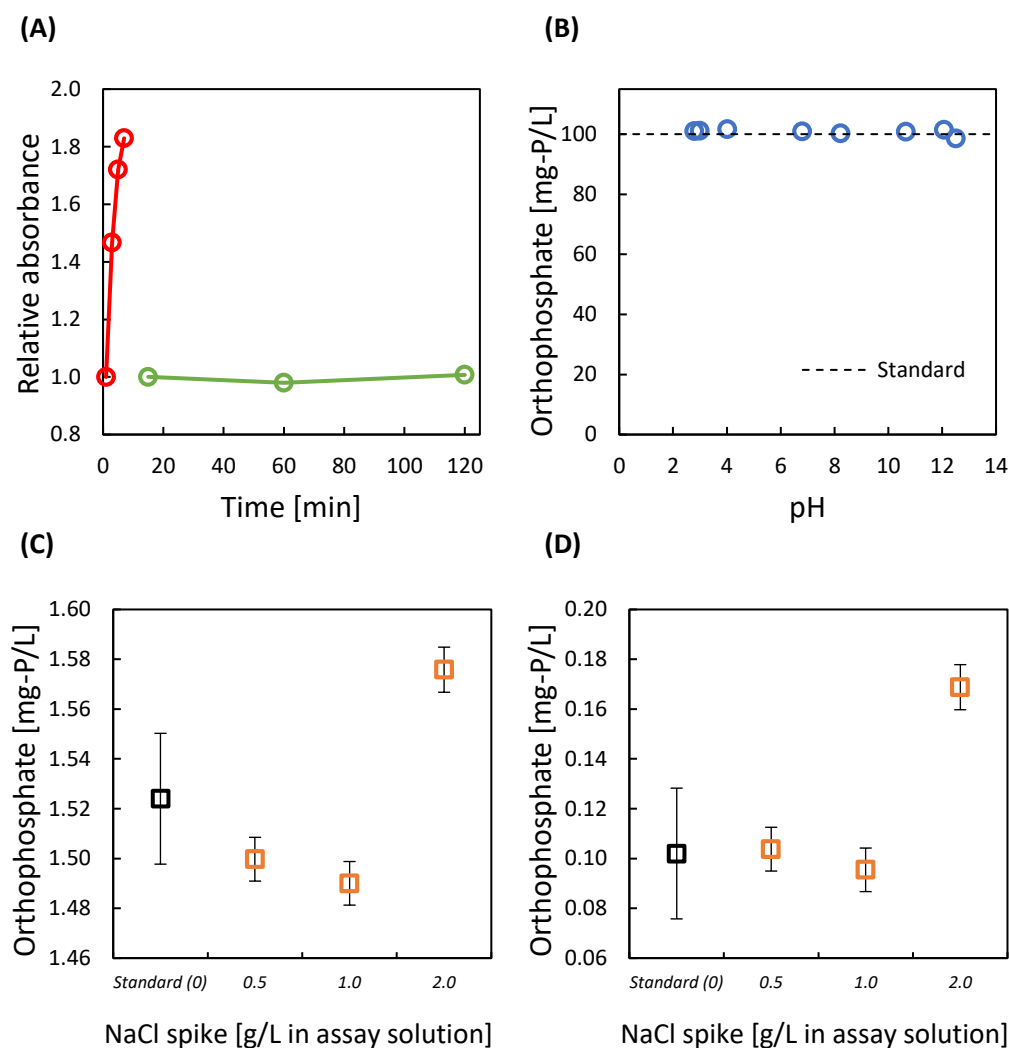


**Figure 4.1** Summary of validation studies for the molybdenum blue assay used in this dissertation. (A) Stability of the molybdenum blue phosphate complex using the methodology presented (green  $\circ$ ) and the result of omitting potassium antimonyl tartrate from the mixed reagent solution (red  $\circ$ ), (B) Measured phosphate concentrations for  $100 \pm 1$  mg-P/L standards prepared at different pH conditions (the error bars are smaller than the size of the markers), (C) Measured interference effect from salt spikes at 1.5 mg-P/L, (D) Measured interference effect from salt spikes at 0.1 mg-P/L.



### 4.3 Characterization of Copper ZSM-5

The synthesized copper ZSM-5 zeolites were characterized for their copper and aluminum content by ICP-OES. Table 4.1 summarizes the results of this analysis, along with derived data. The Cu/Al ratio is indicative of the extent of exchange achieved through ion exchange with the copper(II) acetate. In theory, a simple charge balance indicates that one extra-framework  $\text{Cu}^{2+}$  ion balances two framework Al sites; each Al site carries a single negative charge owing to the substitution of  $\text{Si}^{4+}$  by  $\text{Al}^{3+}$ . The Cu/Al molar ratio was greater than 0.4 for all samples, indicating almost complete exchange was achieved.

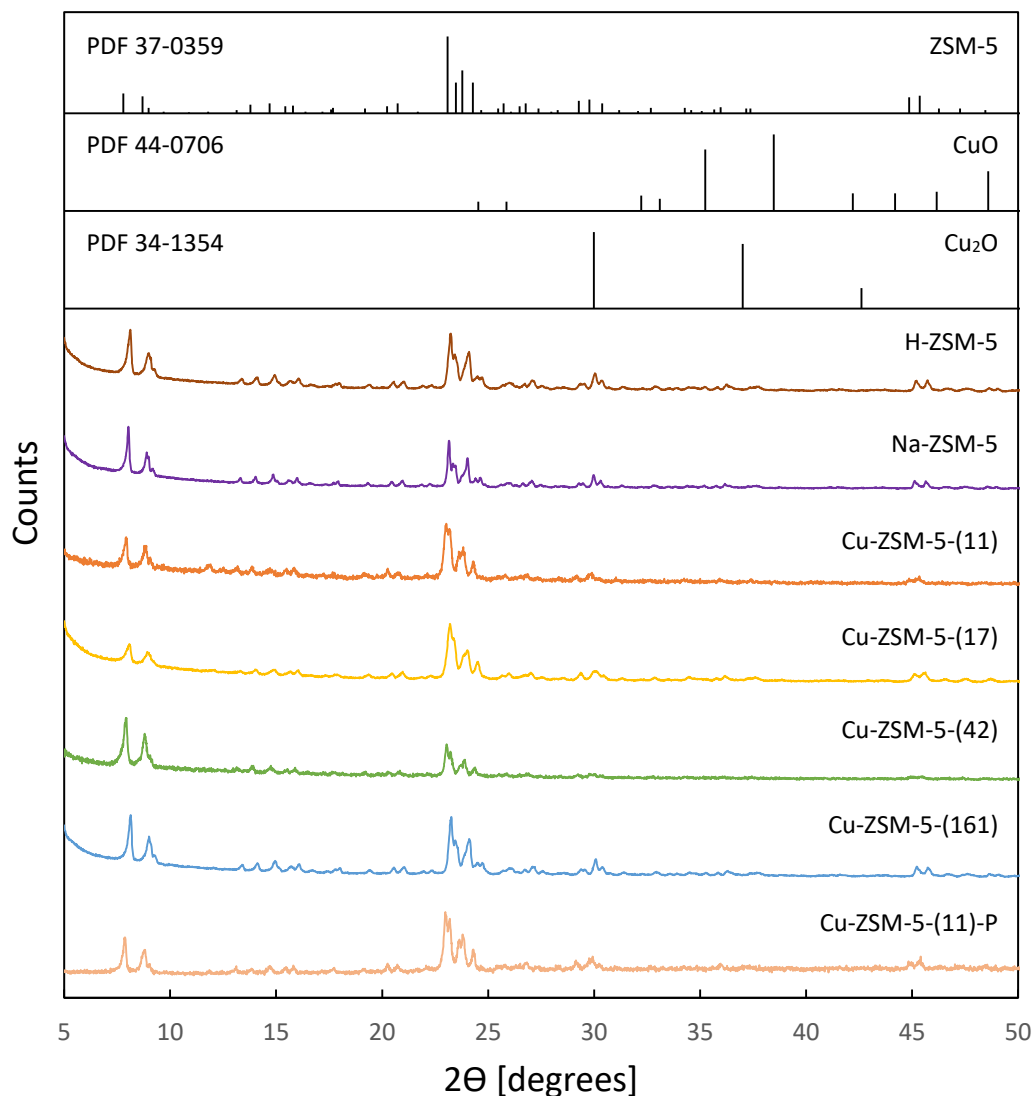
**Table 4.1** Metals analysis for the Cu-ZSM-5 samples synthesized for this study

<b>Si/Al molar ratio</b>	<b>Cu (%w/w)</b>	<b>Al (%w/w)</b>	<b>Cu/Al molar ratio</b>	<b>Cu molar loading (<math>\mu\text{mol/g}_{\text{zeolite}}</math>)</b>	<b>Cu site density (per <math>1000 \text{ \AA}^3</math>)<sup>a</sup></b>	<b>Average Cu...Cu distance (<math>\text{\AA}</math>)<sup>b</sup></b>
11	3.89	3.43	0.48	612	0.66	14.3
17	2.18	2.24	0.41	343	0.37	17.3
42	1.39	0.93	0.63	219	0.24	20.1
161	0.34	0.20	0.75	54	0.06	32.1

<sup>a</sup> Calculated using the theoretical crystal density of ZSM-5,  $1.785 \text{ g/cm}^3$  [93].

<sup>b</sup> Calculated assuming uniform distribution of Cu and Al [94].

XRD was used to evaluate the synthesized Cu-ZSM-5 for identifiable crystalline phases. Specifically, the materials were analyzed for the presence of undesirable bulk copper oxides (indicative of copper deposition in excess of the capacity for extra-framework ions) and to validate the MFI framework of ZSM-5 after ion exchange. Figure 4.2 compares the XRD patterns obtained for Cu-ZSM-5 at the five synthesized Si/Al ratios with reference data for ZSM-5, CuO and Cu<sub>2</sub>O. Along with the selected H-ZSM-5 and Na-ZSM-5 samples—intermediate materials in the synthesis procedure—the patterns for Cu-ZSM-5 show close agreement to the reference pattern for ZSM-5. This indicates the framework maintained its structure through subsequent ion exchange and calcination treatment. Similarly, the absence of discernable CuO or Cu<sub>2</sub>O peaks suggests these species were not produced as bulk crystalline phases. In addition, the provided pattern for Cu-ZSM-5-(11) after phosphate adsorption, Cu-ZSM-5-(11)-P, was similar to the pattern for the pristine material, indicating the phosphate adsorption did not alter the crystal structure of the zeolite.

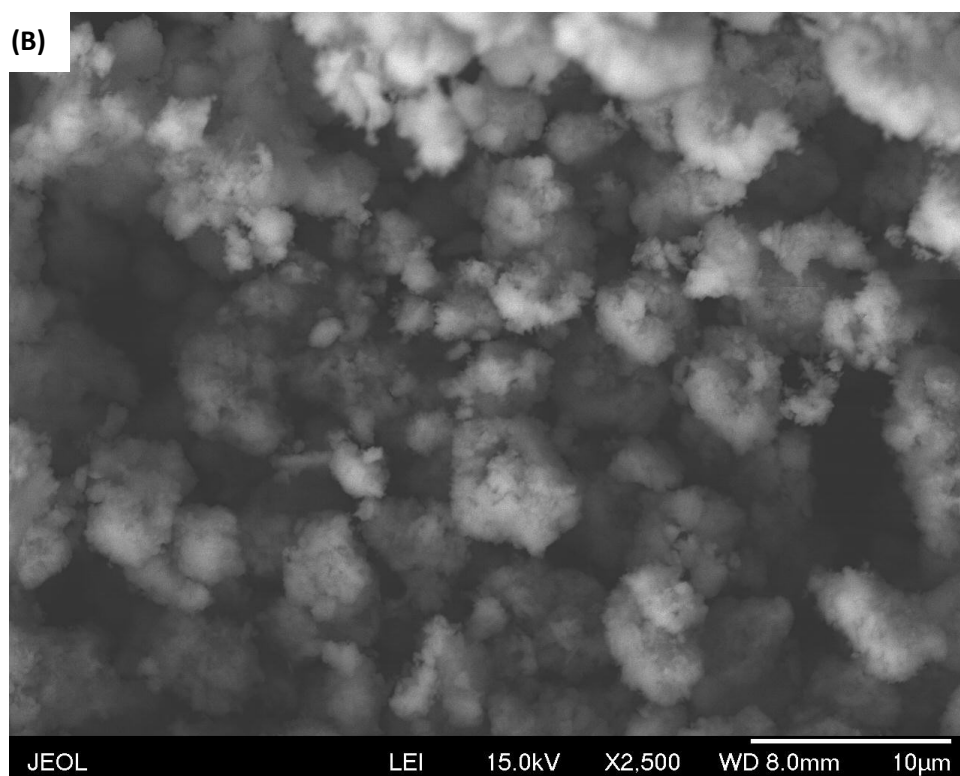
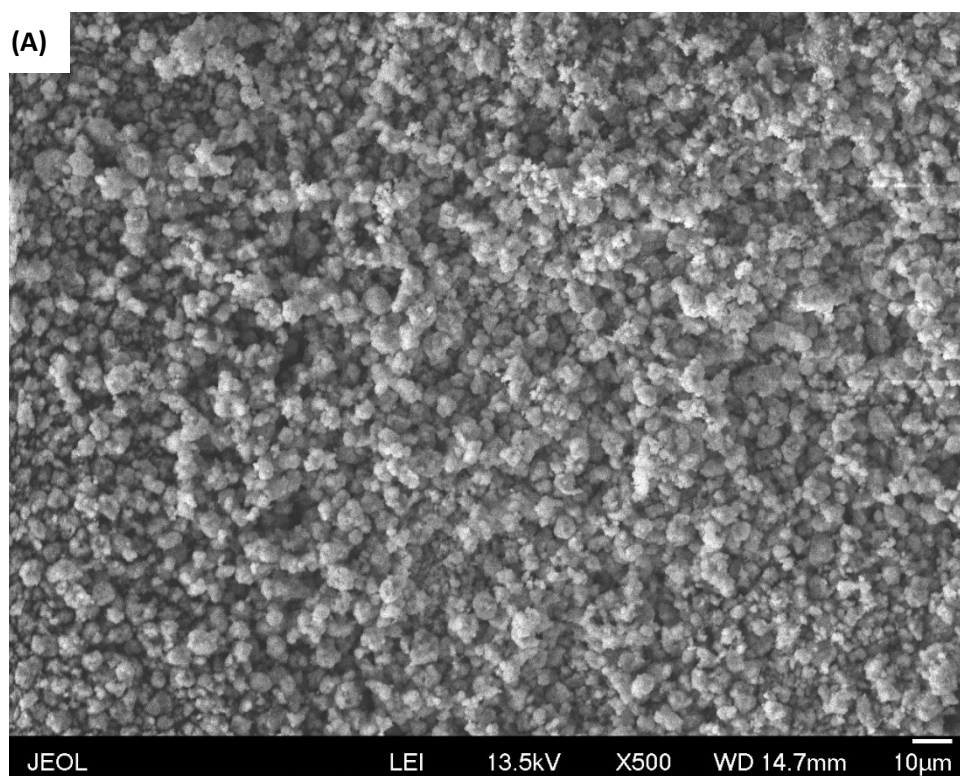


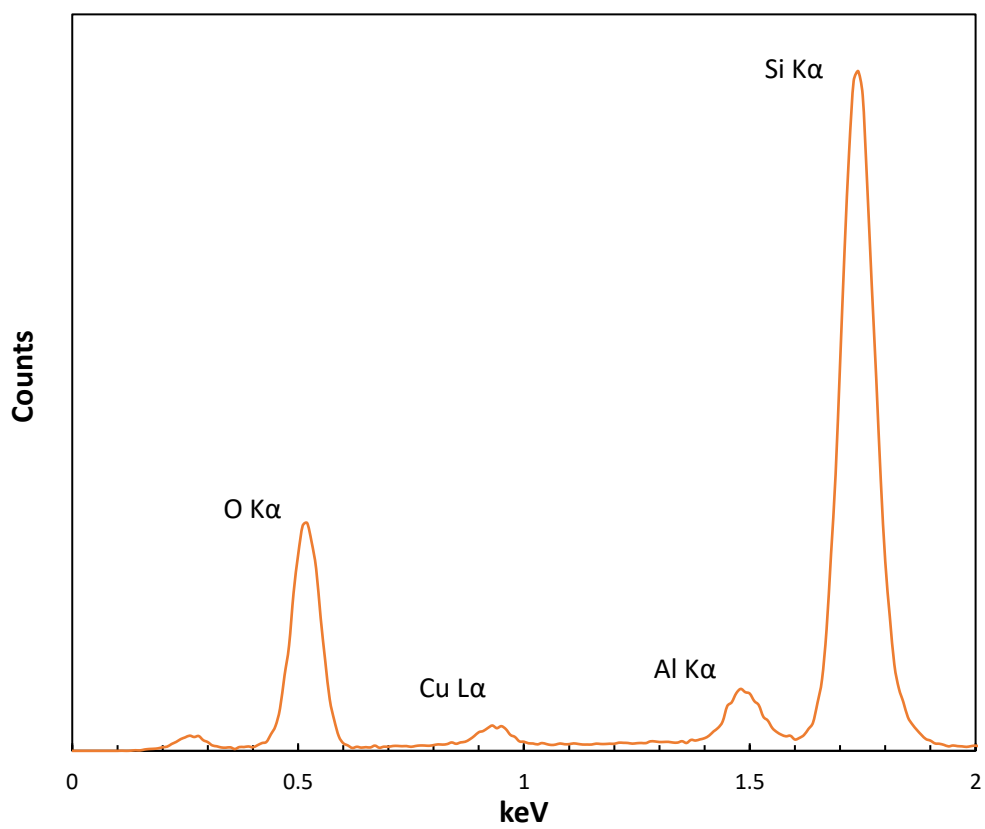
**Figure 4.2** XRD patterns of the four synthesized Cu-ZSM-5 zeolites used in this study, along with selected patterns for H-ZSM-5 and Na-ZSM-5. Cu-ZSM-5-(11)-P is a pattern for Cu-ZSM-5-(11) material after phosphate adsorption. Reference patterns are provided for ZSM-5, CuO and Cu<sub>2</sub>O, indicating preservation of the zeolite framework and no detectable crystalline copper oxide species. H-ZSM-5 and Na-ZSM-5 patterns are for Si/Al ratio 161 and are representative of the patterns obtained for the other all Si/Al ratio materials.

Figure 4.3 shows SEM images for the Si/Al ratio 11 material, Cu-ZSM-5-(11), as-synthesized. The images revealed irregular particle sizes generally less than 10  $\mu\text{m}$ . The corresponding EDS spectra, illustrated in Figure 4.4, revealed qualitative confirmation of copper loading in ZSM-5 by the ion exchange method through the positive identification of the Cu  $L\alpha$  peak at 0.93 keV; the copper content was quantitatively characterized by ICP-OES as shown earlier in Table 4.1. Further electron microscopy and Brunauer–Emmett–Teller (BET) analysis of Cu-ZSM-5 synthesized by the ion exchange method have already been reported extensively elsewhere by our research group [74], [95]. Based on this work, the BET surface area of the materials used in this study were estimated to fall in the  $\sim 370 - 400 \text{ m}^2/\text{g}$  without any meaningful correlation to the Si/Al ratio; the specific surface areas for the zeolites used in this study (before any ion exchange) were reported in Table 3.1 and were in the  $\sim 440 - 460 \text{ m}^2/\text{g}$  range.

**Figure 4.3** SEM images for Cu-ZSM-5-(11). (A) Low magnification image showing particles of  $\sim 10 \mu\text{m}$  in size, (B) Higher magnification image showing irregular particle sizes and shapes less than  $10 \mu\text{m}$  in size.

## RESULTS





**Figure 4.4** Energy-dispersive X-ray spectroscopy (EDS) spectra obtained for Cu-ZSM-5-(11).

## RESULTS

ATR-FT-IR analysis was performed on the as-synthesized Cu-ZSM-5 material at two Si/Al ratios, along with samples obtained after phosphate adsorption. The results are shown in Figure 4.5. The spectra of all materials feature major features at  $\sim 1220\text{ cm}^{-1}$ ,  $\sim 1050\text{ cm}^{-1}$  and  $\sim 800\text{ cm}^{-1}$  that were ascribed to the ZSM-5 lattice vibrations [96]. The first near  $1220\text{ cm}^{-1}$  was identified as the Si–O asymmetric stretching band, which is unique to zeolites featuring chains of five-membered rings such as ZSM-5; the symmetric stretching of T–O in the external linkages was responsible for the feature near  $800\text{ cm}^{-1}$ . The broader, most intense peak near  $1050\text{ cm}^{-1}$  was assigned to both asymmetric and symmetric bending vibrations of T–O from the internal tetrahedra. The spectra for Cu-ZSM-5-(42) featured this peak at slightly higher wavenumbers than Cu-ZSM-5-(11), which could be explained by the difference in Si/Al ratio. The materials analyzed after phosphate adsorption did not display any unique peaks compared to the pristine samples, although a slight peak shift to lower wavenumbers was observed for Cu-ZSM-5-(11) (low, medium and high) and Cu-ZSM-5-(42) (high). Vibrations of P–O bonds in the  $[\text{PO}_4]^{3-}$  tetrahedron in the available data range are generally found at  $\sim 1000$  to  $1100\text{ cm}^{-1}$  depending on the non-tetrahedral cation [97], [98]. Therefore, these peaks appear to have been obscured by the strong absorption band of the zeolite framework. However, the slight changes in peak shape and position may have been a result of the contributions of P–O vibrational features associated with adsorbed phosphate species, though of too small a magnitude to be meaningfully extracted through deconvolution methods. The faint peaks visible near  $\sim 1630\text{ cm}^{-1}$  in all spectra



## RESULTS

were ascribed to H<sub>2</sub>O bending in trace amounts of liquid water remaining in the zeolite samples [99].

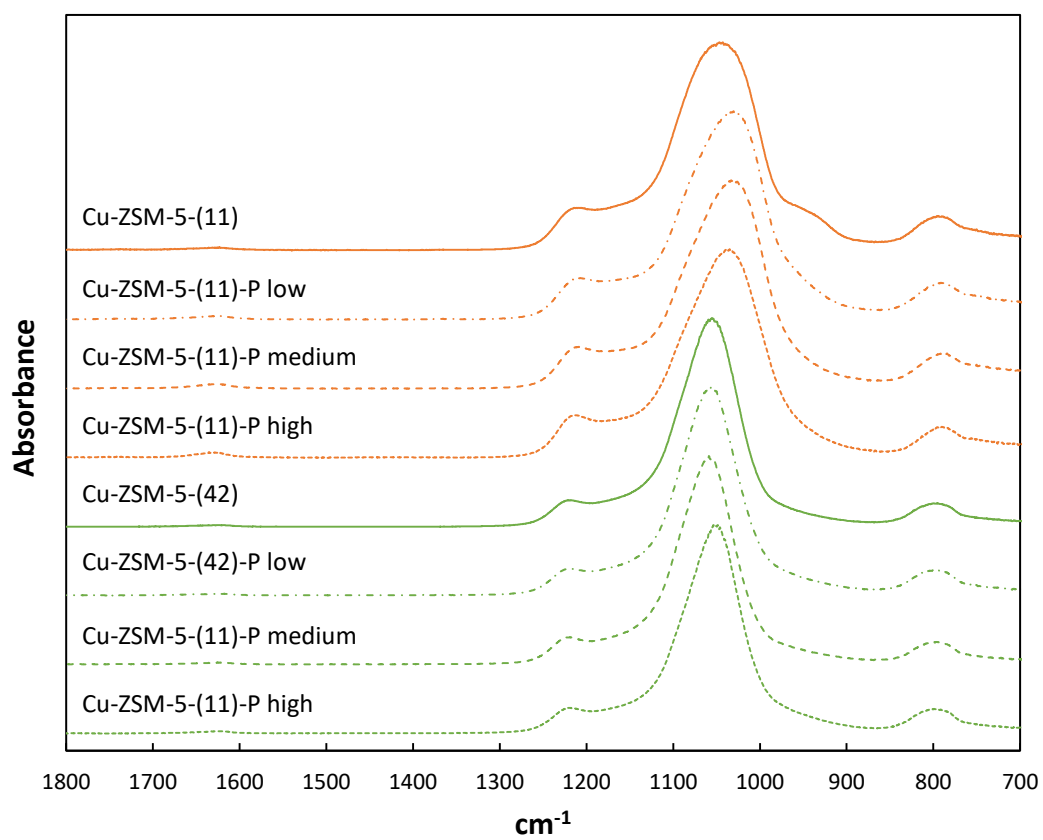


**Figure 4.5** ATR-FT-IR absorbance spectra for pristine Cu-ZSM-5 and samples after phosphate adsorption across the range of initial phosphate concentrations studied.

## 4.4 Copper ZSM-5 as a sorbent for phosphate

### 4.4.1 Adsorption uptake

The performance of Cu-ZSM-5 for phosphate removal by adsorption was tested at room temperature, a concentration of 10 mg-P/L and initial solution pH of 7. These conditions approximate those likely to be encountered in waste-water treatment or environmental streams without significant pre-concentration. The results presented in Figure 4.6 show an effective equilibrium was reached after approximately 12 hours for all Si/Al ratios. The Cu-ZSM-5-(11) sample displayed the greatest phosphate removal performance, with a capacity of 0.38 mg-P/g<sub>zeolite</sub>, or approximately 76%. The observed trend in phosphate removal performance by Si/Al ratio was 11 > 17 > 42, with P removal percentages of 76%, 54% and 50%, respectively, after 24 hours.

The phosphate uptake by Cu-ZSM-5-(161) was not high enough to be reliably quantified using the difference method shown in equation 1 (section 3.3.2); the sensitivity of the molybdenum blue assay technique to slight differences in phosphate concentration was insufficient to obtain meaningful results. Therefore, Cu-ZSM-5-(161) was omitted from these results and further adsorption analysis.

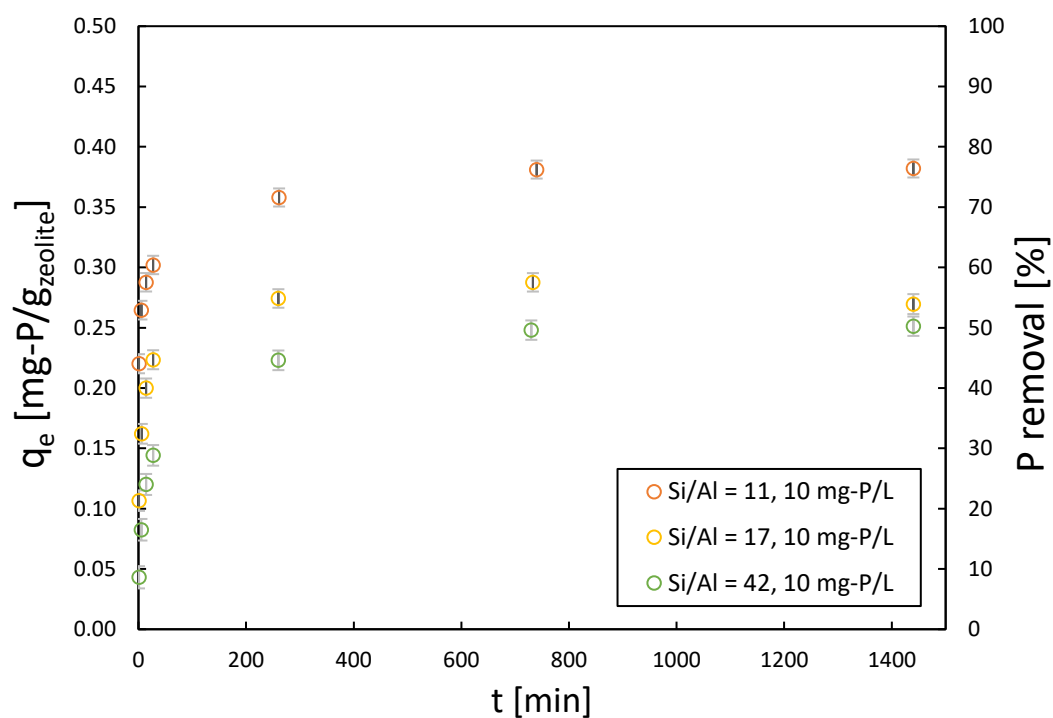


**Figure 4.6** Room temperature phosphate adsorption performance of Cu-ZSM-5 at 10 mg-P/L over 24 hours. The initial pH of the solution was 7 and the sorbent loading was 20 g/L. Phosphate adsorption by Cu-ZSM-5-(161) was below the quantification threshold and has been omitted from the figure.

#### 4.4.2 Adsorption isotherms

The adsorption isotherms of orthophosphate on Cu-ZSM-5 were measured and are displayed in Figure 4.7 (without normalization by copper content); the temperature was  $20 \pm 2$  °C and the initial pH was 7. The results in Figure 4.7 show that for all Si/Al ratios, the adsorption uptake ( $q_e$ ) increased with increasing equilibrium orthophosphate concentration. The magnitude of phosphate adsorption was greatest for Cu-ZSM-5-(11) across the measured concentration range, followed by Cu-ZSM-5-(17) and then Cu-ZSM-5-(42).

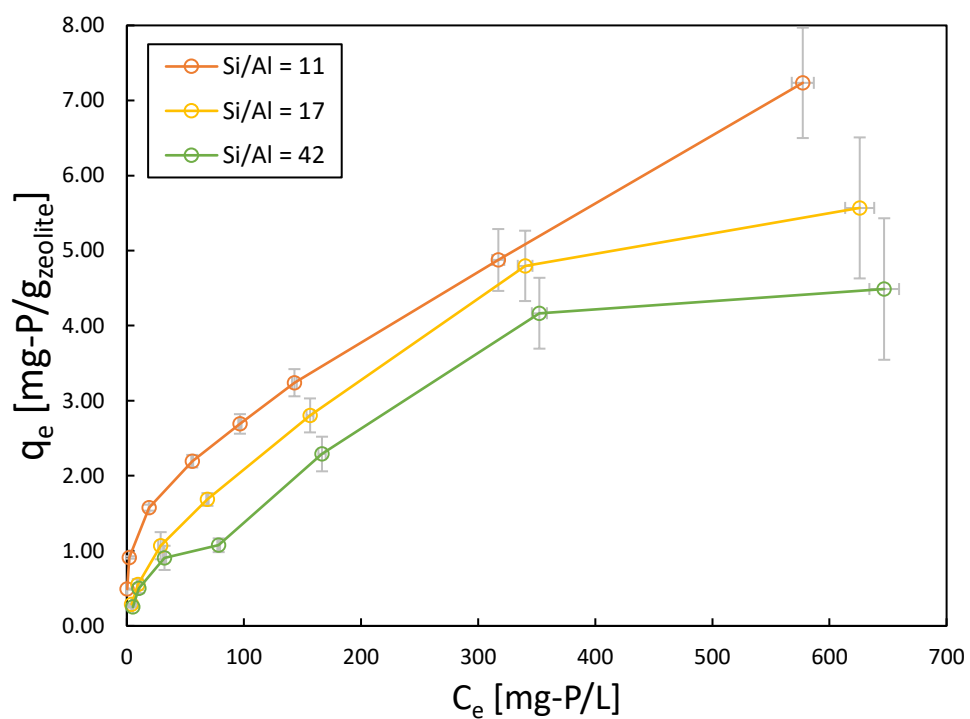


**Figure 4.7** Phosphate adsorption isotherms obtained for Cu-ZSM-5 at  $20 \pm 2$  °C and neutral pH. The sorbent loading was 20 g/L. The horizontal axis,  $C_e$ , represents the equilibrium concentration.

The adsorption isotherm data was fitted to Langmuir and Freundlich models, shown in equations 3 and 4, respectively [100], [101]. The isotherm parameters were obtained by non-linear regression of the adsorption data. The results and  $\chi^2$  values for the regressions are presented in Table 4.2.

$$q_e = \frac{Q_{max}^0 K_L C_e}{1 + K_L C_e} \left[ \frac{mg-P}{g} \right] \quad (\text{Equation 3, Langmuir})$$

$$q_e = K_F C_e^{1/n} \left[ \frac{mg-P}{g} \right] \quad (\text{Equation 4, Freundlich})$$

According to the  $\chi^2$  metric, the empirical Freundlich adsorption isotherm model provided a better fit to the experimental adsorption data for Cu-ZSM-5 across all Si/Al ratios. Figure 4.8 illustrates the adsorption isotherm data fitted to the Freundlich model. The Freundlich intensity parameter,  $1/n$ , was less than 1 indicating favorable adsorption. Cu-ZSM-5-(11) featured the lowest intensity parameter (most favorable adsorption or highest degree of surface adsorption site heterogeneity), followed by Si/Al ratio 17 and then 42. The reverse trend was observed for the Freundlich constant,  $K_F$ . According to the poorer fitted Langmuir model, the maximum adsorption capacity for Cu-ZSM-5 across all studied Si/Al ratios was 9.8 mg-P/g<sub>zeolite</sub>.

**Table 4.2** Langmuir and Freundlich isotherm parameters obtained by non-linear regression for adsorption of phosphate by Cu-ZSM-5.

Si/Al	Langmuir			Freundlich		
	$Q^0_{\max}$ (mg-P/g <sub>zeo</sub> )	$K_L$ (L/mg-P)	$\chi^2$	1/n	$K_F$ (mg-P/g <sub>zeo</sub> )(L/mg-P) <sup>1/n</sup>	$\chi^2$
11	9.8	0.0039	31.0	0.49	0.30	1.35
17	7.8	0.0042	0.5	0.53	0.19	0.15
42	6.8	0.0034	0.7	0.56	0.13	0.31



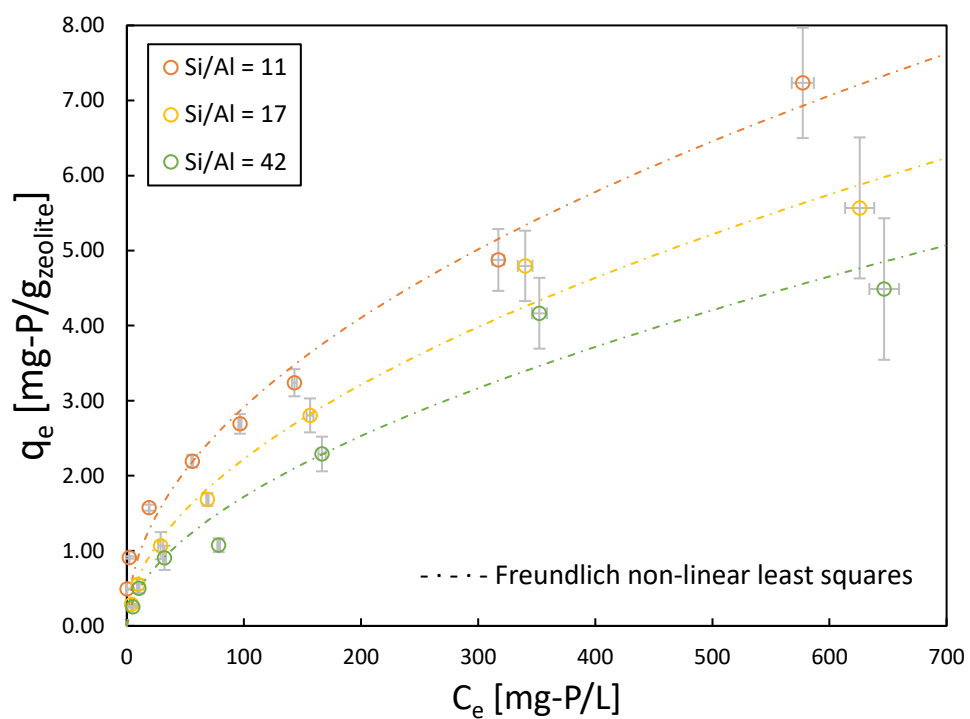


**Figure 4.8** Phosphate adsorption isotherm data for Cu-ZSM-5 fitted to the empirical Freundlich model by non-linear least squares regression.

### 4.4.3 Effect of pH

The effect of the initial solution pH was studied for the lowest and highest Si/Al ratio copper ZSM-5 materials—11 and 42—which correspond to the materials with highest and lowest copper contents, respectively. In addition, the unexchanged zeolites—defined here as Na-ZSM-5 prior to copper ion exchange—were included as negative controls for the presence of copper as the extra framework ion. Figure 4.9 illustrates the measured dependence of phosphate uptake on initial solution pH ( $\text{pH}_0$ ) at a constant starting concentration of 100 mg-P/L; all other conditions remained unchanged.

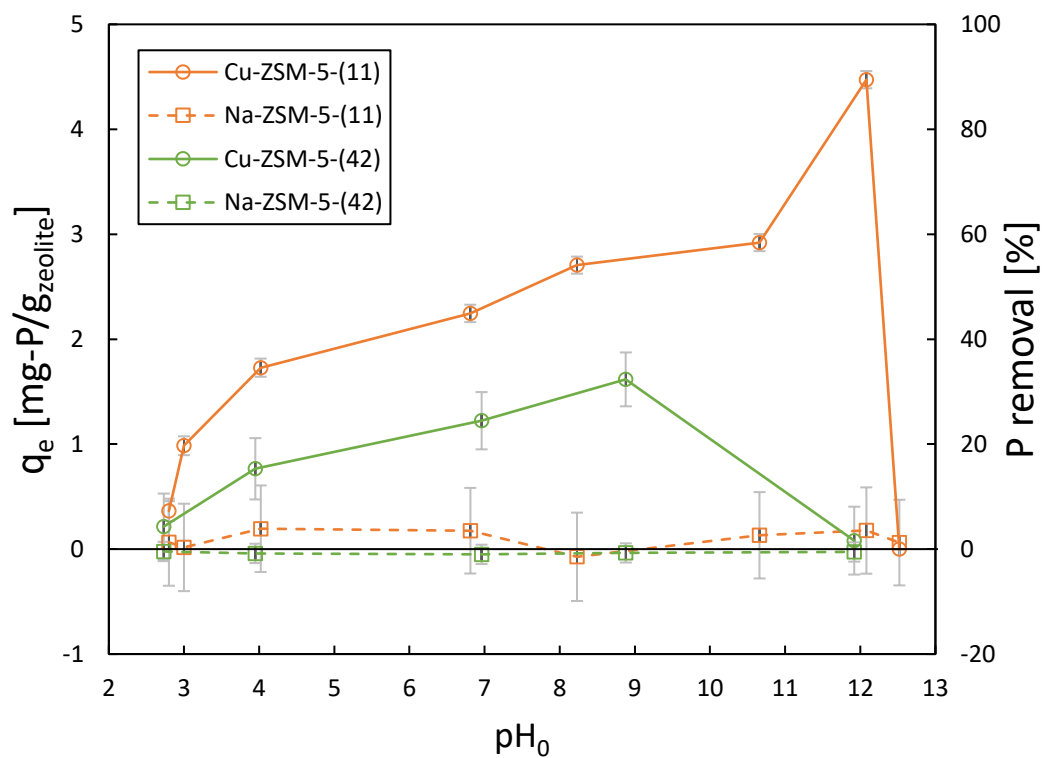


**Figure 4.9** Effect of initial pH on phosphate adsorption over a wide range of initial pH values for Cu-ZSM-5 and Na-ZSM-5 at Si/Al ratios of 11 and 42. The initial concentration of phosphate was 100 mg-P/L.

## RESULTS

The results show that phosphate adsorption increased with increasing pH for both Cu-ZSM-5-(11) and Cu-ZSM-5-(42), but dropped to zero at strongly alkaline pH values of 11.9 and 12.5, respectively. For the same materials, at pH ~2.8—the lowest pH solution used—phosphate adsorption was less than 0.5 mg-P/g<sub>zeolite</sub> or less than 10% of phosphate initially available. Cu-ZSM-5-(42) revealed a lower uptake than Cu-ZSM-5-(11) across the pH range. However, the difference was approximately constant at ~1 mg-P/g<sub>zeolite</sub> from pH 4 to 9; the difference is consistent with the adsorption isotherm data collected at neutral pH. The maximum measured phosphate adsorption for Cu-ZSM-5-(11) was 4.5 mg-P/g<sub>zeolite</sub> (or 89% P removal) at pH 12.1, while the maximum obtained value for Cu-ZSM-5-(42) was 1.6 mg-P/g<sub>zeolite</sub> (or 32% P removal) at pH 8.9; both represented improvements over neutral conditions of ~100% and ~33%, respectively. However, it should be noted that the maximums reported did not represent global maximums over the studied pH range, owing to the finite number of sampling points. The Na-ZSM-5 controls did not exhibit significant phosphate uptake anywhere in the studied pH range. Therefore, copper was confirmed to be the active site for phosphate adsorption in Cu-ZSM-5.

The change in pH of the solution owing to the addition of Cu-ZSM-5 sorbents and phosphate adsorption was investigated. The  $\Delta\text{pH}$  (i.e.,  $\text{pH}_e - \text{pH}_0$ ) was calculated from initial and final equilibrium pH measurements and evaluated as a function of  $\text{pH}_0$ , as shown in Figure 4.10.

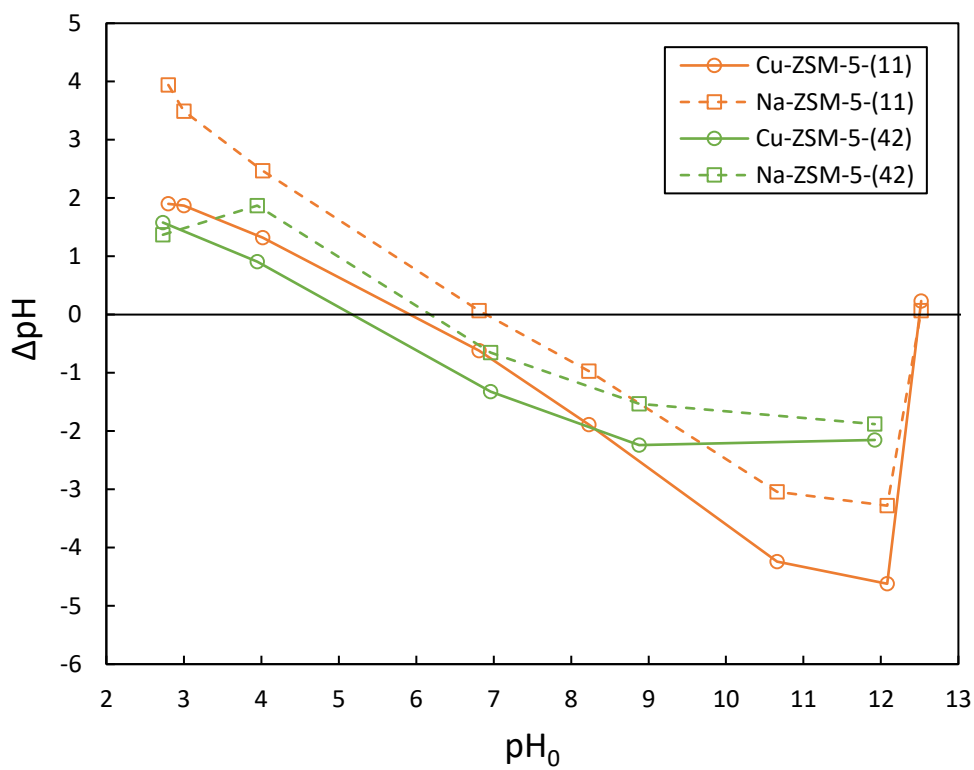


**Figure 4.10** Change in pH of solutions due to the addition of ZSM-5 sorbents and phosphate adsorption for a wide range of initial pH values. The initial concentration of phosphate was 100 mg-P/L.

The results in Figure 4.10 show that  $\Delta\text{pH}$  decreased with increasing initial pH for all tested ZSM-5 materials. However, at pH  $\sim 12$ , off-trend behavior was observed; this is consistent with the findings shown in Figure 4.9, where phosphate adsorption deviated and dropped to zero at extreme alkaline conditions. The  $\Delta\text{pH}$  profiles for Na-ZSM-5-(11) and Na-ZSM-5-(42) displayed similar behavior to their corresponding copper ZSM-5 materials, despite the absence of exchanged copper and phosphate adsorption. However, there was generally a consistent offset between the unexchanged and copper-exchanged materials. More generally,  $\Delta\text{pH}$  vs.  $\text{pH}_0$  profiles reflect the charge on a material's surface, and the point of zero net proton charge (PZNPC) can be estimated from the location where  $\Delta\text{pH}$  equals zero; in other words,  $\text{pH}_0 = \text{pH}_{\text{PZNPC}}$  when  $\Delta\text{pH} = 0$  [102]. The  $\text{pH}_{\text{PZNPC}}$  for Cu-ZSM-5-(11) and Cu-ZSM-5-(42) were estimated to equal 5.9 and 5.1, respectively; for Na-ZSM-5-(11) and Na-ZSM-5-(42) the values were estimated to equal 6.9 and 6.1, respectively. Therefore, for both Si/Al ratios, the  $\text{pH}_{\text{PZNPC}}$  was lower for the copper-exchanged zeolite compared to the unexchanged material. When considering the same class of sorbent (i.e., Cu-ZSM-5 or Na-ZSM-5), a lower  $\text{pH}_{\text{PZNPC}}$  was associated with the higher Si/Al ratio.

The  $\Delta\text{pH}$  vs.  $\text{pH}_0$  plots and the resulting  $\text{pH}_{\text{PZNPC}}$  values provide some insight in terms of the charge structure of the Cu-ZSM-5 surface. First, the ionic potentials (i.e., charge divided by estimated ionic radius in Å) were calculated for  $\text{Si}^{4+}$ ,  $\text{Al}^{3+}$ ,  $\text{Cu}^{2+}$  and  $\text{Na}^+$ : 10.0, 5.6, 2.7 and 1.0, respectively [103]. Based on this, the lower  $\text{pH}_{\text{PZNPC}}$  of Na-ZSM-

## RESULTS

5 going from Si/Al ratio 11 to 42 can be attributed to the lower number of Al host sites in the framework. Compared to Na-ZSM-5-(11), the Na-ZSM-5-(42) structure has fewer sites where high ionic potential  $\text{Si}^{4+}$  has been replaced by the comparatively low ionic potential  $\text{Al}^{3+}/\text{Na}^+$  pair. Because the high ionic potential of  $\text{Si}^{4+}$  makes it more effective at repelling  $\text{H}^+$ , Na-ZSM-5-(42) has a lower  $\text{pH}_{\text{PZNPC}}$ ; in other words,  $\Delta\text{pH}$  at a given  $\text{pH}_0$  is generally lower. This is consistent with the results shown in Figure 4.10. Given the order of ionic potentials ( $\text{Si}^{4+} > \text{Al}^{3+} > \text{Cu}^{2+} > \text{Na}^+$ ), similar arguments can be made for the observed difference going from Cu-ZSM-5-(42) to Cu-ZSM-5-(11), and when comparing Cu-ZSM-5 to Na-ZSM-5 at the same Si/Al ratio. In considering the regions away from  $\text{pH}_0 \sim 7$ , it should be noted that the  $\Delta\text{pH}$  results displayed somewhat unusual behavior at the extremes; this was likely due to chemical instability of the zeolite, especially under alkaline conditions.

Considering that the final equilibrium pH is different to the initial pH of the phosphate solution, the phosphate adsorption can also be evaluated as a function of  $\text{pH}_e$  rather than initial pH; this analysis is shown in Figure 4.11. The results show that phosphate adsorption sharply increased with increasing  $\text{pH}_e$ . The compression of the active pH range in going from  $\text{pH}_0$  to the  $\text{pH}_e$  coordinate was a result of the  $\Delta\text{pH}$  behavior already depicted in Figure 4.10. The results here (Figure 4.11) show maximum adsorption for Cu-ZSM-5-(11) and Cu-ZSM-5-(42) both occurred at similar, near-neutral equilibrium

## RESULTS

pH conditions (within one unit). This suggested the possibility of a common upper limit on equilibrium pH for non-zero phosphate adsorption.



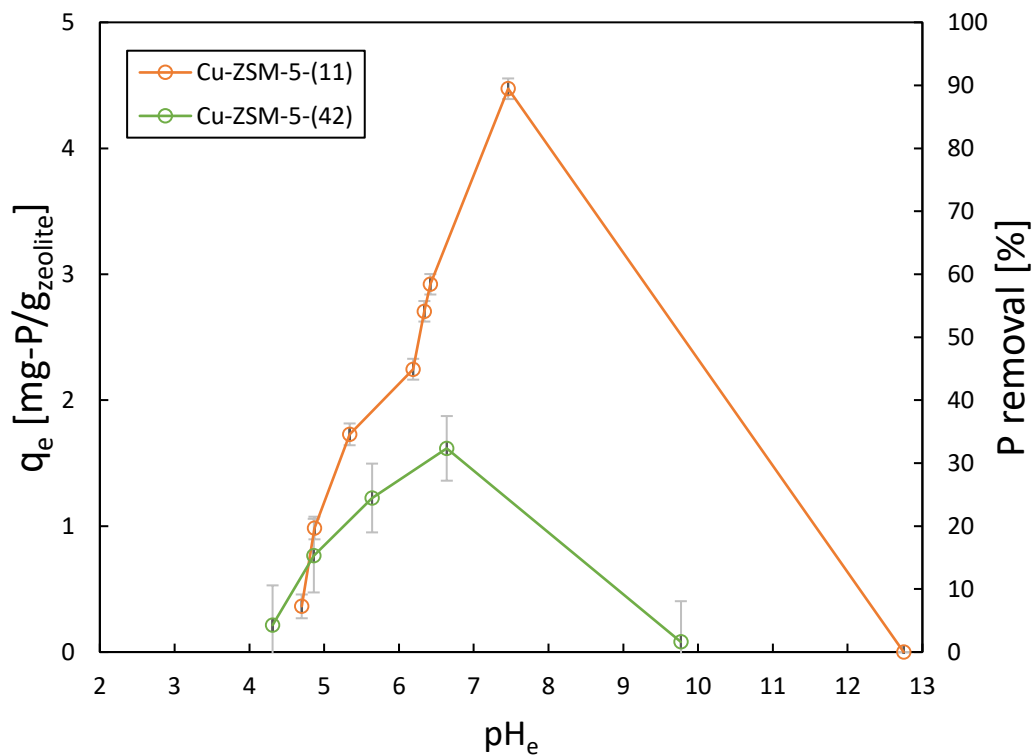


**Figure 4.11** Phosphate adsorption on Cu-ZSM-5 at Si/Al ratios 11 and 42 evaluated as a function of the final solution pH. The experimental conditions and phosphate uptake values are the same as those reported in Figure 4.9.

#### 4.4.4 Copper leaching

Dissolved copper is toxic to a wide range of organisms, especially to aquatic biota including algae, phytoplankton and fish, which can experience mortality at concentrations  $< 1 \mu\text{g/L}$  [104]. Therefore, the post-adsorption solutions of Cu-ZSM-5 were studied for evidence of copper leaching. Owing to the observed behavior, the initial phosphate concentration range was extended up to 1500 mg-P/L; the initial pH was 7 for all solutions to approximate environmental conditions, and all other conditions remained unchanged. The results are displayed in Figure 4.12.

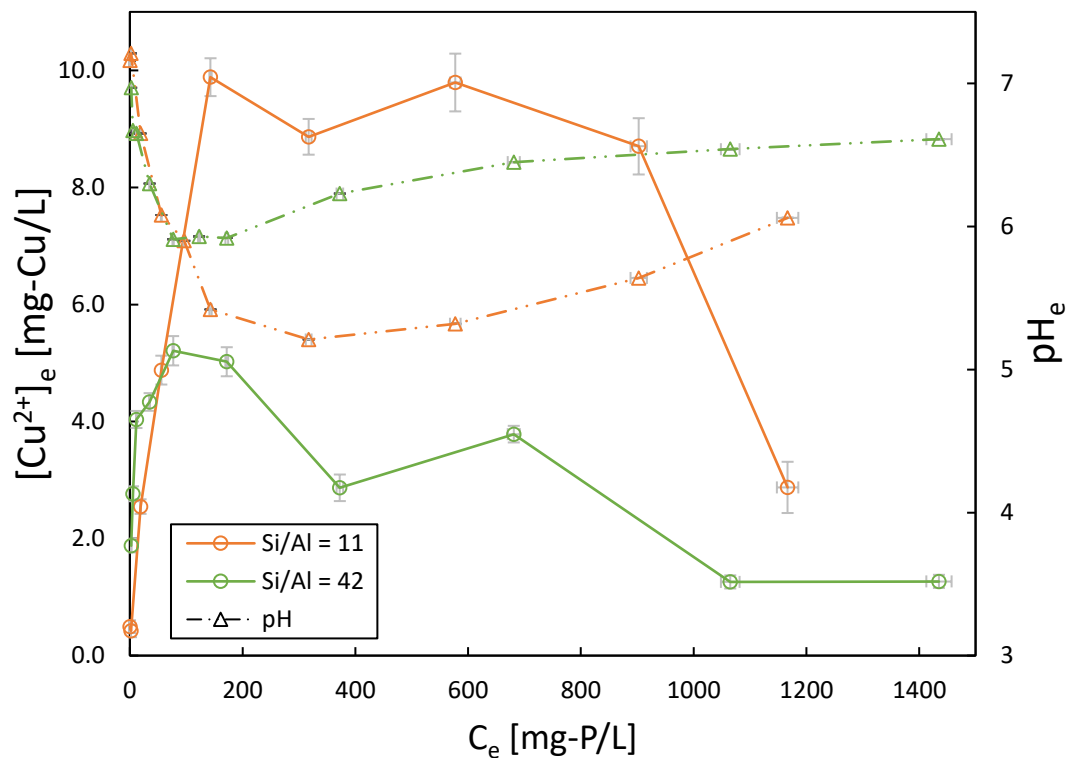


**Figure 4.12** Leaching of copper from Cu-ZSM-5 sorbents into solution due to phosphate adsorption over a range of initial solution phosphate concentrations, up to 1500 mg-P/L. The initial pH was 7 for all cases, and the final equilibrium pH is shown for reference.

Environmentally significant copper concentrations were measured for both Si/Al ratio sorbents over the entire range of initial phosphate concentrations. For data obtained at an initial P concentration of 10 mg-P/L, Cu-ZSM-5-(11) and Cu-ZSM-5-(42) leached  $0.5 \pm 0.1$  mg-Cu/L and  $2.8 \pm 0.1$  mg-Cu/L, respectively. However, the Si/Al = 11 sorbent produced the highest dissolved copper concentration of  $9.9 \pm 0.3$  mg-Cu/L (at initial P concentration of 200 mg-P/L), while Si/Al ratio 42 produced  $5.2 \pm 0.3$  mg-Cu/L (at initial P concentration of 100 mg-P/L). For both sorbents beyond these maximums, higher phosphate concentrations used for the adsorption tests were associated with lower dissolved copper concentrations. The  $pH_e$  data also shown in Figure 4.12 showed an inverse relationship with dissolved copper concentration, and general alignment of the extrema and profiles was observed. This inverse relationship is consistent the well-established role of pH (over this range) on the solubility of copper species [105]. At high P concentrations, the equilibrium pH was observed to revert to neutral initial conditions. This is consistent with the increased buffering capacity of phosphate solutions with higher concentration. The loss of copper relative to the starting contents of the sorbents were approximately 1.3% and 1.9% for Cu-ZSM-5-(11) and Cu-ZSM-5-(42), respectively.

#### **4.5 Linking active sites and structure to phosphate adsorption**

The results presented in section 4.4.3 confirmed that copper species are the active site for phosphate adsorption in Cu-ZSM-5. This finding supports similar conclusions

relating to phosphate recovery by Cu-ZSM-5 previously reported by our research group [74]. Therefore, the phosphate adsorption properties of copper ZSM-5 were further studied with a focus on accounting for variations in copper loading and identifying any remaining activity differences that could provide insight into zeolite or copper site structure.

#### **4.5.1 Adsorption isotherms**

The measured phosphate adsorption isotherm data was normalized by copper content, both on molar and specific bases. In other words, phosphate adsorption was calculated as a P/Cu molar ratio as well as mg-P/g<sub>Cu</sub>. The results are displayed in Figure 4.13.

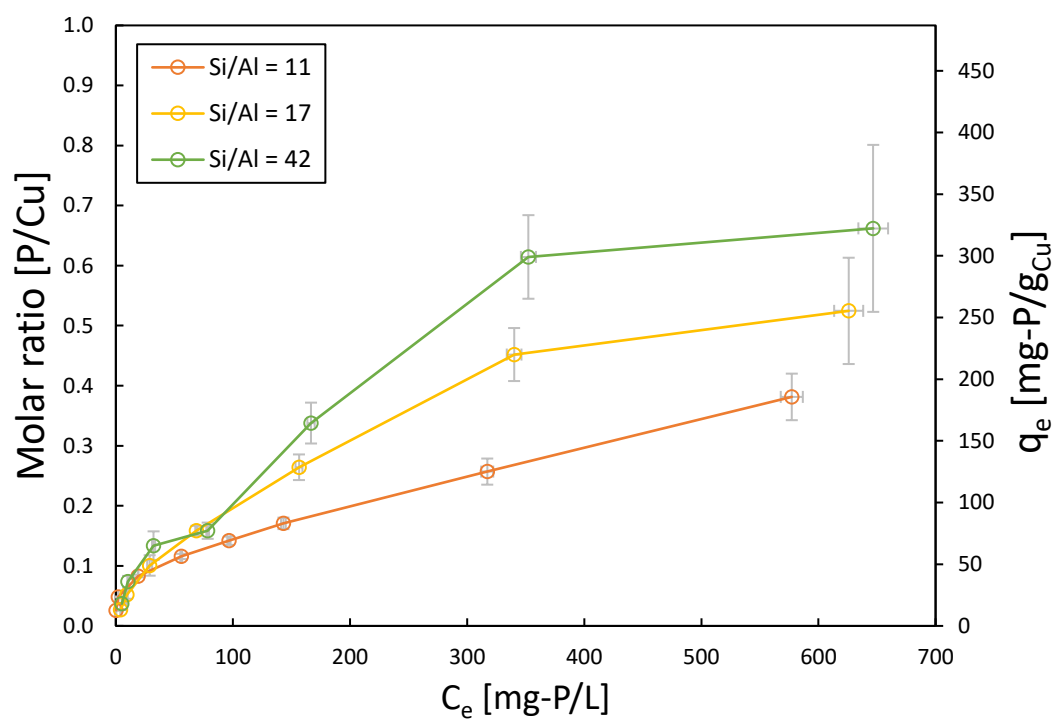


**Figure 4.13** Phosphate adsorption isotherms for Cu-ZSM-5 at  $20 \pm 2$  °C and neutral pH, normalized by copper content. The sorbent loading was  $20 \text{ g}_{\text{zeolite}}/\text{L}$ . The horizontal axis,  $C_e$ , represents the equilibrium concentration.

## RESULTS

The copper-normalized phosphate adsorption isotherms revealed different phosphate adsorption trends to the isotherms without normalization discussed in section 4.4.2. Here, the magnitude of phosphate adsorption at  $C_e > 50$  mg-P/L was clearly lowest for Cu-ZSM-5-(11), whereas it was greatest across the entire measured concentration range for the data without normalization. Below an equilibrium phosphate concentration of  $\sim 50$  mg-P/L, all three Si/Al ratio copper-exchanged zeolites showed similar (i.e., within 0.05 P/Cu units or 25 mg-P/g<sub>Cu</sub>) normalized phosphate adsorption behavior. However, above this concentration, the isotherms deviated. The normalized data revealed a P/Cu molar ratio of less than 1 for all copper-exchanged zeolites studied, with a maximum of 0.66 represented by Cu-ZSM-5-(42).

The normalized adsorption isotherm data was fitted to Langmuir and Freundlich models as previously described in section 4.4.2. The results and  $\chi^2$  values for the regressions are presented in Table 4.3. According to the  $\chi^2$  metric, the empirical Freundlich adsorption isotherm model provided a better fit to the experimental adsorption data for Cu-ZSM-5 across all Si/Al ratios. Figure 4.14 illustrates the adsorption isotherm data fitted to the both models. The Freundlich intensity parameter,  $1/n$ , was less than 1 indicating favorable adsorption. The values matched those obtained without normalization by copper content; Cu-ZSM-5-(11) featured the lowest intensity parameter (most favorable adsorption or highest degree of surface adsorption site heterogeneity), followed by Si/Al ratio 17 and then 42. In contrast, a higher magnitude

## RESULTS

of adsorption—represented by the Freundlich constant,  $K_F$ , and the Langmuir maximum adsorption capacity,  $Q_{\max}^0$ —was observed with higher Si/Al ratio despite the decreasing trend in degree of favorable adsorption suggested by  $1/n$ . The increasing trend for  $K_F$  and  $Q_{\max}^0$  was in contrast to the decreasing trend observed for the data without normalization.



**Table 4.3** Langmuir and Freundlich isotherm parameters obtained by non-linear regression for adsorption of phosphate by Cu-ZSM-5, normalized by copper content.

Si/Al	Langmuir			Freundlich		
	$Q_{\max}^0$ (mg-P/g <sub>Cu</sub> )	$K_L$ (L/mg-P)	$\chi^2$	1/n	$K_F$ (mg-P/g <sub>Cu</sub> )(L/mg-P) <sup>1/n</sup>	$\chi^2$
11	252.0	0.0039	796.1	0.49	7.69	34.74
17	357.7	0.0042	23.6	0.53	8.92	6.88
42	492.2	0.0034	51.4	0.56	9.58	22.41

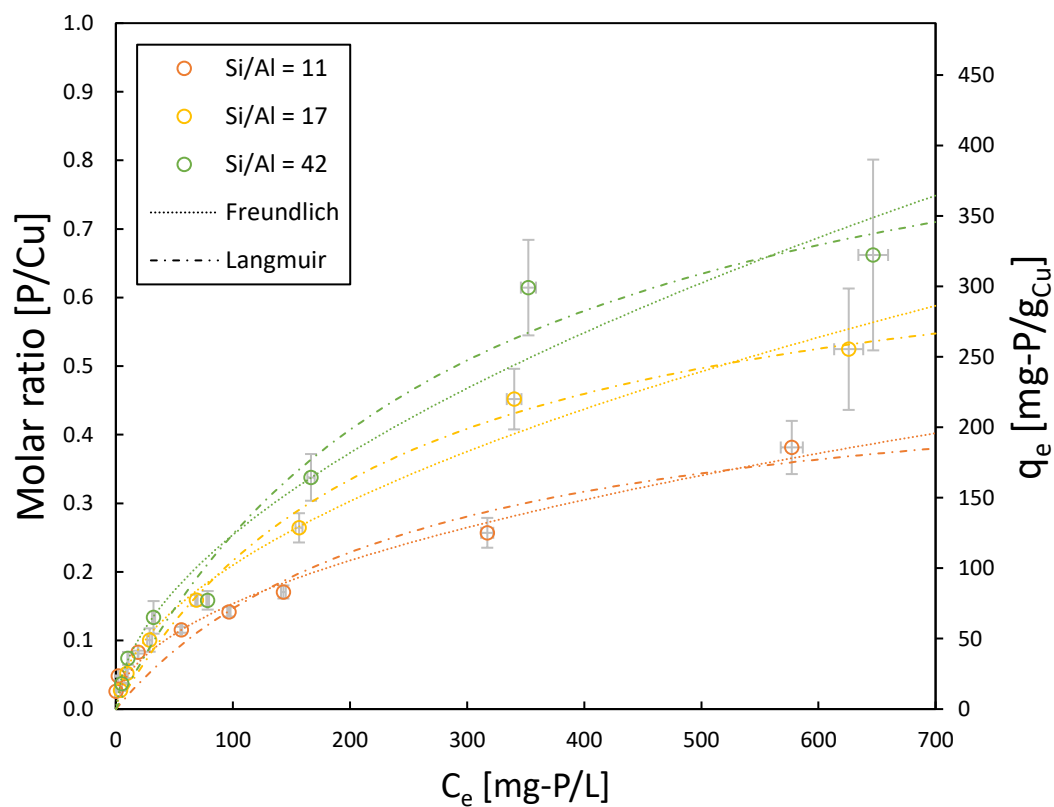


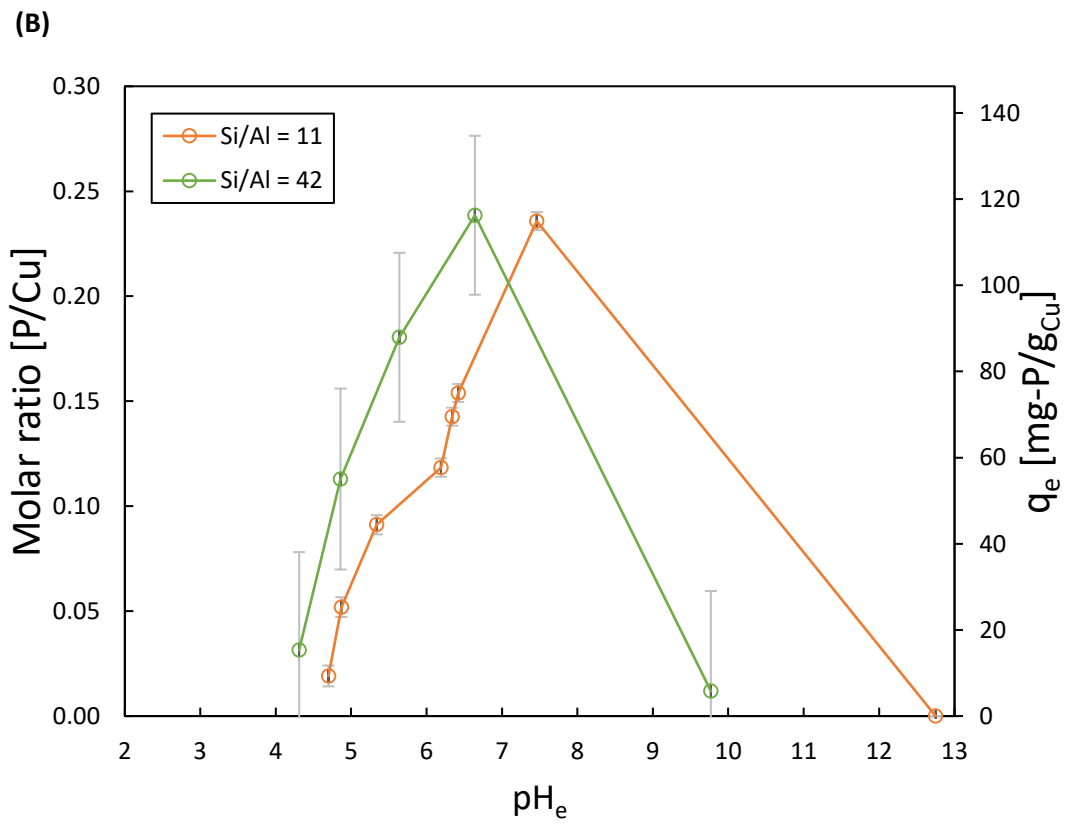
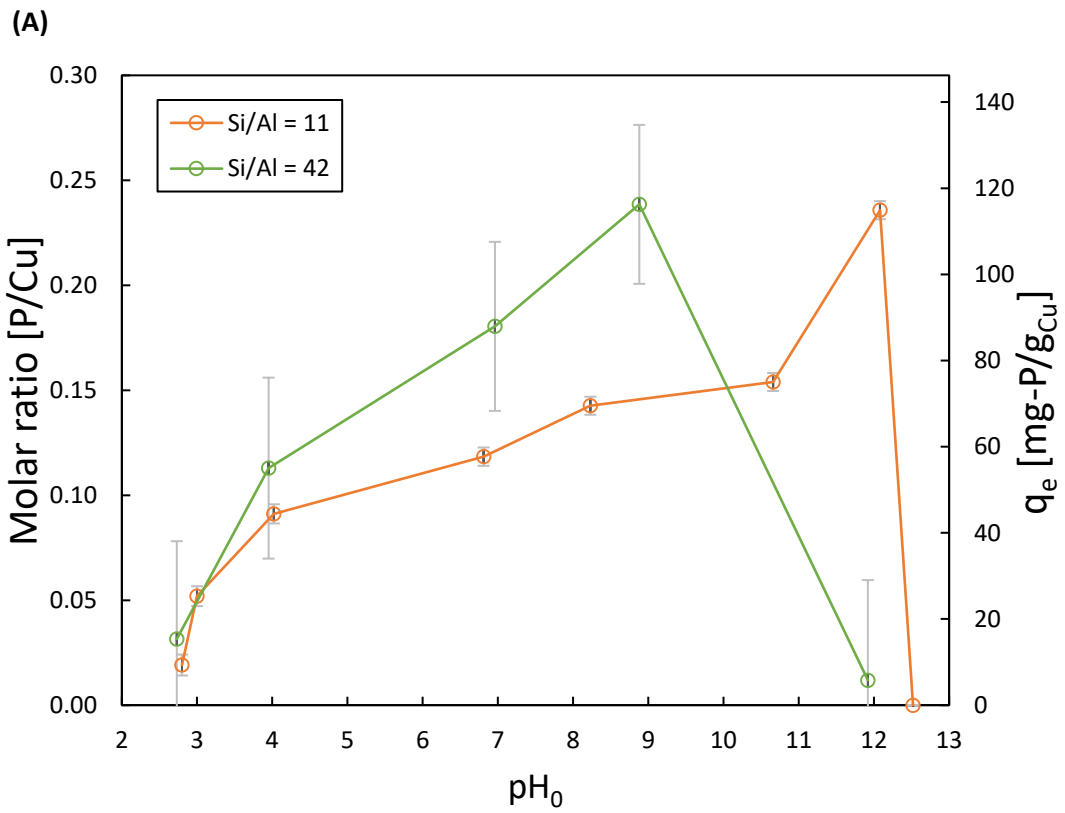
**Figure 4.14** Equilibrium phosphate adsorption isotherm data for Cu-ZSM-5 fitted to the Freundlich and Langmuir models by non-linear least squares regression. The initial pH of the solution was 7.

### 4.5.2 Effect of pH

The pH of the phosphate solution impacted the phosphate adsorption capacity of Cu-ZSM-5, as demonstrated in section 4.4.3. This effect was further considered in light of the different copper loadings in the copper ZSM-5 materials. The results are illustrated in Figure 4.15.

The results show that Cu-ZSM-5-(42) exhibited a higher copper-normalized phosphate adsorption capacity than Cu-ZSM-5-(11) over a wide range of initial pH values. At initial pH  $\sim 3$ , the difference was negligible, but increased with increasing pH. However, when considering the equilibrium pH, Cu-ZSM-5-(42) demonstrated consistently higher copper-normalized phosphate adsorption over the active range. The magnitude of this difference was approximately constant at  $\sim 0.05$  P/Cu or  $\sim 25$  mg-P/g<sub>Cu</sub>; this is also reflected in Figure 4.15B by similar slopes for both Si/Al ratio materials. Therefore, the pH effect did not account for the superior copper-normalized phosphate adsorption observed for Cu-ZSM-5 with higher Si/Al ratio.

**Figure 4.15** Effect of pH (A: initial, B: equilibrium) on phosphate adsorption for Cu-ZSM-5, normalized by copper content. Initial concentration was 100 mg-P/L.



### 4.5.3 Adsorption kinetics

Adsorption kinetic data was collected at  $20 \pm 2$  °C, initial pH of 7 and initial phosphate concentration of 10 mg-P/L. To obtain kinetic parameters, the copper-normalized data was fitted to the pseudo first order and pseudo second order adsorption kinetic models, shown in equations 5 and 6, respectively [106], [107]. The parameters were obtained by non-linear regression. The results and  $\chi^2$  values for the regressions are presented in Table 4.4.

$$q_t = q_e(1 - e^{-k_1 t}) \left[ \frac{mg-P}{g} \right] \quad (\text{Equation 5})$$

$$q_t = \frac{q_e^2 k_2 t}{1 + q_e k_2 t} \left[ \frac{mg-P}{g} \right] \quad (\text{Equation 6})$$

According to the  $\chi^2$  metric, the pseudo second order kinetic model provided a better fit to the experimental adsorption data for Cu-ZSM-5 across all Si/Al ratios. Figure 4.16 illustrates the adsorption kinetic data fitted to both models and highlights the superior fit obtained for the pseudo second order model. The copper-normalized equilibrium adsorption parameter,  $q_e$ , increased with increasing Si/Al ratio; this is consistent with the general trends in equilibrium adsorption observed in the isotherm data. In contrast, the kinetic rate constant decreased with increasing Si/Al ratio.

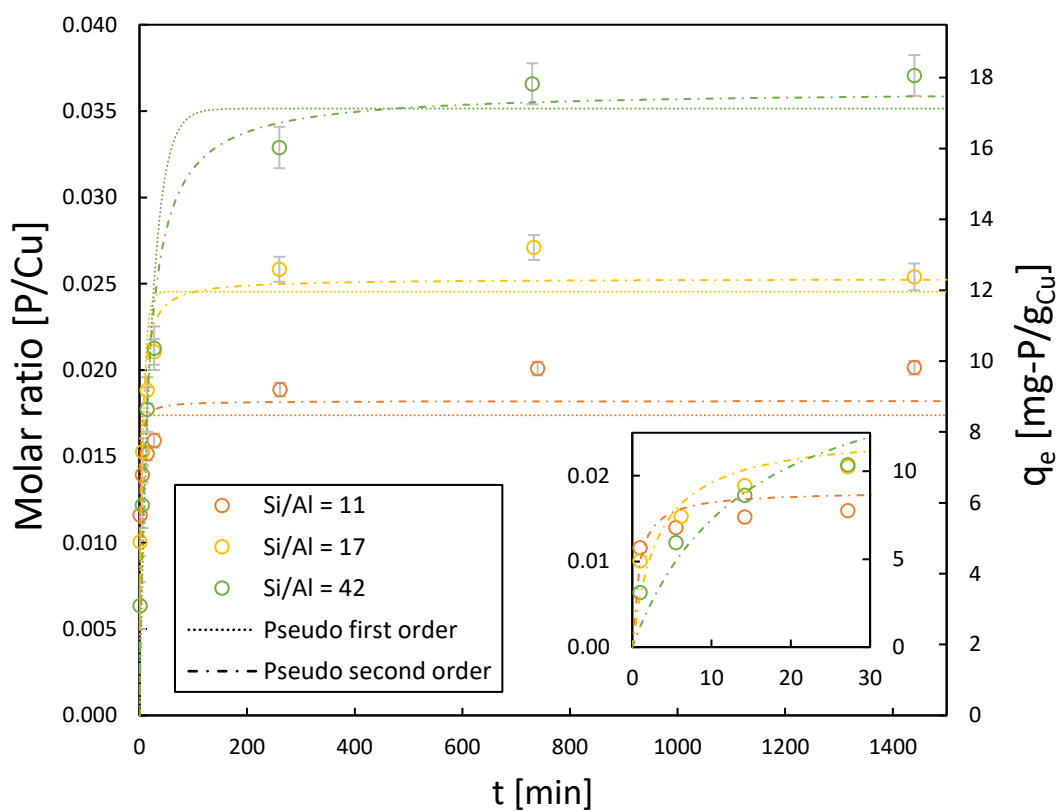
**Table 4.4** Pseudo first order and pseudo second order kinetic model parameters obtained by non-linear regression for adsorption of phosphate by Cu-ZSM-5, normalized by copper content.

Si/Al	Pseudo first order			Pseudo second order		
	$q_e$ (mg-P/g <sub>Cu</sub> )	$k_1$ (1/min)	$\chi^2$	$q_e$ (mg-P/g <sub>Cu</sub> )	$k_2$ (g <sub>Cu</sub> /mg-P·min)	$\chi^2$
11	8.5	1.08	1.0	8.9	0.14	0.6
17	12.0	0.16	6.5	12.3	0.026	1.6
42	17.1	0.046	8.7	17.6	0.0040	3.7

Although the pseudo second order model provided a reasonable fit to the experimental data, it does not generally reveal any mechanistic insight; the same applies to the pseudo first order model [63]. Therefore, to further analyze the kinetics of phosphate adsorption by Cu-ZSM-5 with potential for mechanistic insight, the kinetic data was plotted with  $t^{1/2}$  as the abscissa per the linearized form of the intra-particle diffusion model, shown in equation 7 [65]. The results are shown in Figure 4.17.

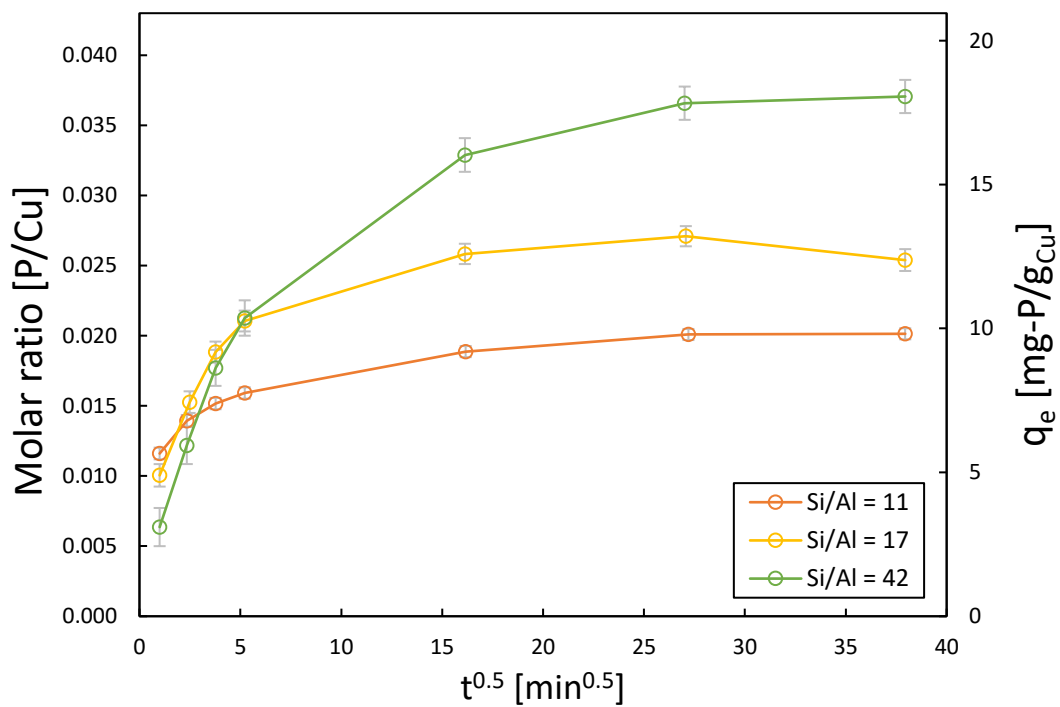
$$q_t = k_p \sqrt{t} + c \left[ \frac{mg-P}{g} \right] \quad (\text{Equation 7})$$

Figure 4.17 reveals that none of the Si/Al ratio copper-exchanged ZSM-5 materials exhibited a linear relationship between phosphate adsorption and  $t^{1/2}$ . Rather, steep initial slopes flattened as  $t^{1/2}$  increased. The longest initial, near-linear regime was demonstrated by Si/Al ratio 42 (up to  $\sim 5 \text{ min}^{1/2}$ ), followed by 17 (up to  $\sim 4 \text{ min}^{1/2}$ ) then 11 (less than  $2.5 \text{ min}^{1/2}$ ). The observed changes in slope are indicative of a multi-step adsorption process [63]. Therefore, intra-particle diffusion was not solely responsible for phosphate adsorption in copper-exchanged ZSM-5. By inspection, the apparent vertical axis intercepts were all positive, with the highest for Cu-ZSM-5-(11), followed by Si/Al ratio 17 and 42. Therefore, Si/Al ratio 11 featured the strongest initial adsorption behavior, and Si/Al ratio 42 the least [64].



**Figure 4.16** Phosphate adsorption data for Cu-ZSM-5 fitted to kinetic models by non-linear least squares regression, normalized by copper content. The initial phosphate concentration was 10 mg-P/L. Inset is data from 0 to 30 min.





**Figure 4.17** Phosphate adsorption data for Cu-ZSM-5, normalized by copper content, with  $t^{1/2}$  as the abscissa for evaluation of the intra-particle diffusion kinetic model.

#### 4.5.4 Adsorption properties and active site structure

The Si/Al ratio is an important structural parameter of copper-exchanged ZSM-5, as it directly impacts the number of available framework Al sites facilitating copper loading onto ZSM-5 through ion exchange with extra-framework cations. It follows that the average distance between copper sites—assuming a completely homogenous distribution of Al and Cu sites—should increase with Si/Al ratio. Figure 4.18 shows the relationship between the Si/Al ratio and both Cu site density and average Cu···Cu distance calculated for all copper-exchanged ZSM-5 materials synthesized (previously reported in Table 4.1). The results show that Cu site density decreased with increasing Si/Al ratio, as expected. The dependence was non-linear. The average Cu···Cu distance increased with increasing Si/Al ratio, as expected. However, the dependence in this case had a stronger linear character. The observed increase in linear dependence in going from Cu density to average Cu···Cu distance is consistent with the calculation methodology; the distance was calculated (in part) by taking the cubed root of the reciprocal of density.

Of particular interest in the study of Cu-ZSM-5 structure-property relationships is the speciation of Cu in the exchanged zeolites. Specifically, the relative abundance of [Cu–O–Cu]<sup>2+</sup> dimer species vs. isolated Cu<sup>2+</sup> monomers;  $\eta_{\text{Cu}\cdots\text{Cu}}$  is used here to denote the fraction of all copper sites present in dimeric form. The phosphate adsorption properties

of Cu-ZSM-5 at Si/Al ratios 11, 17 and 42 were regressed against the Cu density. The results presented in Figure 4.18 illustrate a strong correlation between equilibrium phosphate adsorption properties and the Cu density in Cu-ZSM-5. The strongest linear correlation was demonstrated by the Freundlich constant,  $K_f$ , with an  $R^2$  value of 0.999 and negative slope. This correlation suggests the magnitude of phosphate adsorption decreases with increasing Cu density. Similarly, the Langmuir maximum adsorption parameter,  $Q_{\max}^0$ , also followed a negative linear correlation with a reasonably strong  $R^2$  value of 0.92. The Freundlich intensity parameter,  $1/n$ , followed a negative linear correlation with an  $R^2$  value of 0.98. Therefore, higher Cu site densities are correlated with more favorable adsorption or higher degrees of surface adsorption site heterogeneity. No consistent trend was observed for the Langmuir constant,  $K_L$ .

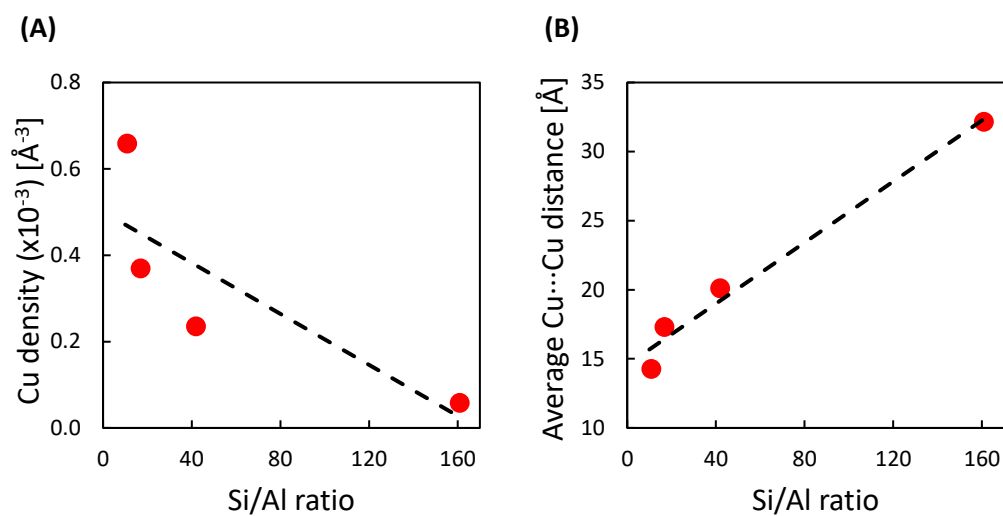


**Figure 4.18** Characterization of Cu sites in copper-exchanged ZSM-5. (A) Dependence of Cu density on the Si/Al ratio. (B) Dependence of average Cu...Cu distance on Si/Al ratio.

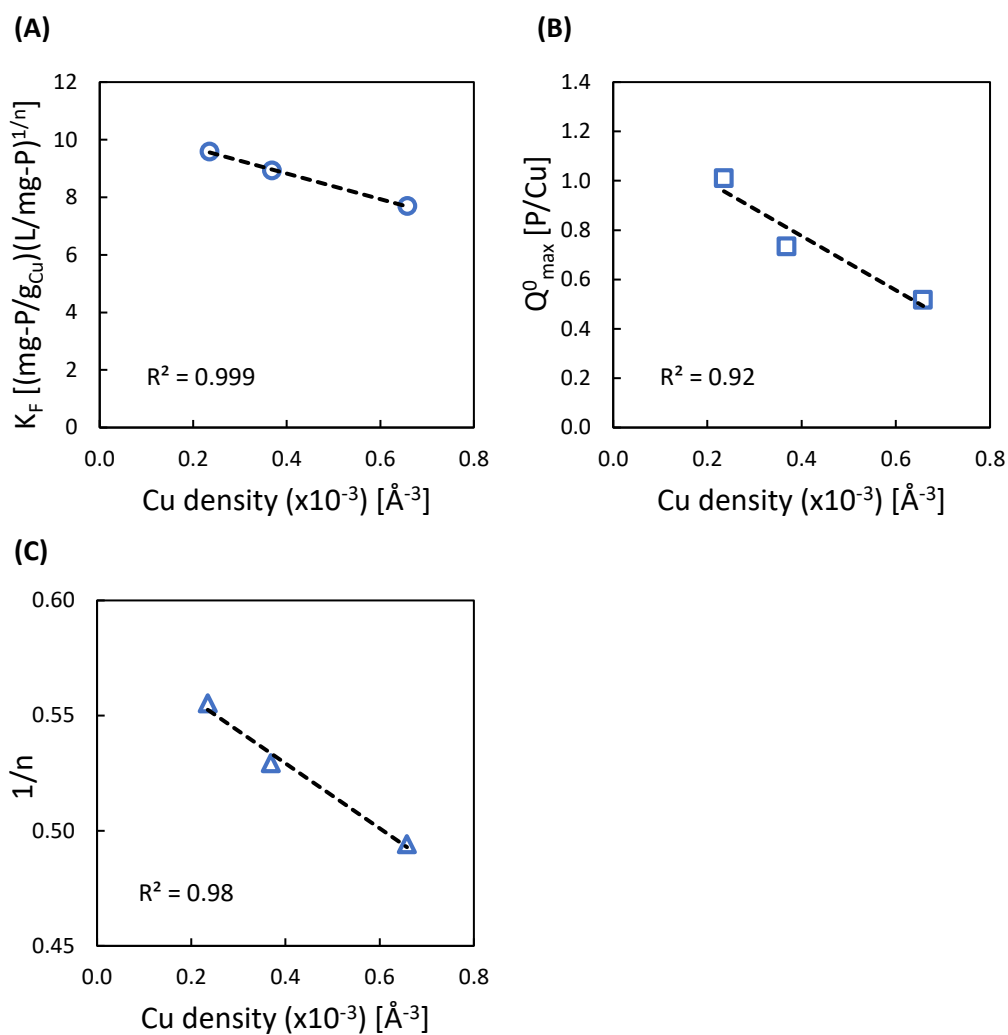


**Figure 4.19** Dependence of equilibrium phosphate adsorption properties at tested conditions on Cu density. (A) Dependence of the Freundlich constant on site density, (B) Dependence of the Langmuir maximum adsorption constant on site density, (C) Dependence of the Freundlich intensity parameter on site density.

The data presented in Figure 4.19A indicated that  $K_f$  decreased with increasing Cu density, and the same trend held for  $Q_{\max}^0$  data shown in Figure 4.19B. Unlike  $Q_{\max}^0$ ,  $K_f$  does not indicate a maximum adsorption but is rather the constant of proportionality that indicates the magnitude of adsorption. Therefore, despite the slightly poorer fit of the Langmuir model to the experimental isotherm data,  $Q_{\max}^0$  is still useful in providing information on the maximum saturated monolayer adsorption capacity of the Cu-ZSM-5 material. In units of P/Cu, the  $Q_{\max}^0$  parameter was 1.0 for the lowest Cu density, but only 0.52 for the highest site density. Given the obtained  $Q_{\max}^0$  values are  $\sim 1$  or lower, the adsorption of phosphate on Cu sites appeared to be monolayer in nature for the conditions studied here. However, neither  $K_f$  nor  $Q_{\max}^0$ —both of which are based on phosphate adsorption normalized by total copper content—considered the adsorption capacity of copper dimer sites compared to monomeric sites in the Cu-ZSM-5 materials tested. This may explain the somewhat unexpected trend in phosphate adsorption magnitude observed with respect to Cu density. Given the dimer is a copper oxocation of the form  $[\text{Cu}-\text{O}-\text{Cu}]^{2+}$ , it's reasonable to suggest that this structure has a reduced phosphate adsorption capacity, per Cu ion, compared to monomeric  $\text{Cu}^{2+}$  sites. To correct the capacity or magnitude-related parameter for this difference, a simple division by  $\delta \cdot \eta_{\text{Cu}\cdots\text{Cu}} + (1 - \eta_{\text{Cu}\cdots\text{Cu}})$  could be applied, where  $\delta$  is the number of phosphate anions a dimer site can host—per Cu ion—relative to a monomeric site. It's proposed here that dimer  $[\text{Cu}-\text{O}-\text{Cu}]^{2+}$  sites have an equilibrium capacity equal to the equilibrium capacity of monomeric  $\text{Cu}^{2+}$  sites (i.e.,  $\delta = 0.5$ ) at the low phosphate

concentrations and conditions utilized in this study. Detailed arguments justifying this assumption have been presented in the discussion.

Based on  $\delta = 0.5$ , the dimer fractions for each point in the data set were calculated by independently minimizing the sum of the absolute differences among  $K_f$  and  $Q_{\max}^0$  values normalized by  $\delta \cdot \eta_{\text{Cu}\cdots\text{Cu}} + (1 - \eta_{\text{Cu}\cdots\text{Cu}})$ . The constraints applied in solving this non-linear set of equations and the parameters after the attempted equalization are presented in Figure 4.20. The calculated values for  $\eta_{\text{Cu}\cdots\text{Cu}}$  based on both the Freundlich model's magnitude-related parameter,  $K_f$ , and the Langmuir model's  $Q_{\max}^0$  parameter are shown as a function of the Cu density in Figure 4.21A.

The estimates for  $\eta_{\text{Cu}\cdots\text{Cu}}$  derived from equalization of the Langmuir maximum adsorption constants were consistently higher than those derived from the equalization of the Freundlich constants. Based on the Langmuir model's  $Q_{\max}^0$  parameter, the estimated dimer fractions for Cu-ZSM-5-(11), Cu-ZSM-5-(17) and Cu-ZSM-5-(42) were ~100%, 71% and 28%, respectively, while based on the Freundlich model's parameter  $K_f$  parameter, the fractions were ~55%, 32% and 19%, respectively. The linear scaling relationship with Cu density was ~1.6 and 0.84 for the Langmuir and Freundlich estimations, respectively. Based on the average of both models, the estimated dimer fractions for Cu-ZSM-5-(11), Cu-ZSM-5-(17) and Cu-ZSM-5-(42) were ~77%, 51% and 24%, respectively, while the linear scaling relationship with Cu

density was  $\sim 1.2$ . As highlighted in Figure 4.21A, the estimates calculated based on phosphate anion adsorption and derived from  $Q_{\max}^0$  were generally consistent with those calculated from TPR measurements by our group for Cu-ZSM-5 at full exchange [95]; the TPR profiles for this data are shown in Figure 4.22. In that work by Xie *et al.*, the linear scaling relationship was estimated to be  $\sim 1.4$ , which is similar to the  $\sim 1.6$  slope reported here. Additionally, there is some agreement with the dimer estimates previously calculated from CO-TPR measurements by Da Costa *et al.* [42]. However, in that study the Si/Al ratio was generally held constant, while the level of exchange was varied leading to a broader range of Cu/Al ratios than those used in this work.



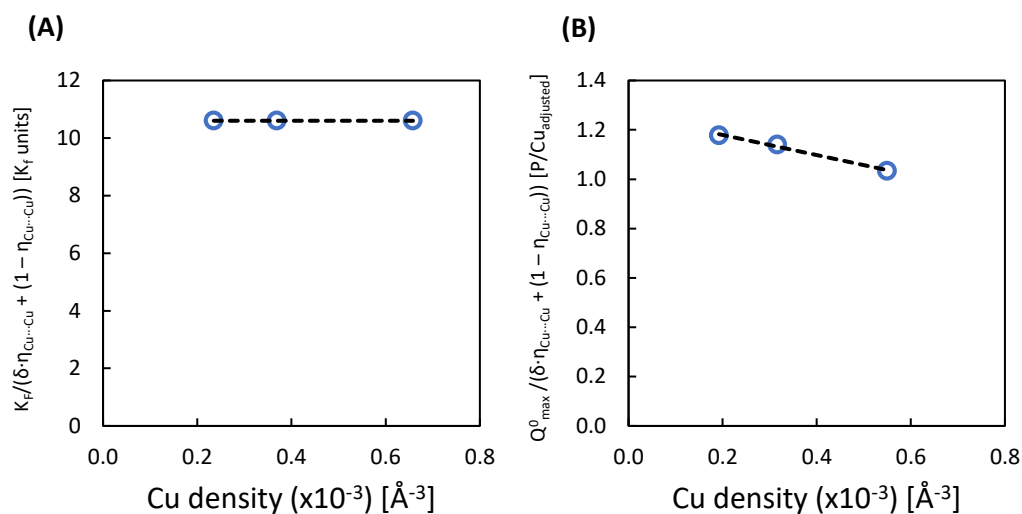


**Figure 4.20** Equilibrium phosphate adsorption parameters equalized by  $\delta \cdot \eta_{\text{Cu}\cdots\text{Cu}} + (1 - \eta_{\text{Cu}\cdots\text{Cu}})$ , where  $\eta_{\text{Cu}\cdots\text{Cu}}$  was varied to achieve minimum sum of the squared differences and  $\delta$  was taken as 0.5 (i.e., number of phosphate anions a dimer site can host—per Cu ion—relative to a monomeric site). The equalization was subject to the following constraints:  $0 \leq \eta_{\text{Cu}\cdots\text{Cu}} \leq 1$ , line of best fit for  $\eta_{\text{Cu}\cdots\text{Cu}}$  vs. Cu density must pass through the origin. (A) Equalization of Freundlich constants, (B) Equalization of Langmuir maximum adsorption constants, presented in P/Cu<sub>adjusted</sub> units (i.e., units accounting for the reduced host capacity of Cu in the dimer fraction).  $Q_{\text{max}}^0 \sim 1$  indicates adsorption was near monolayer in nature.

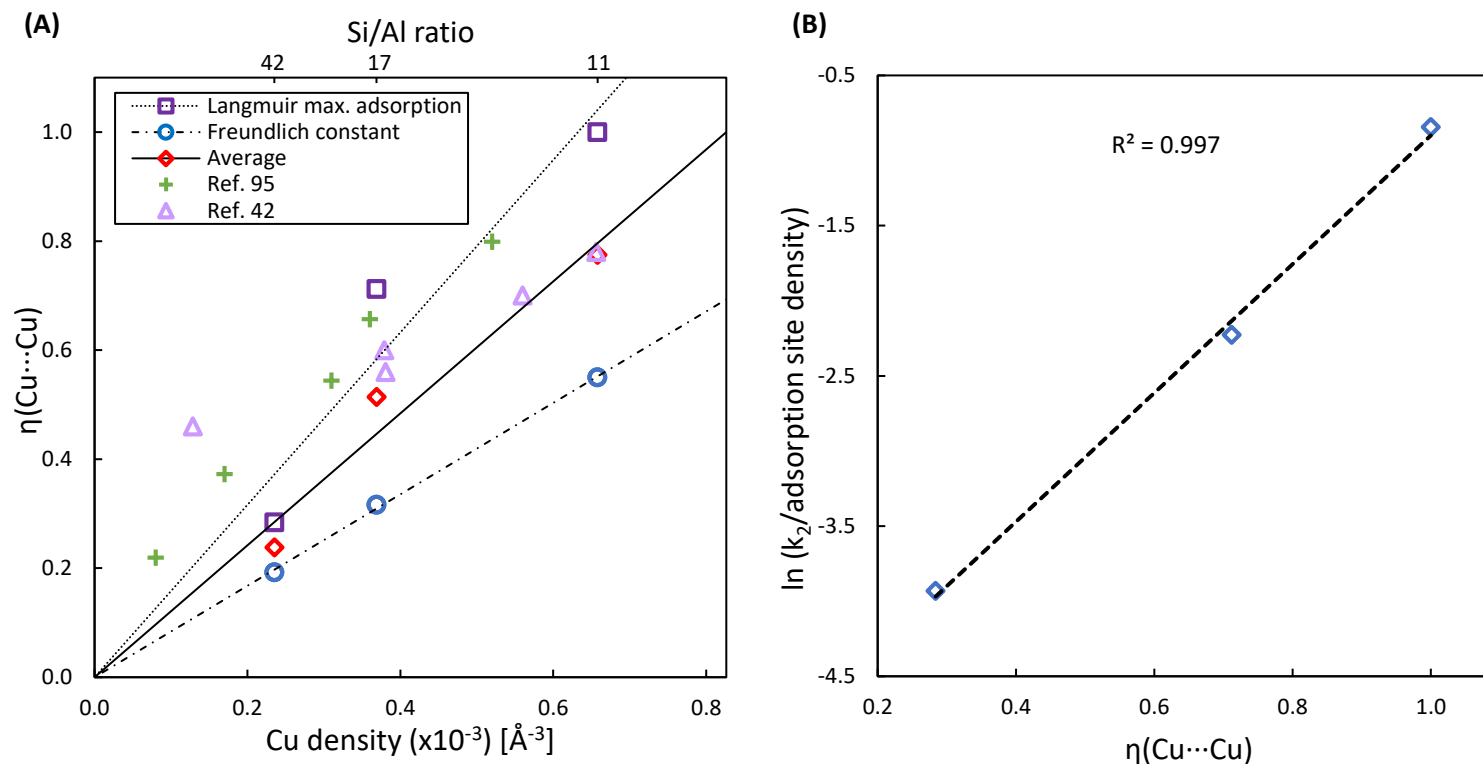


**Figure 4.21** Copper dimer fraction derived from equilibrium phosphate adsorption and applied to kinetic data. (A) Cu dimer fraction,  $\eta_{\text{Cu}\cdots\text{Cu}}$ , estimated from equilibrium adsorption isotherm constants,  $Q_{\text{max}}^0$  (purple  $\square$ ),  $K_f$  (blue  $\circ$ ) (corresponding to the magnitude of the adsorption capacity in the Langmuir and Freundlich models, respectively) and averages (red  $\diamond$ ) as a function of the Cu density. Our estimates for the Cu dimer fraction using liquid phase phosphate anion adsorption were generally consistent with TPR experimental data from references 95 (green  $+$ ) and 42 (pink  $\triangle$ ), (B) Dependence of the pseudo second order rate constant on copper dimer fraction.  $\ln(k_2/\text{adsorption site density})$  is referred to as  $\ln k_2^*$  in the text.

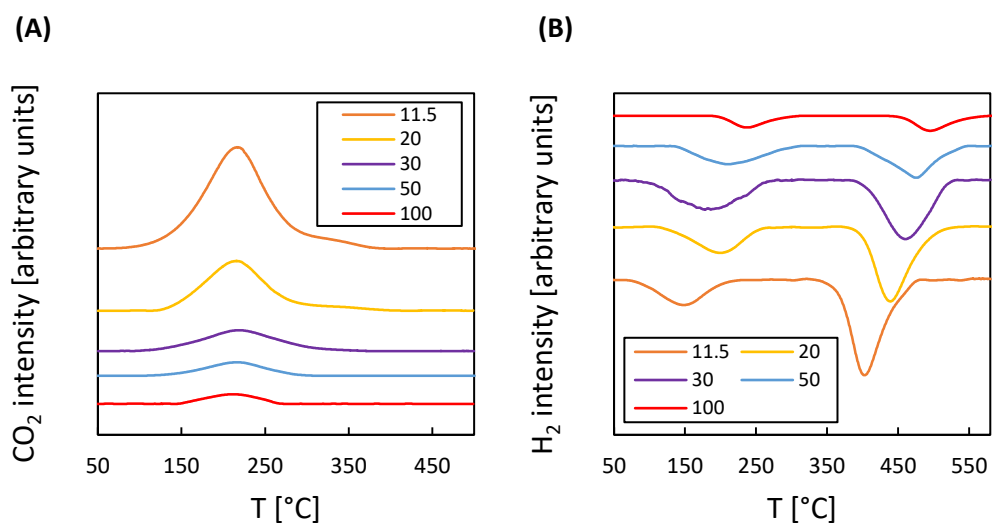


**Figure 4.22** TPR profiles for five Cu-ZSM-5 zeolites at full exchange referenced in Figure 4.21. Source data provided by Xie *et al.* [95]. The legends refer to the Si/Al ratio of the zeolite. (A) CO-TPR profile, (B) H<sub>2</sub>-TPR profile.

The results of the kinetic modeling were evaluated in the context of the estimated dimer fractions by regressing the pseudo second order rate constant,  $\ln k_2^*$ , against the  $\eta_{\text{Cu}\cdots\text{Cu}}$  derived from  $Q_{\text{max}}^0$ . Note here that in the text  $k_2^*$  refers to the rate constant normalized by the adsorption site density (i.e., Cu density \*  $(\delta \cdot \eta_{\text{Cu}\cdots\text{Cu}} + (1 - \eta_{\text{Cu}\cdots\text{Cu}}))$ ), which assumes the phosphate anion sticking probability is directly proportional to the concentration of adsorption sites. The results in Figure 4.21B show a positive linear correlation with dimer fraction, with an  $R^2$  value of close to 1 indicating a strong linear fit for the kinetic parameter. Going from the lowest dimer fraction to the highest (i.e., Si/Al ratio 42 to 11) the  $\ln k_2^*$  parameter showed relative changes of 65%, or  $\sim 3500\%$  if  $k_2^*$  is considered rather than the natural logarithm. Therefore, phosphate adsorption kinetics showed great sensitivity to changes in dimer fraction. This indicates that the kinetic rate constant could serve as a sensitive tool for probing changes in the Cu dimer fraction within Cu-ZSM-5 under controlled phosphate adsorption conditions.

## **Chapter 5 Discussion**

### **5.1 Introduction**

This chapter discusses the results presented in Chapter 4 and their broader implications in the context of the stated objectives of the thesis. First, the extent to which copper ZSM-5 may represent a viable sorbent material for dissolved inorganic P will be considered. Then, the discussion will focus on the relationship between phosphate anion adsorption properties and material structure. This will lead to an evaluation of the potential for liquid phase anion adsorption to be used as a probe for quantifying copper dimers and—more broadly—as a new and unique direction for characterizing heterogenous catalysts.

### **5.2 Copper ZSM-5 as a sorbent for inorganic dissolved P**

From the perspective of the removal of inorganic dissolved P from environmental or waste-water streams, Cu-ZSM-5 displayed strong potential for P removal at the tested conditions. The best performing material tested, Cu-ZSM-5-(11), showed a removal of ~76% at pH 7 and initial concentration of 10 mg-P/L. In addition, kinetic behavior was reasonably fast, with near-equilibrium removal reached after ~2 hours, which is in

general agreement with the work of Manto *et al.* [74]. However, given the solution conditions of this study were synthetic, they represent performance in a best-case scenario; it is likely that removal from real-world samples would be lower, as reported by others [74]. Additionally, the high sorbent loading—20 g/L used here, up to 50 g/L by Manto *et al.*—implies a general inefficiency of the material owing to a low concentration of active sites, with copper content generally less than 4.0 %w/w. Therefore, low manufacturing costs—or recovery and regeneration of the sorbents, already studied elsewhere [74]—would be a necessity for more practical applications.

An important focus of this work that was not previously investigated is the impact of Si/Al ratio on the phosphate uptake. The results showed that regardless of any heterogeneity in Cu sites, the decreased copper loading in ZSM-5 with higher Si/Al ratios resulted in a net decrease in phosphate uptake. This was established not only by the kinetic profile shown in Figure 4.6, but by the adsorption isotherms measured and reported in section 4.4.2 across a wide range of phosphate concentrations. The maximum adsorption capacity,  $Q_{\max}^0$  (assuming Langmuir behavior) decreased from 9.8 mg-P/g<sub>zeolite</sub> to 6.8 mg-P/g<sub>zeolite</sub> going from Si/Al 11 to 42. This lends further support to the established conclusion that copper is the active site for phosphate anion adsorption on Cu-ZSM-5. Indeed, for Cu-ZSM-5-(161)—featuring a copper loading of only 54  $\mu\text{mol/g}_{\text{zeolite}}$  vs. 219  $\mu\text{mol/g}_{\text{zeolite}}$  for Cu-ZSM-5-(42)—no phosphate adsorption

was detectible. However, it cannot be ruled out that a kinetic effect, rather than equilibrium considerations, was responsible for this observation.

The pH had a significant impact on phosphate adsorption capacity, and the results presented in this work are a significant contribution in that regard. Solution pH is a critical parameter in environmental water bodies and waste-water treatment systems. Therefore, to only study adsorption uptake at a single pH value—especially at non-neutral conditions [74]—significantly limits the applicability and comparability of reported data. The results showed that adsorption capacity for Cu-ZSM-5 increased with increasing initial pH, but was zero for Na-ZSM-5 across the entire pH range. This provided further evidence of the active role of extra-framework copper in phosphate adsorption. At extremes of alkaline pH, it's likely that attack of the Si-O bonds and damage to the zeolite framework in general led to the complete loss of phosphate adsorption activity. The observed increasing trend in pH is in contrast with most sorbent materials (e.g., metal hydr(oxides), organic materials), where increasing pH tends to result in lower phosphate adsorption [25], [27], [28], [30], [108], [109]. The general reasoning presented is that as pH increases, the sorbent surface becomes more negatively charged or there is a higher concentration of competing  $\text{OH}^-$ , which are both unfavorable for anion adsorption. However, orthophosphate deprotonates with increasing pH (at neutral pH, there are approximately equimolar concentrations of  $\text{H}_2\text{PO}_4^-$  and  $\text{HPO}_4^{2-}$ ), which would appear to be favorable for electrostatic interactions

between positively charged copper sites and negatively charged phosphate anions with increasing valence (i.e., outer-sphere adsorption). Therefore, the pH data for Cu-ZSM-5 tends to suggest that either the latter effect dominates the former, or another adsorption mechanism is responsible.

The copper leaching results represent a limitation of the copper ZSM-5 material as a practical sorbent for inorganic dissolved P. Given the measurement of parts-per-million range copper concentrations in the post adsorption liquor, it's unlikely the effluent could be discharged directly into environmental systems without negative consequences for nearby aquatic life [104]. The Cu-ZSM-5 material may be more suitable for industrial or municipal waste-water treatment where processes and equipment already exist to reduce or control the final copper concentration. However, it may be a challenge to convince practitioners to trade one pollutant for another in the absence of a thorough cost-benefit analysis. Comparatively, the loss of copper from the sorbents themselves may be less of a concern, with the reported figures being less than 2% for an initial pass; these losses are similar to those previously reported by Manto *et al.* [74].

### **5.3 Adsorption isotherms and kinetic behavior**

While copper-normalized adsorption data may be of limited interest in terms of the performance of Cu-ZSM-5 as a sorbent for inorganic dissolved P, such data provides



the necessary information required to investigate the nature of the active sites. The normalized adsorption isotherms showed that the P/Cu ratio was less than one, suggesting that multi-layer adsorption is unlikely for this system. Although the isotherms of different Si/Al ratio materials deviated at higher concentrations, it is interesting to note the general agreement where  $C_e < \sim 50$  mg-P/L. This is potentially indicative of heterogeneity in Cu adsorption sites: at low enough concentrations, a certain number of most energetically favorable sites available in all three zeolites can adsorb phosphate similarly; at higher concentrations, these sites become exhausted and others become more important. Therefore, differences in the relative proportions of active site types lead to different adsorption isotherm behavior as concentrations increase, which is in qualitative agreement with the observed adsorption isotherms. Supporting this argument is the superior fit of the Freundlich adsorption isotherm model compared to the Langmuir model. The Langmuir model assumes identical sites, microscopically flat surface and no interactions between adsorbates, while the Freundlich model is more empirical in nature and better explains heterogeneous surfaces [63], [100], [101]. Indeed, the Freundlich intensity parameter,  $1/n$ , varied across the three Si/Al ratio zeolites, indicating differences in the extent of favorable adsorption or degree of surface adsorption site heterogeneity. It is also interesting to note that Cu-ZSM-5-(11) displayed the lowest normalized adsorption uptake—as indicated by the magnitude of the Freundlich constant,  $K_f$ —even though it featured the lowest  $1/n$  parameter, suggesting the most favorable adsorption. This is perhaps an

indication that different adsorption sites are capable of adsorbing different amounts of phosphate; in other words, a copper dimer (i.e., made up of two copper atoms) may not be able to host double the number of phosphate ions as a single monomeric  $\text{Cu}^{2+}$  site. This will be considered in further detail at a later point in the discussion.

The results from kinetic modeling of phosphate adsorption on Cu-ZSM-5 can provide additional information to understand the active sites. Unfortunately, fitting data to the pseudo first or second order models alone does not reveal any information about the mechanism itself; the intra-particle diffusion model on the other hand is capable of providing mechanistic insight [63]. However, the most useful insight that can be gleaned from the latter in relation to copper ZSM-5 is that adsorption is not controlled solely by intra-particle diffusion of phosphate through the zeolite's channels. This lends credence to the theory of attachment of phosphate anions to copper sites on the framework surface. The pseudo second order modeling revealed important information on the kinetics of adsorption. Namely, there was an order of magnitude decrease in the rate constant,  $k_2$ , for each Cu-ZSM-5 material studied, with Cu-ZSM-5-(11) displaying the fastest kinetics. This tends to suggest a substantial change in the average energy barrier for adsorption-attachment of phosphate. The notion of heterogeneous copper sites would appear to be consistent with this behavior, and could mean that Cu-ZSM-5-(11) had a particularly high proportion of sites featuring a low energy barrier for attachment, while Si/Al ratio 17 and 42 copper zeolites featured significantly lower

proportions in turn. However, based on the available experimental data, it is not possible to quantify directly the energy barriers involved.

#### **5.4 Dimers in copper ZSM-5 and the link to phosphate adsorption**

As outlined in the introduction and literature review of this dissertation, the interest in characterizing dimer species in Cu-ZSM-5 stems from the evidence of their critical catalytic role in SCR reactions. The conclusions from previous studies have indicated that in order to form  $[\text{Cu-O-Cu}]^{2+}$  dimers, two fundamentally important structural criteria must be met: the Si/Al ratio must be low enough such that there is significant probability to form Al-Al pairs that are close enough to support the copper dimer structure (with favorable separation distances estimated at 7.0 to 8.0 Å and a tighter pairing range of 4.2 to 5.5 Å) [41]; and sufficiently high copper loading of the zeolite is needed in order for Cu ions to find a pairable neighbor [41], [42]. Because the data on average Cu···Cu distance shown in Table 4.1 for the ZSM-5 zeolites studied in this work ignores—among other structural considerations—the highly puckered five- and six-membered rings of the framework—which, necessarily increase the probability of shorter Al-Al distances—these values represent merely a proxy for the increased “closeness” of Cu ions with decreasing Si/Al ratio, as depicted in Figure 4.18. Nevertheless, the average distances obtained through calculation based on characterization of the copper content do validate the finding that low Si/Al ratio copper

ZSM-5 materials will likely have a higher proportion of Cu sites capable of forming dimers, given the same approximate Cu/Al ratio.

The calculation of dimer fractions in this work was partly based on the proposal that dimer  $[\text{Cu}-\text{O}-\text{Cu}]^{2+}$  sites have an equilibrium capacity equal to the equilibrium capacity of monomeric  $\text{Cu}^{2+}$  sites (i.e.,  $\delta = 0.5$ , the number of phosphate anions a dimer site can host—per Cu ion—relative to a monomeric site) at the low phosphate concentrations and conditions utilized in this study. This can be justified by comparing the  $\text{Cu}\cdots\text{Cu}$  distance in dimeric copper species to the size of the  $\text{PO}_4^{3-}$  anion. Previously, researchers have compared EXAFS results to spectroscopically characterized Cu–O dimeric species identified in the active sites of enzymes and synthetic models to determine the form of the  $\text{Cu}-\text{O}_x-\text{Cu}$  structure based on matching of the  $\text{Cu}\cdots\text{Cu}$  distance; using this approach, the distance has been reported at  $\sim 2.9$  Å [43], [110]. However, others have cast doubt on the validity of the EXAFS method for measuring the spacing because of the abundant number of spectator Cu sites compared to the activated Cu core [111]. Regardless, the largest Cu–O dimeric species identified for such comparisons—an end-on peroxide-bridged coupled binuclear copper(II) model complex relevant to the active sites in hemocyanin and tyrosinase—featured a  $\text{Cu}\cdots\text{Cu}$  distance of 4.4 Å; this value was considered to be a plausible upper bound for the  $\text{Cu}\cdots\text{Cu}$  distance in copper dimers found in Cu-ZSM-5, even in an aqueous environment where hydrogen abstraction of the ligands or other phenomena may alter the O bridge(s) of the dimer [112], [113]. In

comparison, the  $\text{PO}_4^{3-}$  anion has a thermochemical diameter of 4.6 Å, and the  $\text{H}_2\text{PO}_4^-$  anion has a diameter of 4.3 Å [114]. Therefore, based on a simple size comparison, it's improbable that each Cu atom could adsorb its own phosphate anion in an energetically favorable configuration compared to a single phosphate anion being hosted by the dimer structure. Additionally, *Escherichia coli* alkaline phosphatase (AP)—an enzyme with a zinc(II) dimer active site with a  $\text{Zn}\cdots\text{Zn}$  spacing of  $\sim 4$  Å—features a transition state where the structure of AP binds a single phosphate group during phosphoryl transfer [115]–[117]. Given this well-characterized divalent metal dimer with spacing of  $\sim 4$  Å hosts only a single phosphate anion, it's considered probable that a  $\text{Cu}\cdots\text{Cu}$  dimer of similar (and more likely, smaller) distance would have a similar capacity. Similar size arguments hold for comparisons of the phosphate anion's thermochemical diameter to the pore size within the ZSM-5 framework—approximately 5.5 Å [32]—as sketched in Figure 5.1; it would be difficult for the 10-membered ring to accommodate more than one phosphate anion in a hard sphere model. Therefore, it's reasonable to propose that dimer  $[\text{Cu}-\text{O}-\text{Cu}]^{2+}$  sites in copper ZSM-5 have an equilibrium capacity no higher than that of isolated  $\text{Cu}^{2+}$  monomers at the low phosphate concentrations utilized in this study.

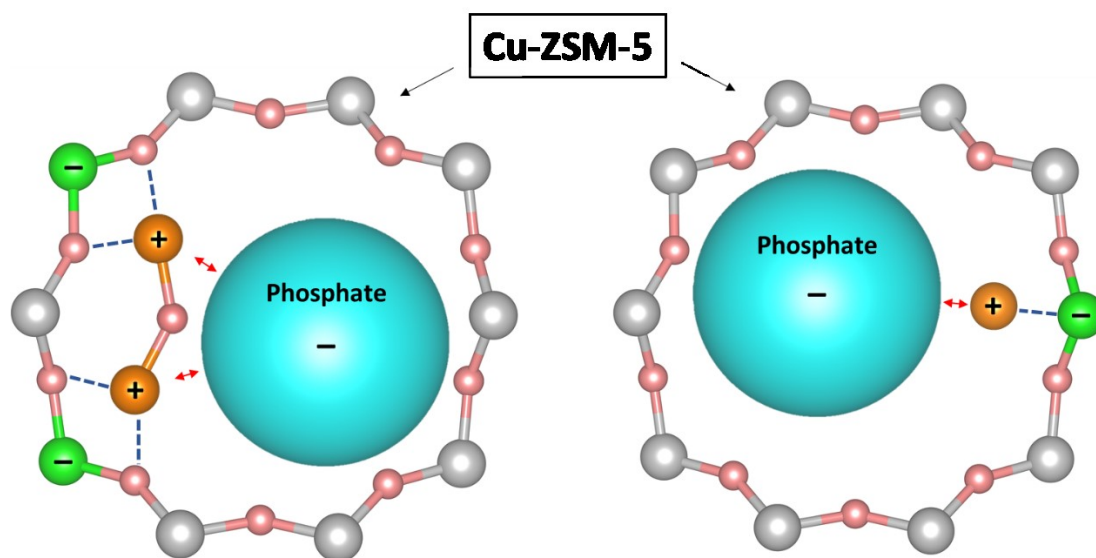


**Figure 5.1** Sketch of proposed phosphate adsorption arrangement in Cu-ZSM-5 by dimer sites (left) and monomer sites (right) in a 10-membered ring of the zeolite. The scaling of the features is approximate only.

The strong linear correlations between Cu density and phosphate adsorption properties normalized by total copper content provide evidence for the ability of the phosphate anion to probe fundamentally different types of sites within Cu-ZSM-5. While acknowledging the limitations of the assumptions underlying their calculation, the estimates for  $\eta_{\text{Cu}\cdots\text{Cu}}$  and deduced scaling relationship with the Cu density based on phosphate adsorption were validated by the general agreement with calculations based on TPR measurements, as shown in Figure 4.21. The better agreement of the estimates and regression based on the Langmuir model's  $Q_{\text{max}}^0$  parameter when compared to the Freundlich model's  $K_f$  is a logical consequence of the former being directly related to the concept of adsorption capacity, while the latter is merely a constant of proportionality related to magnitude of adsorption. Importantly, the similarity of the slope between the dimer estimates calculated from TPR data by Xie *et al.* (which were based on Cu-ZSM-5 at full exchange but with varying Si/Al ratio, similar to this work) and the linear regression of the dimer estimates derived from  $Q_{\text{max}}^0$  is consistent with and further evidence to support an inherent linear scaling relationship with Cu density that is characteristic of the ZSM-5 framework, as proposed by Xie *et al.* [95]. Although there was some agreement with the results of Da Costa *et al.*, it should be noted that the authors in that work primarily varied the Cu/Al ratio rather than the Si/Al ratio; the lowest Cu density point corresponds to copper ZSM-5 with a Cu/Al ratio of only 0.12, which indicates the zeolite was under-exchanged [42]. In this work, full exchange of the zeolite was targeted, and the copper content was varied by changing the Si/Al ratio.

This difference in study design and synthesized zeolites may be responsible for the larger discrepancy observed in both dimer fraction estimates and the scaling relationship when compared to the data from Xie *et al.*

The estimation of dimer fractions and positive correlation with Cu density addresses questions raised by the trends relating to magnitude of adsorption in the phosphate adsorption isotherms and other data normalized by total copper content. Those results (Figure 4.14 and Table 4.3) indicated that while lower Si/Al ratio (i.e., higher dimer fraction) copper ZSM-5 had more favorable adsorption, copper-normalized phosphate uptake was—curiously—also lower. The supporting results in Figure 4.20 showed that by accounting for the observation that a dimeric  $[\text{Cu-O-Cu}]^{2+}$  oxocation structure does not necessarily host twice the number of phosphate anions as an isolated  $\text{Cu}^{2+}$  monomer, the Si/Al ratio trends in adsorption uptake parameters could be explained. This could provide further insight into our previously reported studies of Cu-ZSM-5 as a sorbent for phosphate, where proposed ion exchange mechanisms for the attachment of phosphate ignored the heterogeneous nature of the copper sites discussed here [74]. Furthermore, it can be noted that the adjusted maximum adsorption capacity reported in Figure 4.20 was  $\sim 1.0$  to  $\sim 1.2$  P/Cu<sub>adjusted</sub> units (i.e., units accounting for the reduced host capacity of Cu in the dimer fraction,  $\delta = 0.5$ ). Given the value was close to 1 P/Cu and acknowledging the low phosphate concentration used in the study, this result further suggests that adsorption on Cu sites in copper ZSM-5 was monolayer—or near



monolayer—in nature. The previously discussed speculation on adsorption site heterogeneity based the Freundlich intensity parameter,  $1/n$ , the pseudo second order rate constant,  $k_2$ , and qualitative adsorption isotherm characteristics is supported by the trends with  $\eta_{\text{Cu}\cdots\text{Cu}}$  illustrated in Figure 4.21. From the  $1/n$  results in Figure 4.19 showing a shallow but negative slope, one can deduce that dimer sites are more favorable for the adsorption of phosphate anions based on the general interpretation of the Freundlich intensity parameter [63]. The relationship between  $\ln k_2^*$  and  $\eta_{\text{Cu}\cdots\text{Cu}}$  displayed in Figure 4.21B reveals that dimers have lower energy barriers for adsorption. In particular, the sensitivity of the rate constant with respect to dimer fraction is strong confirmation of heterogeneous adsorption sites. The normalization of the rate constant by the adsorption site density (i.e., Cu density \*  $(\delta \cdot \eta_{\text{Cu}\cdots\text{Cu}} + (1 - \eta_{\text{Cu}\cdots\text{Cu}}))$ ) was necessary to account for the naturally positive contribution from the increased number of adsorption sites in the copper ZSM-5 samples with higher copper loading. The tacit assumption that the phosphate anion sticking probability is directly proportional to the concentration of adsorption sites is a reasonable approximation for the purposes of stripping out this effect. Given that the adjusted rate constant still increased by two orders of magnitude in going from a dimer fraction of ~25% to 75%, the argument for a fundamental difference in the adsorption energy barriers of dimers vs. isolated monomers is reasonably strong. The demonstrated variability in kinetic behavior is indicative of underlying chemisorption processes for phosphate adsorption in addition to the expected physisorption due to Coulombic attraction of the anion. Intuitively, the

differences in molecular and electronic structure between dimers and isolated Cu monomers could shift the chemisorption and physisorption potential energy curves such that the intersection gives rise to substantially different energy barriers for adsorption. The data presented here would tend to suggest that this barrier is greater for adsorption on the isolated monomers. Although it is difficult to state to what extent the adsorption of the phosphate anion is dissociative in nature, the aqueous environment is likely to result in (de)protonation or (de)hydroxylation of the surface (depending on pH), and potentially exchange of  $\text{OH}^-$  consistent with ligand coordination mechanisms frequently reported for phosphate adsorption [21]. However, based on the pH data presented in Figure 4.15—after accounting for the necessary adjustments for adsorption site capacity previously discussed (not shown)—there was no substantial difference between dimers and monomers (where the Si/Al ratio can be used as a proxy for dimer concentration) in their equilibrium capacity to adsorb phosphate anions with different levels of protonation. Furthermore, the equilibrium pH for the adsorption isotherm and kinetic data gathered in this study was less than 7 (i.e.,  $\Delta\text{pH}$  was  $< 0$  at  $\text{pH}_i = 7$ ), indicating  $\text{H}_2\text{PO}_4^-$  was the dominant species in solution. Therefore, it is not believed that the protonation state of phosphate is a significant parameter in the differentiation of dimers from isolated monomers, and the observed kinetic variation is more likely a result of structural differences in the adsorption sites themselves. Ultimately, measurement of kinetic and equilibrium phosphate adsorption properties present novel routes for quantifying and probing the dimer fraction in copper ZSM-5.

## Chapter 6 Conclusions

This dissertation has presented a systematic study of the inorganic dissolved phosphate adsorption properties of copper ZSM-5. The material showed some potential for use as a sorbent in environmental, industrial or municipal waste-water treatment systems, with a maximum P removal of approximately 76% at room temperature, neutral pH, 20 g/L sorbent loading at an initial phosphate concentration of 10 mg-P/L in synthetic solution. Room temperature adsorption isotherms were fit by non-linear regression to the Freundlich and Langmuir adsorption isotherm models, with the Freundlich model showing closer agreement. The Langmuir maximum adsorption capacity was  $\sim 10$  mg-P/g<sub>zeolite</sub> for Cu-ZSM-5 with Si/Al ratio 11, which is comparable in magnitude to the most commonly studied metal hydr(oxide) minerals. Phosphate adsorption on Cu-ZSM-5 increased with increasing initial solution pH, in contrast with most reported sorbents for orthophosphate. The  $\text{pH}_{\text{PZNPC}}$  decreased with increasing Si/Al ratio, due to the substitution of high ionic potential  $\text{Si}^{4+}$  with species of lower ionic potential. The leaching of copper into the post-adsorption filtrate is a potential limitation to the application of copper ZSM-5 for P removal. Metal-exchanged zeolites present a unique direction in the development of highly tunable synthetic sorbents for inorganic dissolved phosphate.

## CONCLUSIONS

The structure-property relationships for Cu-ZSM-5 were investigated with regards to phosphate adsorption. The phosphate adsorption data was normalized by copper content and fit to the pseudo second order kinetic model, for which the rate constant decreased with Si/Al ratio and ranged from 0.14 to 0.004  $\text{g}_{\text{Cu}}/\text{mg-P}\cdot\text{min}$ . The copper-normalized phosphate adsorption property parameters showed strong linear correlations to the Cu density. Equalizing these adsorption parameters by accounting for the reduced anion host capacity—per Cu ion—of dimers vs. monomers facilitated quantification of the dimer fraction, which were estimated at ~100%, 71% and 28% for Si/Al ratios 11, 17 and 42, respectively. The estimated linear scaling relationship between dimer fraction and Cu density was ~1.6. Negative correlation with the Freundlich adsorption isotherm intensity parameter,  $1/n$ , suggested dimers are favorable for phosphate adsorption, while a positive correlation with  $\ln k_2^*$  indicated the energy barrier for attachment to dimers is lower than for isolated  $\text{Cu}^{2+}$  monomers. The kinetic rate constant showed the greatest sensitivity to changes in dimer fraction. Therefore, phosphate anion adsorption can distinguish copper ions in dimers from those in monomeric structures based on the proposed per-ion capacity difference. The results and analysis also indicated that adsorption is monolayer in nature for the low phosphate concentration range studied. In conclusion, liquid phase phosphate anion adsorption can be used as a tool to probe and quantify the copper speciation in copper-exchanged

## CONCLUSIONS

ZSM-5. This presents a new and unique direction for understanding the active site structures in metal-exchanged zeolites.

## Chapter 7 Supplementary

The body of this dissertation focused on the topic of phosphate adsorption by copper ZSM-5. However, in addition to this work a considerable effort was made in exploring other topics relevant to phosphate chemistry. Here, a brief accounting of the most promising supplementary project has been presented.

### **7.1 Synthetic enzymes and the transition state in heterogeneous catalytic dephosphorylation**

Phosphoryl transfer plays an incredibly important role in the biology of life. Part of this importance can be traced to the rather unique ability of phosphorus to form chemically stable esters and anhydrides at ambient, aqueous physiological conditions; such properties are often central to discussions on why nature “chose” phosphate for its role in biological molecules [118], [119]. The cleavage and formation of the P–O bond in phosphate esters—in some ways, resembling an biological switch—is critical to a variety of biochemical processes, including energy transfer, biosynthesis, messaging, regulation of protein function and preservation of genetic material [118]. However, the rate of phosphoryl transfer reactions in the absence of enzymes is very slow [120]. Therefore, biological catalysts—phosphatases for cleavage of the P–O bond and

kinases for formation—are essential in providing the immense but necessary increases in reaction rates [121]. Figure 7.1 illustrates a simplified scheme for the enzymatic hydrolysis of a phosphomonoester substrate.

In order to understand the rate enhancements effected by enzymes, the nature of the transition state must be investigated; it is the stabilization of this transition state relative to the ground reference that leads to catalytic activity. Alkaline phosphatase (AP), in particular, has been well studied in this regard [115]–[117], [122]. A common technique for studying the transition state in these enzymatic systems is to use linear free-energy relationships (LFER); the observed rate constant,  $k_{obs}$ , is measured for a series of substrates with leaving groups of varying  $pK_a$ , and the fitted Brønsted coefficient— $\beta_{lg}$  in equation 8—is used to infer the “tightness” of the transition state.

$$\log k_{obs} = \beta_{lg} \cdot pK_a + C \quad (\text{Equation 8})$$

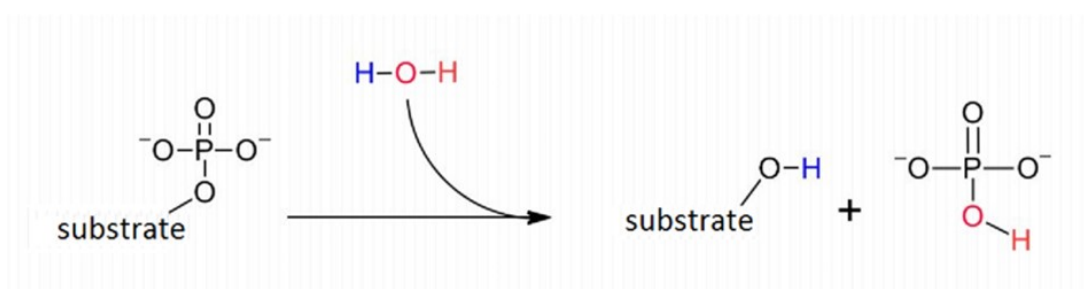
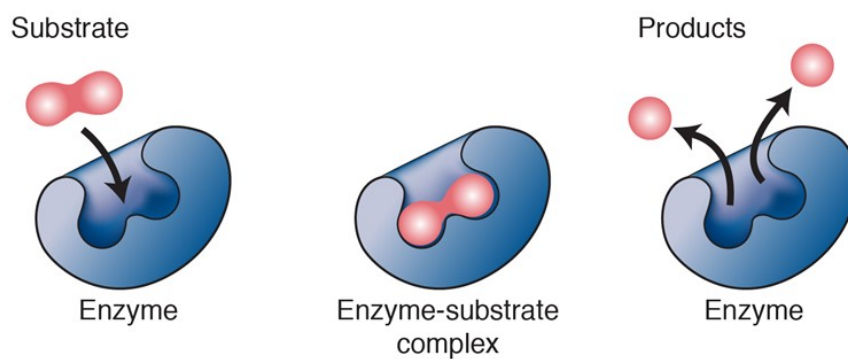


**Figure 7.1** Simplified scheme for the enzymatic hydrolysis of a phosphomonoester substrate [123], [124].



The Brønsted equation shown in equation 8 implies the Gibbs free energy for dissociation (given by  $pK_a$  of the substrate's leaving group in this context) is proportional to activation energy for catalytic step (represented by the rate constant). Therefore,  $\beta_{lg}$  can be used as a measure of dissociative vs. associative nature of the transition state. If the slope is steep, the transition complex is dissociative (i.e., most bond cleavage has already occurred in getting to the transition state and catalytic activity is driven by how tight leaving group “grips” onto the substrate). On the other hand, a flat slope indicates the transition state is associative (i.e., little bond cleavage has occurred, and how tight leaving group “grips” to substrate is largely irrelevant). Previous reports have shown that without the AP enzyme, phosphoryl transfer is highly dissociative for monoesters, and remains mostly so for energetic reasons when AP is introduced, notwithstanding significant differences in the reaction rate [115].

Synthetic enzymes—i.e., catalysts that can be synthesized by purely chemical routes but applied to biomolecular reactions—have gained interest due to their central role in the developing field of artificial biology and for improving fundamental understanding of the chemical processes that sustain life [125]–[127]. In terms of solid catalysts, cerium oxide nanoparticles have demonstrated activity relevant to biomolecular reactions owing to its unusual mixed-valence crystal structure leading to a high concentration of redox active oxygen vacancies [128]–[130]. In particular, our group has previously studied catalytic dephosphorylation of the model substrate *para*-

nitrophenyl phosphate (*p*-NPP) by cerium oxide nanocrystals [131]. The *p*-NPP substrate is widely used for assays of alkaline phosphatase in ELISA applications, with convenient UV detection mediated by the chromogenic properties of the substrate (and with pH modification, the reaction product, *para*-nitrophenol).

In this work, we explore the nature of the ceria–organophosphate surface transition state by studying the hydrolysis of a series of alkyl and aryl phosphomonoesters, incorporating LFER techniques that have previously been applied to biological catalysts such as AP. By studying how the nature of the surface complex changes with respect to reaction conditions and nanoparticle morphology (e.g., size, exposed crystal facets, oxygen vacancy density), we hope to gain an improved understanding of the mechanism by which ceria acts as a catalyst for the dephosphorylation of phosphomonoesters.

### 7.1.1 Methodology

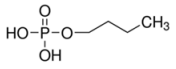
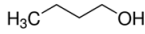
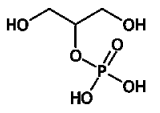
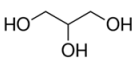
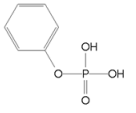
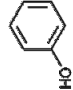
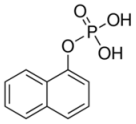
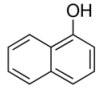
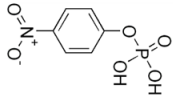
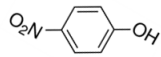
Most of the techniques applied in the supplementary project build off the methodology presented in the main body of this dissertation. Importantly, the extent of reaction was calculated by measuring the quantity of phosphate produced in the reaction solutions.

Commercial cerium(IV) oxide nanopowder was used as the catalyst material in this study ( $\geq 99.5\%$ , Alfa Aesar), along with five phosphate ester salts as substrates:  $\beta$ -

Glycerophosphate disodium salt hydrate ( $\geq 99\%$ , Sigma-Aldrich), Butyl phosphate (Sigma-Aldrich), 1-Naphthyl phosphate monosodium salt monohydrate ( $\geq 98\%$ , Sigma-Aldrich), Sodium phenyl phosphate dibasic dihydrate ( $\geq 95\%$ , Sigma-Aldrich), *para*-nitrophenyl phosphate disodium salt hexahydrate (pNPP,  $\geq 99\%$ , Sigma-Aldrich). A summary of the chemical structures, leaving groups and corresponding  $pK_a$  values is presented in Figure 7.2.

Where experiments were conducted above room temperature, an oil bath was used to regulate temperature with the solution temperature measured directly with a glass thermometer. All substrate solutions were preheated to the target temperature and adjusted to pH 7 prior to the addition of the catalyst powder. The mass of catalyst was 3.5 mg, the substrate solution volume was 50 mL and the substrate concentration was 1 mM. A stir bar was added to each reaction vessel and maintained at 600 RPM. The observed kinetic rate constant was estimated by linear regression of the initial portion of the kinetic curve—typically less than 30 minutes—with a minimum of five data points.

SUPPLEMENTARY

	Phosphate ester	Leaving group alcohol	pK <sub>a</sub> of alcohol <sup>[1]</sup>
<b>Butyl acid phosphate</b>			<b>16.1</b>
<b>β-Glycerophosphate</b>			<b>14.4</b>
<b>Phenyl phosphate</b>			<b>10.0</b>
<b>1-Naphthyl phosphate</b>			<b>9.3 – 9.4</b>
<b>p-nitrophenyl phosphate</b>			<b>7.2</b>



**Figure 7.2** Summary of the phosphomonoester substrates utilized in this study. The pK<sub>a</sub> values were sourced from Serjeant *et al.* [132].

### 7.1.2 Results, Discussion and Future Work

The observed rate constant was plotted against the  $pK_a$  of the leaving group, as shown in Figure 7.3. The results show a broadly similar negative correlation at all tested temperatures from 50°C to 90°C. However, the rate constant was significantly higher at elevated temperatures, as expected. The results indicated that given a fixed temperature, the dephosphorylation of *para*-nitrophenyl phosphate featured the fastest reaction kinetics, while the cleaving of the phosphomonoester bond in butyl acid phosphate was the slowest. Based on the data presented in Table 7.1, the average  $\beta_{lg}$  was -0.16, indicating that the transition complex in dephosphorylation by commercial cerium oxide nanoparticles had less dissociative character than alkaline phosphatase, where reported values are  $\sim -0.8$  and the transition state is considered dissociative [115], [116]. Based on the observed change in LFER relationships in going from phosphate monoesters to diesters, a criteria of  $\Delta\beta_{lg} \sim +0.47$  has been used to gauge a significant change to a more associate transition states [115]. Therefore, the LFER analysis conducted in this work supports the conclusion of an associative transition state.

In addition to building on the preliminary LFER results presented above, future work on this project will involve analysis of the activation energies of dephosphorylation and comparisons with different morphologies of cerium oxide nanoparticles. As of the writing of this dissertation, this work was still ongoing.

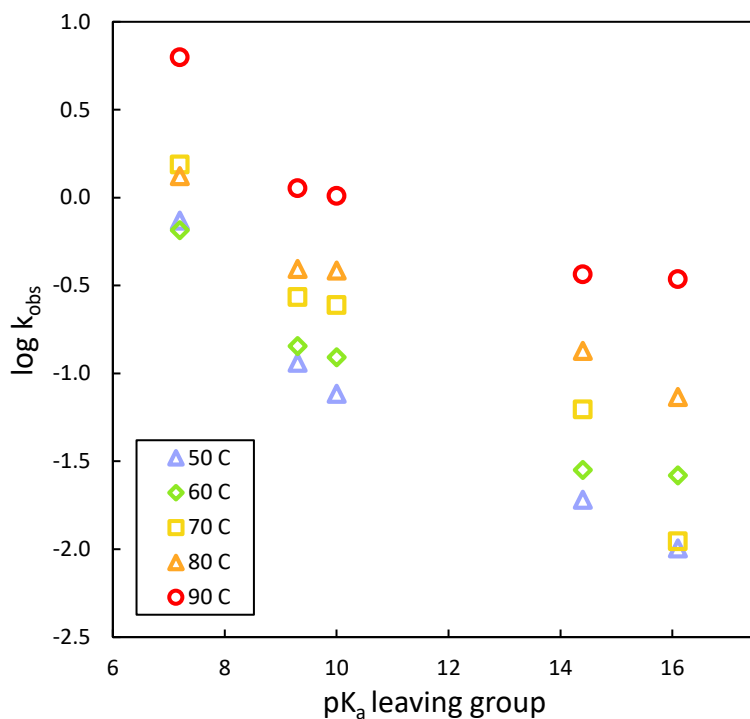


**Figure 7.3** The leaving group dependence for catalytic dephosphorylation by cerium oxide nanoparticles at five different temperatures. The best fit slope data is presented in Table 7.1.

**Table 7.1** LFER results for catalytic dephosphorylation

Temperature	Brønsted coefficient data		
	$\beta_{ig}$	$\pm$ error (95% conf. interval)	$R^2$
50°C	-0.19	0.09	0.94
60°C	-0.15	0.08	0.93
70°C	-0.21	0.09	0.95
80°C	-0.13	0.05	0.96
90°C	-0.13	0.10	0.84

## Chapter 8 References

- [1] M. A. Malboobi and A. Samaeian, "Plant Phosphate Nutrition and Environmental Challenges," pp. 3–34, 2012.
- [2] V. Smil, "Phosphorus in the environment: Natural flows and human interferences," *Annu. Rev. Energy Environ.*, vol. 25, pp. 53–88, 2000.
- [3] V. van Ginneken, E. de Vries, and T. Wijgerde, "A Suggested " Seaweed-Plantation Model " to Tackle the Looming Phosphorus Crises in the 21st Century at the Rhine/North-Sea System," *J. Fish. Sci.*, vol. 9, no. 1, pp. 105–114, 2016.
- [4] N. Gilbert, "Environment: The disappearing nutrient," *Nature*, vol. 461, no. 7265, pp. 716–718, Oct. 2009.
- [5] J. Cooper, R. Lombardi, D. Boardman, and C. Carliell-Marquet, "The future distribution and production of global phosphate rock reserves," *Resour. Conserv. Recycl.*, vol. 57, no. January, pp. 78–86, 2011.
- [6] The Editors of Encyclopaedia Britannica, "Biogeochemical cycle," *Encyclopædia Britannica*, 2016. [Online]. Available: <https://www.britannica.com/science/biogeochemical-cycle>. [Accessed: 23-Apr-2020].
- [7] U.S Geological Survey, *Mineral Commodity Summaries 2020*, no. 703. 2020.
- [8] D. P. Van Vuuren, A. F. Bouwman, and A. H. W. Beusen, "Phosphorus demand for the 1970-2100 period: A scenario analysis of resource depletion," *Glob. Environ. Chang.*, vol. 20, no. 3, pp. 428–439, 2010.
- [9] D. Cordell and S. White, "Peak phosphorus: Clarifying the key issues of a vigorous debate about long-term phosphorus security," *Sustainability*, vol. 3, no. 10, pp. 2027–2049, 2011.
- [10] D. Pimentel, "Soil erosion: A food and environmental threat," *Environ. Dev. Sustain.*, vol. 8, no. 1, pp. 119–137, 2006.

## REFERENCES

- [11] A. N. Sharpley and P. J. A. Withers, “The environmentally-sound management of agricultural phosphorus,” *Fertil. Res.*, vol. 39, no. 2, pp. 133–146, 1994.
- [12] S. E. Shumway, “A Review of the Effects of Algal Blooms on Shellfish and Aquaculture,” *J. World Aquac. Soc.*, vol. 21, no. 2, pp. 65–104, 1990.
- [13] W. M. Kemp *et al.*, “Eutrophication of Chesapeake Bay: Historical trends and ecological interactions,” *Mar. Ecol. Prog. Ser.*, vol. 303, pp. 1–29, 2005.
- [14] B. G. Gustafsson *et al.*, “Reconstructing the development of baltic sea eutrophication 1850-2006,” *Ambio*, vol. 41, no. 6, pp. 534–548, 2012.
- [15] J. E. Brodie, M. Devlin, D. Haynes, and J. Waterhouse, “Assessment of the eutrophication status of the Great Barrier Reef lagoon (Australia),” *Biogeochemistry*, vol. 106, no. 2, pp. 281–302, 2011.
- [16] E. A. Paul and F. E. Clark, *Soil microbiology and biochemistry*. 1988.
- [17] J. R. Mihelcic *et al.*, “The Grandest Challenge of All: The Role of Environmental Engineering to Achieve Sustainability in the World’s Developing Regions,” *Environ. Eng. Sci.*, vol. 34, no. 1, pp. 16–41, 2017.
- [18] B. K. Mayer *et al.*, “Total Value of Phosphorus Recovery,” *Environ. Sci. Technol.*, vol. 50, no. 13, pp. 6606–6620, 2016.
- [19] X. Hao, C. Wang, M. C. M. Van Loosdrecht, and Y. Hu, “Looking beyond struvite for P-recovery,” *Environ. Sci. Technol.*, vol. 47, no. 10, pp. 4965–4966, 2013.
- [20] L. Egle, H. Rechberger, J. Krampe, and M. Zessner, “Phosphorus recovery from municipal wastewater: An integrated comparative technological, environmental and economic assessment of P recovery technologies,” *Sci. Total Environ.*, vol. 571, pp. 522–542, 2016.
- [21] P. Loganathan, S. Vigneswaran, J. Kandasamy, and N. S. Bolan, “Removal and recovery of phosphate from water using sorption,” *Crit. Rev. Environ. Sci. Technol.*, vol. 44, no. 8, pp. 847–907, 2014.
- [22] M. Khalid, E. Johnson, A. Vij, E. J. Bouwer, H. A. Janjua, and M. J. Betenbaugh, “Anaerobic digestion restricted to phase I for nutrient release and energy production using waste-water grown *Chlorella vulgaris*,” *Chem. Eng. J.*, vol. 352, no. May, pp. 756–764, 2018.
- [23] J. Gustavsson, C. Cederberg, U. Sonesson, R. van Otterdijk, and A. Meybeck,



## REFERENCES

- “Global food losses and food waste: extent, causes and prevention,” no. BOOK, pp. vi, 29 pp., 2011.
- [24] V. V. Shenoy and G. M. Kalagudi, “Enhancing plant phosphorus use efficiency for sustainable cropping,” *Biotechnol. Adv.*, vol. 23, no. 7–8, pp. 501–513, 2005.
- [25] R. Mallampati and S. Valiyaveetil, “Apple peels - A versatile biomass for water purification?,” *ACS Appl. Mater. Interfaces*, vol. 5, no. 10, pp. 4443–4449, 2013.
- [26] P. A. Trazzi, J. J. Leahy, M. H. B. Hayes, and W. Kwapinski, “Adsorption and desorption of phosphate on biochars,” *J. Environ. Chem. Eng.*, vol. 4, no. 1, pp. 37–46, 2016.
- [27] M. S. Onyango, D. Kuchar, M. Kubota, and H. Matsuda, “Adsorptive removal of phosphate ions from aqueous solution using synthetic zeolite,” *Ind. Eng. Chem. Res.*, vol. 46, no. 3, pp. 894–900, 2007.
- [28] R. Chitrakar, S. Tezuka, A. Sonoda, K. Sakane, K. Ooi, and T. Hirotsu, “Phosphate adsorption on synthetic goethite and akaganeite,” *J. Colloid Interface Sci.*, vol. 298, no. 2, pp. 602–608, 2006.
- [29] E. A. Deliyanni, E. N. Peleka, and N. K. Lazaridis, “Comparative study of phosphates removal from aqueous solutions by nanocrystalline akaganéite and hybrid surfactant-akaganéite,” *Sep. Purif. Technol.*, vol. 52, no. 3, pp. 478–486, 2007.
- [30] T. J. Daou *et al.*, “Phosphate adsorption properties of magnetite-based nanoparticles,” *Chem. Mater.*, vol. 19, no. 18, pp. 4494–4505, 2007.
- [31] C. Colella and A. F. Gualtieri, “Cronstedt’s zeolite,” *Microporous Mesoporous Mater.*, vol. 105, no. 3, pp. 213–221, 2007.
- [32] N. Jiang, R. Shang, S. G. J. Heijman, and L. C. Rietveld, “High-silica zeolites for adsorption of organic micro-pollutants in water treatment: A review,” *Water Res.*, vol. 144, pp. 145–161, 2018.
- [33] J. Přech, P. Pizarro, D. P. Serrano, and J. Áejka, “From 3D to 2D zeolite catalytic materials,” *Chem. Soc. Rev.*, vol. 47, no. 22, pp. 8263–8306, 2018.
- [34] T. Maesen and B. Marcus, “Chapter 1 The zeolite scene—An overview,” in *Introduction to Zeolite Science and Practice*, vol. 137, H. [van Bekkum], E. M. Flanigen, P. A. Jacobs, and J. C. Jansen, Eds. Elsevier, 2001, pp. 1–9.

## REFERENCES

- [35] S. Brandenberger, O. Kröcher, A. Tissler, and R. Althoff, "Effect of structural and preparation parameters on the activity and hydrothermal stability of metal-exchanged ZSM-5 in the selective catalytic reduction of NO by NH<sub>3</sub>," *Ind. Eng. Chem. Res.*, vol. 50, no. 8, pp. 4308–4319, 2011.
- [36] A. M. Beale, F. Gao, I. Lezcano-Gonzalez, C. H. F. Peden, and J. Szanyi, "Recent advances in automotive catalysis for NO<sub>x</sub> emission control by small-pore microporous materials," *Chem. Soc. Rev.*, vol. 44, no. 20, pp. 7371–7405, 2015.
- [37] S. Brandenberger, O. Kröcher, A. Tissler, and R. Althoff, *The state of the art in selective catalytic reduction of NO<sub>x</sub> by ammonia using metal-exchanged zeolite catalysts*, vol. 50, no. 4. 2008.
- [38] M. Iwamoto, H. Furukawa, Y. Mine, F. Uemura, S. I. Mikuriya, and S. Kagawa, "Copper(II) Ion-exchanged ZSM-5 zeolites as highly active catalysts for direct and continuous decomposition of nitrogen monoxide," *J. Chem. Soc. - Ser. Chem. Commun.*, no. 1272, pp. 1272–1273, 1986.
- [39] M. Shelef, C. N. Montreuil, and H. W. Jen, "NO<sub>2</sub> formation over Cu-ZSM-5 and the selective catalytic reduction of NO," *Catal. Letters*, vol. 26, no. 3–4, pp. 277–284, 1994.
- [40] J. H. Kwak, R. G. Tonkyn, D. H. Kim, J. Szanyi, and C. H. F. Peden, "Excellent activity and selectivity of Cu-SSZ-13 in the selective catalytic reduction of NO<sub>x</sub> with NH<sub>3</sub>," *J. Catal.*, vol. 275, no. 2, pp. 187–190, 2010.
- [41] B. R. Goodman, K. C. Hass, W. F. Schneider, and J. B. Adams, "Statistical analysis of Al distributions and metal ion pairing probabilities in zeolites," *Catal. Letters*, vol. 68, no. 1–2, pp. 85–93, 2000.
- [42] P. Da Costa, B. Modén, G. D. Meitzner, D. K. Lee, and E. Iglesia, "Spectroscopic and chemical characterization of active and inactive Cu species in NO decomposition catalysts based on Cu-ZSM5," *Phys. Chem. Chem. Phys.*, vol. 4, no. 18, pp. 4590–4601, 2002.
- [43] M. H. Grootaert, J. A. Van Bokhoven, A. A. Battiston, B. M. Weckhuysen, and R. A. Schoonheydt, "Bis( $\mu$ -oxo)copper in Cu-ZSM-5 and its role in the decomposition of NO: A combined in situ XAFS, UV-vis-near-IR, and kinetic study," *J. Am. Chem. Soc.*, vol. 125, no. 25, pp. 7629–7640, 2003.
- [44] S. A. Yashnik and Z. R. Ismagilov, "Zeolite ZSM-5 containing copper ions: The effect of the copper salt anion and NH<sub>4</sub>OH/Cu<sup>2+</sup> ratio on the state of the

## REFERENCES

- copper ions and on the reactivity of the zeolite in DeNO<sub>x</sub>,” *Kinet. Catal.*, vol. 57, no. 6, pp. 776–796, 2016.
- [45] S. Morpurgo, “The mechanism of NO and N<sub>2</sub>O decomposition catalyzed by short-distance Cu(I) pairs in Cu-ZSM-5: A DFT study on the possible role of NO and NO<sub>2</sub> in the [Cu–O–Cu]<sub>2</sub><sup>+</sup> active site reduction,” *J. Catal.*, vol. 366, no. 2, pp. 189–201, 2018.
- [46] G. K. Morse, S. W. Brett, J. A. Guy, and J. N. Lester, “Review: Phosphorus removal and recovery technologies,” *Sci. Total Environ.*, vol. 212, no. 1, pp. 69–81, 1998.
- [47] D. Fongers, “The Basics of Phosphorus Removal,” *Michigan Department of Environmental Quality, Operator Training and Certification Unit*, 1999. [Online]. Available: [https://www.michigan.gov/documents/deq/wrd-ot-basics-of-phosphorus-removal\\_445207\\_7.ppt](https://www.michigan.gov/documents/deq/wrd-ot-basics-of-phosphorus-removal_445207_7.ppt).
- [48] T. H. Muster, G. B. Douglas, N. Sherman, A. Seeber, N. Wright, and Y. Güzükkara, “Towards effective phosphorus recycling from wastewater: Quantity and quality,” *Chemosphere*, vol. 91, no. 5, pp. 676–684, 2013.
- [49] A. E. Greenberg, G. Klein, and W. J. Kaufman, “Effect of Phosphorus on the Activated Sludge Process,” *Sewage Ind. Waste.*, vol. 27, no. 3, pp. 277–282, 1955.
- [50] S. Salehi, K. Y. Cheng, A. Heitz, and M. P. Ginige, “Re-visiting the Phostrip process to recover phosphorus from municipal wastewater,” *Chem. Eng. J.*, vol. 343, no. February, pp. 390–398, 2018.
- [51] Y. Liu, G. Villalba, R. U. Ayres, and H. Schroder, “Global phosphorus flows and environmental impacts from a consumption perspective,” *J. Ind. Ecol.*, vol. 12, no. 2, pp. 229–247, 2008.
- [52] W. H. Schlesinger, *Biogeochemistry: An Analysis of Global Change*. 1991.
- [53] S. K. Pradhan, A. Mikola, and R. Vahala, “Nitrogen and Phosphorus Harvesting from Human Urine Using a Stripping, Absorption, and Precipitation Process,” *Environ. Sci. Technol.*, vol. 51, no. 9, pp. 5165–5171, 2017.
- [54] X.-D. Hao, C.-C. Wang, L. Lan, and M. C. M. van Loosdrecht, “Struvite formation, analytical methods and effects of pH and Ca<sup>2+</sup>,” *Water Sci. Technol.*, vol. 58, no. 8, pp. 1687–1692, 2008.
- [55] M. Li, J. Liu, Y. Xu, and G. Qian, “Phosphate adsorption on metal oxides and

## REFERENCES

- metal hydroxides: A comparative review,” *Environ. Rev.*, vol. 24, no. 3, pp. 319–332, 2016.
- [56] A. Thompson and K. W. Goynes, “Introduction to the Sorption of Chemical Constituents in Soils,” *Nat. Educ. Knowl.*, vol. 4, no. 4, p. 7, 2012.
- [57] N. S. Bolan, J. K. Syers, and M. E. Sumner, “Calcium-Induced Sulfate Adsorption by Soils,” *Soil Sci. Soc. Am. J.*, vol. 57, no. 3, pp. 691–696, 1993.
- [58] B. Saha, S. Chakraborty, and G. Das, “A mechanistic insight into enhanced and selective phosphate adsorption on a coated carboxylated surface,” *J. Colloid Interface Sci.*, vol. 331, no. 1, pp. 21–26, 2009.
- [59] J. A. Veith and G. Sposito, “On the Use of the Langmuir Equation in the Interpretation of ‘Adsorption’ Phenomena,” *Soil Sci. Soc. Am. J.*, vol. 41, no. 4, pp. 697–702, 1977.
- [60] D. L. Sparks, “Elucidating the fundamental chemistry of soils: past and recent achievements and future frontiers,” *Geoderma*, vol. 100, pp. 303–319, 2001.
- [61] S. Nagamine, T. Ueda, I. Masuda, T. Mori, E. Sasaoka, and I. Joko, “Removal of phosphorus from wastewater by crystallization on the surface of macroporous TiO<sub>2</sub> with a fibrous microstructure,” *Ind. Eng. Chem. Res.*, vol. 42, no. 20, pp. 4748–4752, 2003.
- [62] W. J. Weber and M. Asce, “Evolution of a Technology,” *J. Environ. Eng.*, vol. 110, no. 5, pp. 899–917, 1984.
- [63] H. N. Tran, S. J. You, A. Hosseini-Bandegharaei, and H. P. Chao, “Mistakes and inconsistencies regarding adsorption of contaminants from aqueous solutions: A critical review,” *Water Res.*, vol. 120, pp. 88–116, 2017.
- [64] F. C. Wu, R. L. Tseng, and R. S. Juang, “Initial behavior of intraparticle diffusion model used in the description of adsorption kinetics,” *Chem. Eng. J.*, vol. 153, no. 1–3, pp. 1–8, 2009.
- [65] W. J. Weber and J. C. Morris, “Kinetics of adsorption on carbon from solution,” *J. Sanit. Eng. Div.*, vol. 89, no. 2, pp. 31–60, 1963.
- [66] M. N. Afridi, W. H. Lee, and J. O. Kim, “Effect of phosphate concentration, anions, heavy metals, and organic matter on phosphate adsorption from wastewater using anodized iron oxide nanoflakes,” *Environ. Res.*, vol. 171, no. December 2018, pp. 428–436, 2019.

## REFERENCES

- [67] K. H. Goh, T. T. Lim, and Z. Dong, "Application of layered double hydroxides for removal of oxyanions: A review," *Water Res.*, vol. 42, no. 6–7, pp. 1343–1368, 2008.
- [68] C. V. Luengo, M. A. Volpe, and M. J. Avena, "High sorption of phosphate on Mg-Al layered double hydroxides: Kinetics and equilibrium," *J. Environ. Chem. Eng.*, vol. 5, no. 5, pp. 4656–4662, 2017.
- [69] W. Shi *et al.*, "Enhanced phosphate removal by zeolite loaded with Mg–Al–La ternary (hydr)oxides from aqueous solutions: Performance and mechanism," *Chem. Eng. J.*, vol. 357, no. July 2018, pp. 33–44, 2019.
- [70] T. H. Pham, K. M. Lee, M. S. Kim, J. Seo, and C. Lee, "La-modified ZSM-5 zeolite beads for enhancement in removal and recovery of phosphate," *Microporous Mesoporous Mater.*, vol. 279, no. December 2018, pp. 37–44, 2019.
- [71] J. Goscianska, M. Ptazkowska-Koniarz, M. Frankowski, M. Franus, R. Panek, and W. Franus, "Removal of phosphate from water by lanthanum-modified zeolites obtained from fly ash," *J. Colloid Interface Sci.*, vol. 513, pp. 72–81, 2018.
- [72] Y. He, H. Lin, Y. Dong, Q. Liu, and L. Wang, "Simultaneous removal of ammonium and phosphate by alkaline-activated and lanthanum-impregnated zeolite," *Chemosphere*, vol. 164, pp. 387–395, 2016.
- [73] Y. He, H. Lin, Y. Dong, and L. Wang, "Preferable adsorption of phosphate using lanthanum-incorporated porous zeolite: Characteristics and mechanism," *Appl. Surf. Sci.*, vol. 426, pp. 995–1004, 2017.
- [74] M. J. Manto, P. Xie, M. A. Keller, W. E. Liano, T. Pu, and C. Wang, "Recovery of Inorganic Phosphorus Using Copper-Substituted ZSM-5," *ACS Sustain. Chem. Eng.*, vol. 5, no. 7, pp. 6192–6200, 2017.
- [75] P. Suresh Kumar *et al.*, "Understanding and improving the reusability of phosphate adsorbents for wastewater effluent polishing," *Water Res.*, vol. 145, pp. 365–374, 2018.
- [76] R. Mallampati, L. Xuanjun, A. Adin, and S. Valiyaveetil, "Fruit peels as efficient renewable adsorbents for removal of dissolved heavy metals and dyes from water," *ACS Sustain. Chem. Eng.*, vol. 3, no. 6, pp. 1117–1124, 2015.
- [77] D. R. Corbin, J. A. C. Soc, D. C. Koningsberger, and D. E. Ramaker, "Applications of X-ray Absorption Spectroscopy in Heterogeneous Catalysis:

## REFERENCES

- EXAFS, Atomic XAFS, and Delta XANES,” in *Handbook of Heterogeneous Catalysis: Online*, no. c, 2006, pp. 774–803.
- [78] M. Tromp, J. A. Van Bokhoven, A. M. Arink, J. H. Bitter, G. Van Koten, and D. C. Koningsberger, “Cu K-edge EXAFS characterisation of copper(I) arenethiolate complexes in both the solid and liquid state: Detection of Cu-Cu coordination,” *Chem. - A Eur. J.*, vol. 8, no. 24, pp. 5667–5678, 2002.
- [79] A. Delabie, K. Pierloot, M. H. Grootaert, R. A. Schoonheydt, and L. G. Vanquickenborne, “The coordination of CuII in zeolites - Structure and spectroscopic properties,” *Eur. J. Inorg. Chem.*, no. 3, pp. 515–530, 2002.
- [80] G. Turnes Palomino, P. Fiscaro, S. Bordiga, A. Zecchina, E. Giamello, and C. Lamberti, “Oxidation States of Copper Ions in ZSM-5 Zeolites. A Multitechnique Investigation,” *J. Phys. Chem. B*, vol. 104, no. 17, pp. 4064–4073, 2000.
- [81] S. A. Fitzgerald *et al.*, “Temperature-Programmed Desorption for Isotope Separation in Nanoporous Materials,” *J. Phys. Chem. C*, vol. 122, no. 4, pp. 1995–2001, 2018.
- [82] M. Moreno-Recio, J. Santamaría-González, and P. Maireles-Torres, “Brønsted and Lewis acid ZSM-5 zeolites for the catalytic dehydration of glucose into 5-hydroxymethylfurfural,” *Chem. Eng. J.*, vol. 303, pp. 22–30, 2016.
- [83] P. B. Stark, “No reproducibility without preproducibility,” *Nature*, vol. 557, no. 7707, p. 613, 2018.
- [84] J. Kim, W. Li, B. L. Philips, and C. P. Grey, “Phosphate adsorption on the iron oxyhydroxides goethite ( $\alpha$ -FeOOH), akaganeite ( $\beta$ -FeOOH), and lepidocrocite ( $\gamma$ -FeOOH): A31P NMR Study,” *Energy Environ. Sci.*, vol. 4, no. 10, pp. 4298–4305, 2011.
- [85] E. A. Nagul, I. D. McKelvie, P. Worsfold, and S. D. Kolev, “The molybdenum blue reaction for the determination of orthophosphate revisited: Opening the black box,” *Anal. Chim. Acta*, vol. 890, pp. 60–82, 2015.
- [86] P. J. Worsfold *et al.*, “Sampling, sample treatment and quality assurance issues for the determination of phosphorus species in natural waters and soils,” *Talanta*, vol. 66, no. 2 SPEC. ISS., pp. 273–293, 2005.
- [87] J. Murphy and J. P. Riley, “A modified single solution method for the determination of phosphate in natural waters,” *Anal. Chim. Acta*, vol. 27, no. C, pp. 31–36, 1962.

## REFERENCES

- [88] U.S. Environmental Protection Agency, “Phosphorous, all Forms (colorimetric, ascorbic acid, two reagent),” *Method 365.3*, vol. National P, pp. 3–7, 1978.
- [89] K. Robards, I. D. McKelvie, R. L. Benson, P. J. Worsfold, N. J. Blundell, and H. Casey, “Determination of carbon, phosphorus, nitrogen and silicon species in waters,” *Anal. Chim. Acta*, vol. 287, no. 3, pp. 147–190, 1994.
- [90] J. E. Harwood, R. A. van Steenderen, and A. L. Kühn, “A rapid method for orthophosphate analysis at high concentrations in water,” *Water Res.*, vol. 3, no. 6, pp. 417–423, 1969.
- [91] A. N. Spiess and N. Neumeyer, “An evaluation of R2as an inadequate measure for nonlinear models in pharmacological and biochemical research: A Monte Carlo approach,” *BMC Pharmacol.*, vol. 10, pp. 1–11, 2010.
- [92] Hach, “Phosphorus , Reactive ( Orthophosphate ) and Total, DOC316.53.01124,” pp. 1–8, 2016.
- [93] V. R. Choudhary and A. P. Singh, “Sorption capacity and diffusion of pure liquids in ZSM-5 type zeolites,” *Zeolites*, vol. 6, no. 3, pp. 206–208, 1986.
- [94] C. Paolucci *et al.*, “Dynamic multinuclear sites formed by mobilized copper ions in NOx selective catalytic reduction,” *Science (80-. )*, vol. 357, no. 6354, pp. 898–903, 2017.
- [95] P. Xie, T. Pu, G. Aranovich, J. Guo, M. Donohue, and C. Wang, “Bridging Adsorption Analytics and Catalytic Kinetics for Metal-Exchanged Zeolites,” *Accept. Nat. Catal.*, 2020.
- [96] P. A. Jacobs, H. K. Beyer, and J. Valyon, “Properties of the end members in the Pentasil-family of zeolites: characterization as adsorbents,” *Zeolites*, vol. 1, no. 3, pp. 161–168, 1981.
- [97] J. M. Arroyave, V. Puccia, G. P. Zanini, and M. J. Avena, “Surface speciation of phosphate on goethite as seen by InfraRed Surface Titrations (IRST),” *Spectrochim. Acta - Part A Mol. Biomol. Spectrosc.*, vol. 199, pp. 57–64, 2018.
- [98] W. Jastrzbski, M. Sitarz, M. Rokita, and K. Bułat, “Infrared spectroscopy of different phosphates structures,” *Spectrochim. Acta - Part A Mol. Biomol. Spectrosc.*, vol. 79, no. 4, pp. 722–727, 2011.
- [99] J. L. Bishop, C. M. Pieters, and J. O. Edwards, “Infrared Spectroscopic Analyses on the Nature of Water in Montmorillonite,” *Clays Clay Miner.*, vol. 42, no. 6, pp. 702–716, 1994.

## REFERENCES

- [100] I. Langmuir, "THE ADSORPTION OF GASES ON PLANE SURFACES OF GLASS, MICA AND PLATINUM.," *J. Am. Chem. Soc.*, vol. 40, no. 9, pp. 1361–1403, 1918.
- [101] H. Freundlich, "Über die adsorption in lösungen," *Zeitschrift für Phys. Chemie*, vol. 57, no. 1, pp. 385–470, 1907.
- [102] E. Cristiano, Y. J. Hu, M. Siegfried, D. Kaplan, and H. Nitsche, "A comparison of point of zero charge measurement methodology," *Clays Clay Miner.*, vol. 59, no. 2, pp. 107–115, 2011.
- [103] R. D. Shannon, "Revised effective ionic radii and systematic studies of interatomic distances in halides and chalcogenides," *Acta Crystallogr. Sect. A*, vol. 32, no. 5, pp. 751–767, 1976.
- [104] Y. M. Nor, "Ecotoxicity of copper to aquatic biota: A review," *Environ. Res.*, vol. 43, no. 1, pp. 274–282, 1987.
- [105] L. Hidmi and M. Edwards, "Role of temperature and pH in Cu(OH)<sub>2</sub> solubility," *Environ. Sci. Technol.*, vol. 33, no. 15, pp. 2607–2610, 1999.
- [106] S. K. Lagergren, "About the theory of so-called adsorption of soluble substances," *Sven. Vetenskapsakad. Handlingar*, vol. 24, pp. 1–39, 1898.
- [107] G. Blanchard, M. Maunaye, and G. Martin, "Removal of heavy metals from waters by means of natural zeolites," *Water Res.*, vol. 18, no. 12, pp. 1501–1507, 1984.
- [108] D. K. L. Harijan and V. Chandra, "Akaganeite nanorods decorated graphene oxide sheets for removal and recovery of aqueous phosphate," *J. Water Process Eng.*, vol. 19, no. June, pp. 120–125, 2017.
- [109] G. Li, S. Gao, G. Zhang, and X. Zhang, "Enhanced adsorption of phosphate from aqueous solution by nanostructured iron(III)-copper(II) binary oxides," *Chem. Eng. J.*, vol. 235, pp. 124–131, 2014.
- [110] P. Vanelderen, R. G. Hadt, P. J. Smeets, E. I. Solomon, R. A. Schoonheydt, and B. F. Sels, "Cu-ZSM-5: A biomimetic inorganic model for methane oxidation.," *J. Catal.*, vol. 284, no. 2, pp. 157–164, Dec. 2011.
- [111] J. S. Woertink *et al.*, "A [Cu<sub>2</sub>O]<sub>2</sub><sup>+</sup> core in Cu-ZSM-5, the active site in the oxidation of methane to methanol," *Proc. Natl. Acad. Sci.*, vol. 106, no. 45, pp. 18908–18913, 2009.



## REFERENCES

- [112] Z. Tyeklar, R. R. Jacobson, N. Wei, N. N. Murthy, J. Zubieta, and K. D. Karlin, “Reversible reaction of dioxygen (and carbon monoxide) with a copper(I) complex. X-ray structures of relevant mononuclear Cu(I) precursor adducts and the trans-( $\mu$ -1,2-peroxo)dicopper(II) product,” *J. Am. Chem. Soc.*, vol. 115, no. 7, pp. 2677–2689, Apr. 1993.
- [113] M. J. Baldwin, P. K. Ross, J. E. Pate, Z. Tyeklar, K. D. Karlin, and E. I. Solomon, “Spectroscopic and theoretical studies of an end-on peroxide-bridged coupled binuclear copper(II) model complex of relevance to the active sites in hemocyanin and tyrosinase,” *J. Am. Chem. Soc.*, vol. 113, no. 23, pp. 8671–8679, Nov. 1991.
- [114] M. C. Simoes, K. J. Hughes, D. B. Ingham, L. Ma, and M. Pourkashanian, “Estimation of the Thermochemical Radii and Ionic Volumes of Complex Ions,” *Inorg. Chem.*, vol. 56, no. 13, pp. 7566–7573, Jul. 2017.
- [115] P. J. O’Brien and D. Herschlag, “Does the active site arginine change the nature of the transition state for alkaline phosphatase-catalyzed phosphoryl transfer? [[11],” *Journal of the American Chemical Society*, vol. 121, no. 47, pp. 11022–11023, 1999.
- [116] P. J. O’Brien and D. Herschlag, “Alkaline phosphatase revisited: Hydrolysis of alkyl phosphates,” *Biochemistry*, vol. 41, no. 9, pp. 3207–3225, 2002.
- [117] I. Nikolic-Hughes, D. C. Rees, and D. Herschlag, “Do electrostatic interactions with positively charged active site groups tighten the transition state for enzymatic phosphoryl transfer?,” *J. Am. Chem. Soc.*, vol. 126, no. 38, pp. 11814–11819, 2004.
- [118] S. C. L. Kamerlin, P. K. Sharma, R. B. Prasad, and A. Warshel, “Why nature really chose phosphate,” *Q. Rev. Biophys.*, vol. 46, no. 1, pp. 1–132, 2013.
- [119] T. Hunter, “Why nature chose phosphate to modify proteins,” *Philos. Trans. R. Soc. B Biol. Sci.*, vol. 367, no. 1602, pp. 2513–2516, 2012.
- [120] J. K. Lassila, J. G. Zalatan, and D. Herschlag, “Biological Phosphoryl-Transfer Reactions: Understanding Mechanism and Catalysis,” *Annu. Rev. Biochem.*, vol. 80, no. 1, pp. 669–702, 2011.
- [121] A. Bononi *et al.*, “Protein kinases and phosphatases in the control of cell fate,” *Enzyme Res.*, vol. 2011, no. 1, 2011.
- [122] J. R. Knowles, “Enzyme-Catalyzed Phosphoryl Transfer Reactions,” *Annu. Rev. Biochem.*, vol. 49, no. 1, pp. 877–919, 1980.

## REFERENCES

- [123] C. P. Austin, "National Human Genome Research Institute." [Online]. Available: <https://www.genome.gov/genetics-glossary/Enzyme>.
- [124] Lovinne, "Phosphatase." [Online]. Available: [https://en.wikipedia.org/wiki/Phosphatase#/media/File:General\\_phosphatase\\_mechanism.png](https://en.wikipedia.org/wiki/Phosphatase#/media/File:General_phosphatase_mechanism.png).
- [125] A. I. Taylor *et al.*, "Catalysts from synthetic genetic polymers," *Nature*, vol. 518, no. 7539, pp. 427–430, 2015.
- [126] A. E. Donnelly, G. S. Murphy, K. M. Digianantonio, and M. H. Hecht, "A de novo enzyme catalyzes a life-sustaining reaction in *Escherichia coli*," *Nat. Chem. Biol.*, vol. 14, no. 3, pp. 253–255, 2018.
- [127] C. Xu, S. Hu, and X. Chen, "Artificial cells: from basic science to applications," *Mater. Today*, vol. 19, no. 9, pp. 516–532, 2016.
- [128] G. Wang, J. Zhang, X. He, Z. Zhang, and Y. Zhao, "Ceria Nanoparticles as Enzyme Mimetics," *Chinese J. Chem.*, vol. 35, no. 6, pp. 791–800, 2017.
- [129] V. Baldim, F. Bedioui, N. Mignet, I. Margail, and J.-F. Berret, "The enzyme-like catalytic activity of cerium oxide nanoparticles and its dependency on Ce 3+ surface area concentration," *Nanoscale*, vol. 10, no. 15, pp. 6971–6980, 2018.
- [130] T. Naganuma, "Shape design of cerium oxide nanoparticles for enhancement of enzyme mimetic activity in therapeutic applications," *Nano Res.*, vol. 10, no. 1, pp. 199–217, 2017.
- [131] M. J. Manto, P. Xie, and C. Wang, "Catalytic Dephosphorylation Using Ceria Nanocrystals," *ACS Catal.*, vol. 7, no. 3, pp. 1931–1938, 2017.
- [132] E. P. Serjeant and B. Dempsey, *Ionisation constants of organic acids in aqueous solution*. Oxford: Pergamon Press, 1979.

# Curriculum Vitae

## *Contact information*

1 E University Pkwy Unit 1407, Baltimore MD 21218

(443) 500-8717

akshat.vij@jhu.edu

## *Summary*

I'm an experienced professional currently in my final year of a doctoral program in chemical and biomolecular engineering at Johns Hopkins University. I bring several years of hands-on professional work experience in chemical, systems and software engineering to my research work in environmental nutrient recovery, zeolite characterization and heterogeneous catalysis.

In addition to research, I have held several leadership roles in the Nano Energy Laboratory of Dr. Chao Wang, including Lab Captain, Laboratory Safety Coordinator and Purchasing Coordinator. I've also gained experience in the pharmaceutical industry through an internship at Bristol-Myers Squibb in 2019.

***Education***

**Doctor of Philosophy (Chemical and Biomolecular Engineering)**

Advisor: Dr. Chao Wang

*Johns Hopkins University – Baltimore MD*

2016 – 2020

GPA: 4.00

**Bachelor of Engineering (Chemical and Process Engineering) *with First Class Honors***

*and*

**Bachelor of Commerce (Investment Finance, Corporate Finance)**

*The University of Western Australia – Crawley WA, Australia*

2005 – 2010

GPA: 6.81 (7 scale)

***RESEARCH EXPERIENCE***

JOHNS HOPKINS UNIVERSITY, Baltimore MD

Sep'16-Dec'20

**Doctoral Research Student**

- Designed and performed experiments for testing phosphate-adsorption properties of metal-exchanged zeolites, including kinetic, equilibrium and separation studies
- Studied the catalytic dephosphorylation of organic phosphates by cerium oxide and other catalysts as artificial enzymes
- Experience with aqueous and organic-phase nanoparticle synthesis (e.g., metal-exchanged zeolites, gold, platinum, cobalt)
- Electrochemical synthesis of composite metal/metal-oxide bifunctional electrocatalysts for ORR and OER; performance testing with cyclic voltammetry
- Expertise in method development for chemical assays of environment nutrients (phosphate, nitrate)
- Precision-oriented wet laboratory technique and thorough understanding of various analytical calibration methods, statistical analysis and error quantification
- Experience with various characterization techniques including SEM, TEM, XRD, UV-VIS, HPLC, FT-IR

***PROFESSIONAL EXPERIENCE***

**BRISTOL-MYERS SQUIBB** (c/o AllSource PPS), New Brunswick, New Jersey

Jun'19- Aug'19

**Parenteral Drug Product Intern, Manufacturing Science and Technology**

- Led execution of a lab-based shear impact study on commercial drug product
- Developed lab-scale study plan for investigating impact of proposed enhancements to a commercial drug product's formulation process
- Experience in sterile lab procedures and pharmaceutical particle characterization techniques including HIAC and MFI
- Built and tested innovative software tool using Python for automated, real-time mass measurements in the laboratory

**MRX TECHNOLOGIES**, Perth, Australia

Apr'13- Aug'14

**Systems / Software Engineer**

- Developed software for multimillion-dollar automation projects in the mining, exploration and rail industries
- C++ for embedded systems (MS Visual Studio, STL, Boost, Qt user interfaces, QNX, Linux), Python scripting
- ISO 9001 and SVN environment

## CURRICULUM VITAE

- Exposure to all parts of the development cycle: specification, design, coding, testing, maintenance
- Engaged in independent hardware testing and research to improve software design and eliminate bugs in \$100K per unit products sold in the US, UK and Germany
- Responsible for independently learning new programming languages and tools to achieve required outcomes
- Received positive feedback from technical and project managers for timely delivery of reliable software

**HATCH-** Non-Ferrous Unit, Perth, Australia

Jun'11- Oct'12

### **Chemical Engineer**

- Key contributor on several multidisciplinary metallurgical plant design projects ranging from <\$1M to \$1B
- Responsible for calculating mass and energy balances for process plant with estimated \$50M per year operating cost, using process modelling software and first-principles analysis
- Created financial models of plant upgrade scenarios by integrating with process models developed in Microsoft Excel
- Researched thermal oxidizer technology and summarized findings in a technical paper for the senior client decision-maker

## CURRICULUM VITAE

- Received award from senior management in recognition of outstanding work performance
- Served as business unit representative on the Hatch Professional Development Program (PDP) committee



***CERTIFICATIONS & HONORS***

- Award: Whiting School of Engineering's Award for Outstanding Teaching Assistants, 2020
- Graduated BEng- First Class Honors and Top Student in 6 Courses, 2010
- Graduated BComm- Best Student Majoring in Finance (Investment) and Top Student in 4 Courses, 2010
- Scholarship: Australian Institute of Nuclear Science and Engineering Winter School, 2007
- Scholarship: Jean Rogerson Studentship – Engineering & Mathematical Sciences, 2005
- Australian Students Prize for Excellence, 2004

***TEACHING AND MENTORING EXPERIENCE***

**Co-instructor**

Thermodynamics, Statistical Mechanics, and Kinetics (EN.540.630)

Fall, 2018

**Teaching Assistant**

Engineering Thermodynamics (EN.540.203)

Spring, 2018

Thermodynamics, Statistical Mechanics, and Kinetics (EN.540.630)

Fall, 2017

Engineering Thermodynamics (EN.540.203)

Spring, 2017

**Volunteer Mentor, Women in STEM Program – Johns Hopkins University**

Baltimore City School intern (Sophomore)

Spring, 2020

Bryn Mawr School intern (Senior)

Summer, 2018

Bryn Mawr School intern (Junior)

Summer, 2017

***PUBLICATIONS***

1. **Vij, Akshat** and Chao Wang. 2020 (submission pending). “Phosphate anion adsorption as a liquid phase probe for active sites in metal-exchanged zeolites.” *Department of Chemical and Biomolecular Engineering, Johns Hopkins University.*

(Contribution: Conceived the project with doctoral advisor, designed and executed all experimental work, performed all data analysis, wrote the manuscript)

2. Khalid, Muneeba, Evan Johnson, **Akshat Vij**, Edward J. Bouwer, Hussnain A. Janjua, and Michael J. Betenbaugh. 2018. “Anaerobic Digestion Restricted to Phase I for Nutrient Release and Energy Production Using Waste-Water Grown *Chlorella Vulgaris*.” *Chemical Engineering Journal* 352 (May). Elsevier: 756–64. <https://doi.org/10.1016/j.cej.2018.07.084>.

(Contribution: Reviewed and edited the manuscript for clarity rewriting 40-50%, assisted lead author with data interpretation and calculations, penned most of the responses to the reviewers’ comments)